



^b
**UNIVERSITÄT
BERN**

Graduate School for Cellular and Biomedical Sciences
University of Bern

Image-based biomechanical assessment of vertebral body and intervertebral disc in the human lumbar spine

PhD Thesis submitted by

Ghislain Maquer

from France

for the degree of

PhD in Biomedical Engineering

Supervisor

Prof.Dr.Philippe K. Zysset
Institute for Surgical Technology & Biomechanics
Medicine Faculty of the University of Bern

Co-advisor

Prof.Dr. Stephen J. Ferguson
Institut für Biomechanik
ETH Zürich

March 2013

Accepted by the Faculty of Medicine, the Faculty of Science and the Vetsuisse
Faculty of the University of Bern at the request of the Graduate School for
Cellular and Biomedical Sciences

Bern, Dean of the Faculty of Medicine

Bern, Dean of the Faculty of Science

Bern, Dean of the Vetsuisse Faculty Bern

PhD Committee

Advisor

Prof.Dr. Philippe K. Zysset
Institute for Surgical Technology and Biomechanics
University of Bern

Co-Advisor

Prof.Dr. Stephen J. Ferguson
Institut für Biomechanik
ETH Zürich

Mentor

Prof.Dr. Chris Boesch
Department of Clinical Research
Inselspital, University of Bern

External Co-Referee

Prof.Dr. Wafa Skalli
Laboratoire de Biomécanique
Ecole Nationale Supérieure d'Arts et Métiers
Paris, France

"My back hurts...!"

My Grandma

Pour mes parents et mon frère.

Acknowledgements

This is it. A bit more than three years of work in two research institutes in two different countries. When I started in ILSB in Vienna, I hardly imagined that I would actually graduate from the University of Bern. On the way, I met people who supported this thesis by their outstanding supervision, essential contributions or valuable friendship.

My first thought goes to Prof. Philippe Zysset who continuously supervised this work with the same interest and patience. He always found the time to discuss the issues I was facing. “The mediocre teacher tells. The good teacher explains. The superior teacher demonstrates. The great teacher inspires” (Ward). Prof. Zysset is a great teacher.

Looking back to the very beginning, I owe many thanks to Prof. Dieter Pahr for introducing me to Prof. Zysset two years after supervising one of my internships. Moreover, without his great programming and scientific skills, this thesis would have another face.

I am very grateful to my co-advisor Prof. Stephen Ferguson and mentor Prof. Chris Boesch, who never hesitated to share their knowledge in intervertebral disc biomechanics and MRI as well as Prof. Wafa Skalli who accepted to evaluate this work as the external referee.

Thanks a lot to all the collaborators: Dr. Enrico Dall’ara, Vaclav Brandejsky, Marc Laurent, Dr. Mauricio Reyes, Dr. Peter Vermathen, Prof. Michael Pretterklieber, Dr. Pavel Galibarov, Dr. Lorin Benneker and Prof. Atsuya Watanabe. Their expertise in their respective field played a big part in the accomplishment of each chapter of this dissertation.

I cannot mention everybody but I thank all the colleagues from ILSB and ISTB especially Urs Rohrer and his team, Alex Bürki, Allison Clouthier and Uwe Wolfram for their help and the lively table football games and the two gentlemen who relocated to Bern as well, Hadi Hosseini and Jakob Schwiedrzik.

This project was made possible through funding obtained from the European Community, Grant Agreement n° PITN-GA-2009-238690-SPINEFX

Finally, I would like to thank all my friends in France, Austria, Switzerland and overseas.

Par ailleurs, il m'est impossible de ne pas remercier mes parents pour leur support malgré la distance et mon frère, capable de transformer un anodin coup de fil en fou rire.

Abstract

Life expectancy continuously increases but our society faces age-related conditions. Among musculoskeletal diseases, osteoporosis associated with risk of vertebral fracture and degenerative intervertebral disc (IVD) are painful pathologies responsible for tremendous healthcare costs. Hence, reliable diagnostic tools are necessary to plan a treatment or follow up its efficacy. Yet, radiographic and MRI techniques, respectively clinical standards for evaluation of bone strength and IVD degeneration, are unspecific and not objective.

Increasingly used in biomedical engineering, CT-based finite element (FE) models constitute the state-of-art for vertebral strength prediction. However, as non-invasive biomechanical evaluation and personalised FE models of the IVD are not available, rigid boundary conditions (BCs) are applied on the FE models to avoid uncertainties of disc degeneration that might bias the predictions. Moreover, considering the impact of low back pain, the biomechanical status of the IVD is needed as a criterion for early disc degeneration.

Thus, the first FE study focuses on two rigid BCs applied on the vertebral bodies during compression test of cadaver vertebral bodies, vertebral sections and PMMA embedding. The second FE study highlights the large influence of the intervertebral disc's compliance on the vertebral strength, damage distribution and its initiation. The third study introduces a new protocol for normalisation of the IVD stiffness in compression, torsion and bending using MRI-based data to account for its morphology. In the last study, a new criterion (Otsu threshold) for disc degeneration based on quantitative MRI data (axial T_2 map) is proposed.

The results show that vertebral strength and damage distribution computed with rigid BCs are identical. Yet, large discrepancies in strength and damage localisation were observed when the vertebral bodies were loaded via IVDs. The normalisation protocol attenuated the effect of geometry on the IVD stiffnesses without complete suppression. Finally, the Otsu threshold computed in the posterior part of annulus fibrosus was related to the disc biomechanics and meet objectivity and simplicity required for a clinical application.

In conclusion, the stiffness normalisation protocol necessary for consistent IVD comparisons and the relation found between degeneration, mechanical response of the IVD and Otsu threshold lead the way for non-invasive evaluation biomechanical status of the IVD. As the FE prediction of vertebral strength is largely influenced by the IVD conditions, this data could also improve the future FE models of osteoporotic vertebra.

Content

ACKNOWLEDGEMENTS	VII
ABSTRACT	VIII
CHAPTER 1: INTRODUCTION.....	1
1. <i>Motivations</i>	1
2. <i>Anatomy</i>	2
2.1 The lumbar spine	2
2.2 The vertebra.....	4
2.3 The intervertebral disc.....	4
2.4 Anatomical references.....	4
3. <i>Conditions of the vertebral body</i>	6
3.1 Osteoporosis	6
3.2 Radiographic diagnosis	6
3.3 Subject-specific finite element models of the vertebral body	8
4. <i>Conditions of the intervertebral disc</i>	10
4.1 Intervertebral disc degeneration	10
4.2 Evaluation of the degeneration grade	12
4.3 Subject-specific finite element models of the intervertebral disc.....	14
5. <i>Objectives of the thesis</i>	16
6. <i>Outline of the thesis</i>	17
CHAPTER 2: THE INFLUENCE OF THE ENDPLATE ON VERTEBRAL STRENGTH	25
1. <i>Introduction</i>	27
2. <i>Materials and methods</i>	27
2.1 CT scans of the vertebral bodies.....	27
2.2 Image processing	28
2.3 Voxel FE models and boundary conditions.....	29
2.4 Simulations.....	29
3. <i>Results</i>	30
3.1 Comparison of ultimate forces	30
3.2 Comparison of the damage distribution	31
4. <i>Discussion</i>	31
CHAPTER 3: THE INFLUENCE OF INTERVERTEBRAL DISC DEGENERATION ON VERTEBRAL STRENGTH	37
1. <i>Introduction</i>	39
2. <i>Materials and Methods</i>	40
2.1 CT scans of the vertebral bodies.....	40
2.2 Image processing	40
2.3 Mesh generation.....	41
2.4 Material properties	42
2.4.1 Bone constitutive model	42
2.4.2 Intervertebral disc constitutive model.....	43
2.5 Simulations.....	45
2.6 Statistics	46
3. <i>Results</i>	46
3.1 Comparison of force-displacement curves	46
3.1.1 Verification of the force-displacement curves.....	46

3.1.2	Pre-yield local force maxima.....	48
3.1.3	The effect of boundary condition on the yield behaviour	48
3.2	Comparison of damage localisation.....	48
3.2.1	Evolution of damage	48
3.2.2	Damage localization with IVD at the pre-yield local force maxima	48
3.2.3	Qualitative observations from damage plots.....	50
3.2.4	Quantitative evaluation of damage	50
4.	<i>Discussion</i>	52
CHAPTER 4:	NORMALISATION OF INTERVERTEBRAL DISC COMPLIANCES.....	59
1.	<i>Introduction</i>	61
2.	<i>Materials and methods</i>	62
2.1	Method of normalisation.....	62
2.2	Parameter study.....	63
2.3	Experimental application	65
3.	<i>Results</i>	67
3.1	Outcomes of the parameter study	67
3.2	Experimental results	68
4.	<i>Discussion</i>	72
CHAPTER 5:	AN MRI-BASED METHODOLOGY FOR BIOMECHANICAL EVALUATION OF DEGENERATED INTERVERTEBRAL DISCS	79
1.	<i>Introduction</i>	81
2.	<i>Materials and methods</i>	82
2.1	Qualitative and quantitative MRI imaging.....	82
2.2	Apparent intervertebral moduli.....	84
2.3	Link between degeneration grade, quantitative MRI data and apparent modulus 85	
3.	<i>Results</i>	86
4.	<i>Discussion</i>	89
CHAPTER 6:	CONCLUSIONS.....	97
1.	<i>Discussions and limitations</i>	97
2.	<i>Outlooks</i>	100
2.1	MRI-based intervertebral disc model	100
2.2	Patient-specific loading on the vertebral body model	101
APPENDIX:	FROM ANYBODY TO ABAQUS.....	103
1.	<i>Introduction</i>	104
2.	<i>Materials and methods</i>	104
2.1	Vertebral body model	104
2.2	Personalisation of the AMS model	105
2.3	Combining musculoskeletal and finite element models.....	106
2.4	Finite element simulations.....	107
3.	<i>Results</i>	108
4.	<i>Discussion</i>	109
CURRICULUM VITAE.....		113
DECLARATION OF ORIGINALITY.....		115

Chapter 1: Introduction

1. Motivations

Thanks to the progress of science, life expectancy continuously increases but frequent age-related diseases are an issue of our societies. Amongst the common musculoskeletal diseases, the back conditions are particularly invalidating and responsible for tremendous healthcare costs. The spinal column provides support for the body via the vertebrae while the intervertebral discs ensure sufficient mobility and contribute to stability of the whole with the ligaments and muscles. Hence, any alterations of either bone or disc can have severe consequences in the quality of life of the patients.

Osteoporosis is a bone condition characterised by low bone density and degradation of the bone architecture involved in more than 500000 vertebral fractures in Europe a year. Reliable diagnostic tools are therefore necessary to plan a treatment. Nowadays, radiographic techniques represent the clinical standard for non-invasive bone strength prediction. However, if those methods can assess the bone density, the current tools do not account for its local variation or the bone morphology. Finite element analysis (FEA) is a numerical method increasingly used in biomedical engineering. In osteology, patient-specific finite element models constitute the current state-of-art for vertebral strength prediction. Thanks to their ability to compute bone strength within few minutes on a standard PC and the possibility to simulate various loading scenarios, the FE models are already used in clinical follow-up studies. Nowadays, rigid boundary conditions such as embedding of the endplates in polymethylmethacrylate (PMMA) are chosen to simplify the experimental validation and avoid the uncertainties of various degrees of disc degeneration in elderly spines but the boundary conditions have influence on the FE predictions of vertebral strength and should be accounted for.

Besides osteoporosis, at least half of the elderly suffers from degenerated intervertebral disc disease. This condition modifies the structure and biochemical constitution of the disc, affecting the spine stability, modifying the load distribution on the vertebra and sometimes inducing low back pain. Hence, effort has been put in developing non-invasive methods for

detection and evaluation of degeneration based on qualitative clinical MRI (magnetic resonance imaging) or quantitative MRI. Nonetheless, the standard procedure consisting in discrete grading of the degeneration is unspecific and subjected to the clinicians' experience. As degeneration occurs, the pressure in the dehydrated disc drops, its height reduces and its collagen structure modified, eventually leading to initiation of lesions and protrusions. The stability of the whole segment is then affected by consequent alterations of the range of motion and stiffness, eventually inducing low back pain and abnormal load distribution on the endplates. Yet, albeit the degenerative process alters the mechanics of the spinal segment, none of the current assessment techniques is able to evaluate objectively how.

Therefore, considering the socio-economic impact of low back pain, the advantage of an objective technique for early disc degeneration related to its mechanics is obvious. Not only, the biomechanical status of intervertebral disc is possibly related to low back pain but such data could be included in the future FE models of osteoporotic vertebral bodies to avoid assumptions on the boundary conditions that potentially bias the strength predictions.

2. Anatomy

This part mainly refers to the work of Bogduk 2005, Adams and Dolan 2005, Prithvi Raj et al. 2008 and introduces briefly the anatomical structures under study.

2.1 The lumbar spine

The spine forms a solid pillar supporting the body weight. Apart from the sacrum, composed of fused bones, the 3 other sections of the human spine (cervical, thoracic and lumbar) are articulated around 24 vertebrae separated by the fibro-cartilaginous intervertebral discs responsible for the spine overall flexibility. The lumbar spine can be segmented in a succession of articulations called intervertebral segments consisting in two successive vertebrae bound by ligaments, muscles and intervertebral disc. The segments are often referred to as functional spinal unit (FSU), the smallest element exhibiting the biomechanical function of the entire lumbar column (Roh et al. 2005) (Fig. 1).

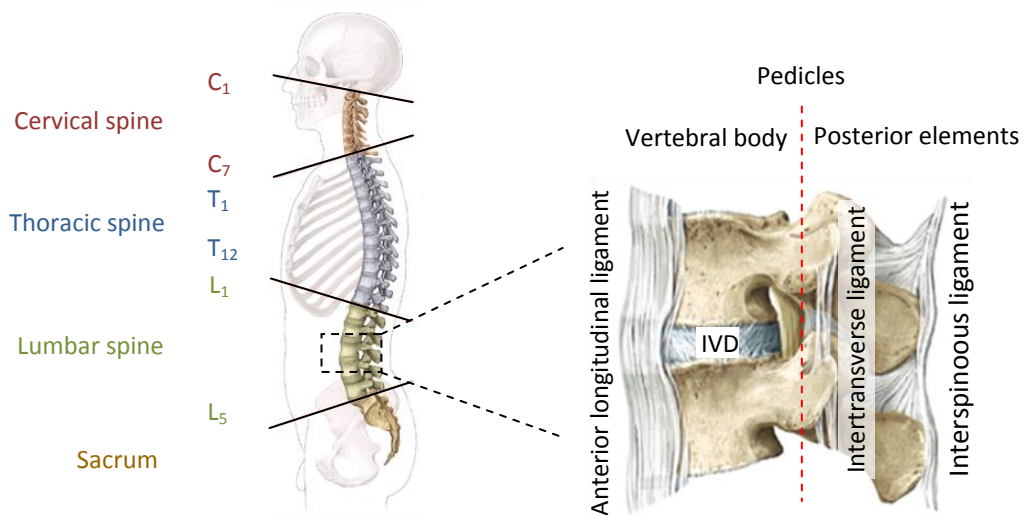


Fig. 1. The human spine and intervertebral segment. (Schünke et al.2007)

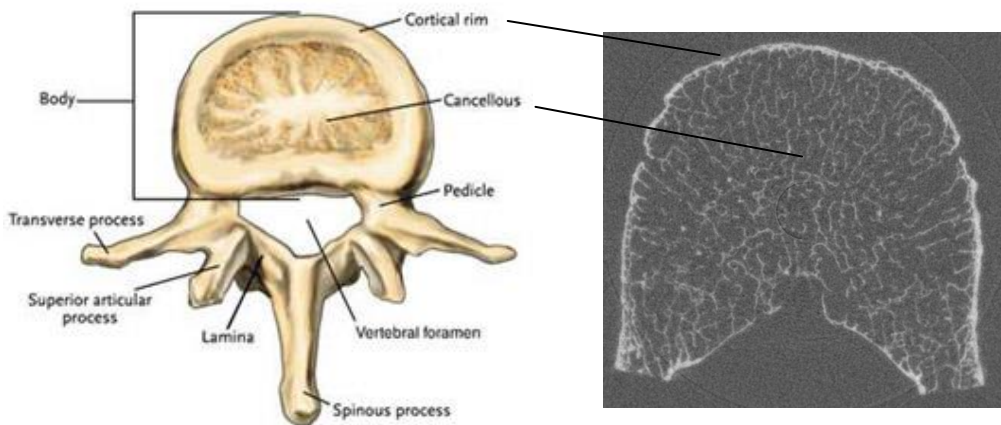


Fig. 2. Schematic (www.back.com) and CT image of a lumbar vertebra (from our study).

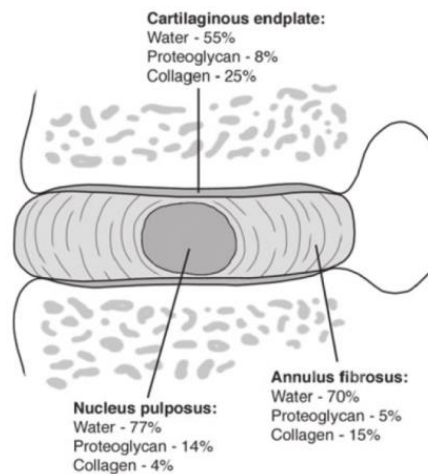


Fig. 3. The intervertebral disc content (Prithvi Raj et al. 2008).

2.2 The vertebra

Three main structures compose the vertebra: the vertebral body supports the loads, the vertebral arch houses the spinal cord, a delicate and vital bundle of nerve fibres connecting the brain to the rest of the body and part of the Central Nervous System (CNS). The spinous and transverse processes, anchorage area for many muscles and ligaments, allow respectively motions in extension and torsion. The area of contact between processes, covered by smooth cartilage is called facet joint. The vertebral body consists of trabecular (or cancellous) core (~70 % of the weight) surrounded by a lateral cortical wall (cortex) and a caudal and cranial cortical endplates (< 500 μm in thickness). The trabecular bone, filled with marrow, is acting as a hydraulic cushion under high compressive loads (Fig. 2).

2.3 The intervertebral disc

The intervertebral disc (IVD) is a large avascular cartilaginous tissue tiding the vertebrae together. The healthy IVD is mainly composed of water (~70%), features a highly rate-dependent mechanical behaviour (Kurutz and Oroszvary. 2010) and is characterised by a gelatinous nucleus pulposus surrounded by the concentric layers of collagen fibres of the fibrous annulus fibrosus. Embedded in the ground substance of the annulus, the collagen fibres are alternatively inclined at $\pm 30^\circ$ to the axial plane and anchored in the cartilaginous endplates (Fig. 3). Healthy annulus and nucleus interact to distribute the load on the vertebra. It is usually assumed that an unloaded IVD is in a stress free state. Thus, under compression, the pressurization of the nucleus stretches the inner annulus fibres with the progressive recruitment of the outer fibres. Nevertheless, latest experiments highlighted the existence of prestress in the annulus even without external load or pressurisation as the nucleus was excised. This result suggests that the tensile stress resulting from elevated hydrostatic pressure of the nucleus under compression is rather distributed in the whole annulus (Michalek et al. 2012b).

2.4 Anatomical references

The clinicians often describe the body via 2D images in three anatomical planes. The sagittal plane separates laterally the body, the axial or transverse plane separates the superior sections from the inferior body and the coronal plane divides the body into ventral and

dorsal regions. Three axes are also used to explicit the motion of the body: the mediolateral (left-right), anteroposterior (front-back) and craniocaudal (superior-inferior) axes (Fig. 4). Six translations and rotations along or around the anatomical axes are used to describe any rigid body motions in 3D. Although it is rather usual to observe coupled motions *in vivo*, the following work focuses on axial compression and single rotational motions: torsion, lateral bending left-right, forward bending (flexion) and backward bending (extension) (Fig. 5).

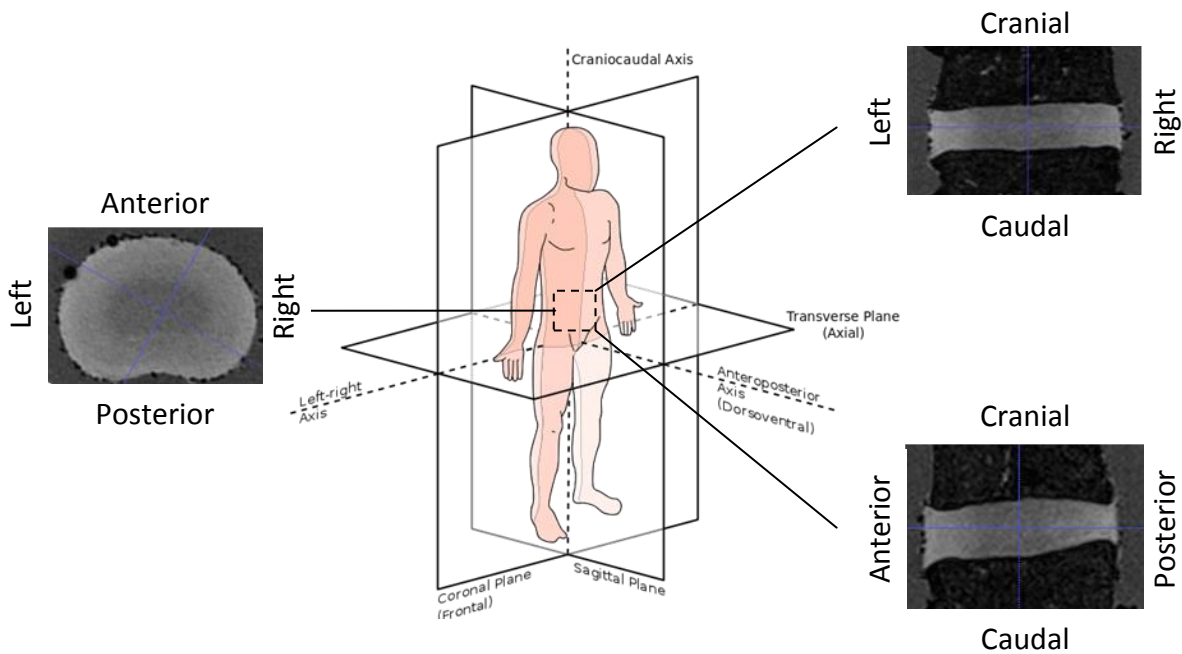


Fig. 4. An intervertebral disc in the anatomical planes (www.wikipedia.org).

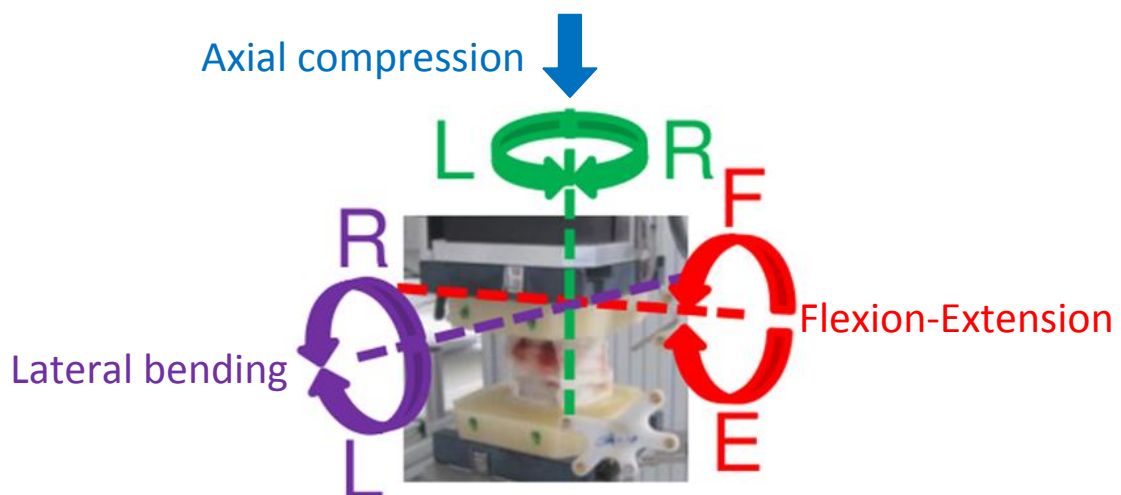


Fig. 5. Motions of the intervertebral segments (from our study).

3. Conditions of the vertebral body

3.1 Osteoporosis

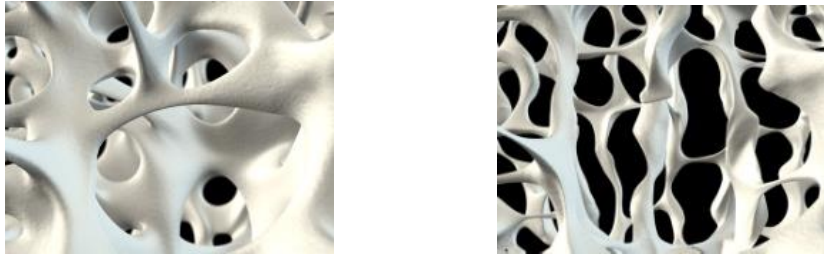


Fig. 6. Healthy and osteoporotic trabecular bone (www.concordortho.com/patient-education).

The WHO (World Health Organisation) defines osteoporosis as “a systemic skeletal disease characterised by low bone mass and microarchitectural deterioration of bone tissue with a consequent increase in bone fragility and susceptibility to fracture” (Kanis et al. 2008). The consequences of the pathology are clear: approximately 1.5 million osteoporotic fractures occur in the U.S. a year generating an incredible yearly expense of 14 billion dollars. This includes wrist and hip fractures but the most common is, by far, the vertebral fractures with approximately 750000 occurrences per year (Watts 2001).

The reason of such widespread lies in the absence of symptoms. Therefore, a monitoring is necessary to detect the disease, assess the vertebral strength and plan a treatment at an early stage and its follow-up before further bone loss (Griffith and Genant 2011). As the amount and quality of a bone are important criteria of its strength, the current densitometric techniques are based on the absorption of X-rays by the tissues and the amount of mineralised bone per area or volume measured, Bone Mineral Density (BMD) is used in clinics as a surrogate for bone strength. However, an ideal assessment of the vertebral strength must also account for bone morphology (Griffith and Genant 2008).

3.2 Radiographic diagnosis

A number of radiographic techniques were developed for the diagnosis of osteoporosis. DXA (Dual Energy X-ray Absorptiometry) is assessing the apparent areal BMD (aBMD, g/cm^2) of a projection of the volumetric BMD of the bone on a plane. Despite being the clinical standard, this measure includes indistinctively cortex and trabecular bone and other bony

structures (posterior elements, ribs, osteophytes) and tends to overestimate the BMD of the vertebral body.

Although 3D spine reconstruction is possible via Biplanar X-ray imaging techniques (EOS Imaging, Paris, France), with the advantage of standing position and low radiation, QCT (Quantitative Computed Tomography) is the reference in assessing the 3D bone geometry (Dubousset et al. 2010, Illes and Somoskeoy 2012). Notwithstanding the computation of the apparent volumetric BMD (vBMD, mg/cm^3) linearly related to the Hounsfield Units, with a resolution of 0.6 mm and the distinction between trabecular and cortical bone, QCT is seldom used because of a substantially higher radiation dose than DXA. High resolution QCT (HRQCT) offers higher resolution ($\sim 200 \mu\text{m}$) but is still insufficient for the determination of trabecular architecture (Graeff et al. 2013), as such details can only be captured *in vivo*, to some extent, on the wrist or the foot using HRpQCT (High resolution peripheral QCT, $82 \mu\text{m}$, Griffith and Genant 2011).

Recently, textural methods were used to assess the bone morphology. TBS (Trabecular Bone Score), an index of trabecular architecture evaluating local variations in gray level from DXA image of the lumbar spine shows promises and seems to provide better vertebral strength assessment when combined with the BMD data (Roux et al. 2013, Boutrouy et al. 2013)

Nevertheless, these qualitative techniques cannot be utilised to determine the loading mode that put the vertebra at higher risk or the potential damage pattern and are therefore not a fully satisfactory surrogate of bone strength (Dall'Ara et al. 2012).

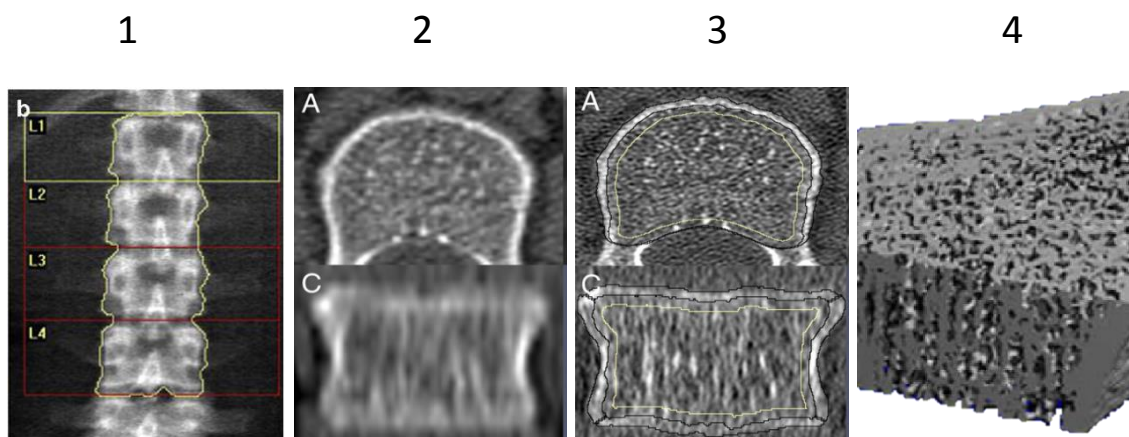


Fig. 7. (1) Frontal DXA examination of a lumbar spine, axial (A) and sagittal (B) view of a QCT (2) and HRQCT (3) of lumbar vertebral body and (4) HRpQCT of distal radius (1-4: Griffith and Genant 2008, 2-3: Graeff et al. 2013).

3.3 Subject-specific finite element models of the vertebral body

Finite element analysis (FEA) is a numerical method increasingly used in biomedical engineering with a tendency towards patient-specific modelling (Gefen, 2012). In bone and mineral research, the latest models are fully CT-based (geometry and material properties), experimentally validated and used in clinical trials and treatment follow-ups (Keaveny et al. 2007, Graeff et al. 2009, Graeff et al. 2013, Gluer et al. 2013) as they better predict the vertebral body strength than clinical methods such as DXA or QCT (Crawford et al. 2003).

Although vertebra meshes can be shaped to biplanar images (EOS), most models are automatically generated by converting directly the voxels from CT images in hexahedral elements (Sapin de Brosse et al. 2012, Glaser et al. 2012). The models based on QCT present ragged edges that may generate artificial stress and local damage if not smoothed (Chevalier and Zysset 2012). Moreover, details of the bone architecture are not captured by the clinical devices. Thus, in EOS and QCT-based voxel models, the trabecular structure and the cortical shell are omitted or constant corticular thickness is assumed (Pahr et al. 2012a). A reduced mesh size (μ FE), achieved via the use of μ CT data (30 μ m), includes the cortex and trabecular morphology but requires large computer resources and is not feasible *in vivo* (Eswaran et al. 2007, Fields et al. 2010). At cost of a longer pre-processing time, the alternative lies in the so-called smooth FE models with CT-based cortex thickness generated from intermediate resolution (HRpQCT, Pahr et al. 2009, Pahr et al. 2012a).

The degree of simplification of the material properties of the simulated vertebral body is induced by the imaging modality that imaged the bone. Most CT-based models feature isotropic density-based bone material properties (Homminga et al. 2011, Erdem et al. 2011) although the trabecular architecture is an important criterion for the vertebral strength, especially when osteoporosis and unusual loading are involved (Homminga et al. 2004, Wolfram et al. 2011). The cancellous morphology is naturally accounted for in μ FE models and FE predictions of vertebral strength of smooth models are improved by the inclusion of CT-based trabecular fabric compared to the sole use of simple power-law constitutive law (Pahr et al. 2009). Moreover, following tedious modelling and experimental validation, usually indentations, the latest material models (or constitutive laws) simulate the bone more realistically by including the post-yield behaviour, elastic-viscoplastic damage (Schwiedrzik et al. 2012),

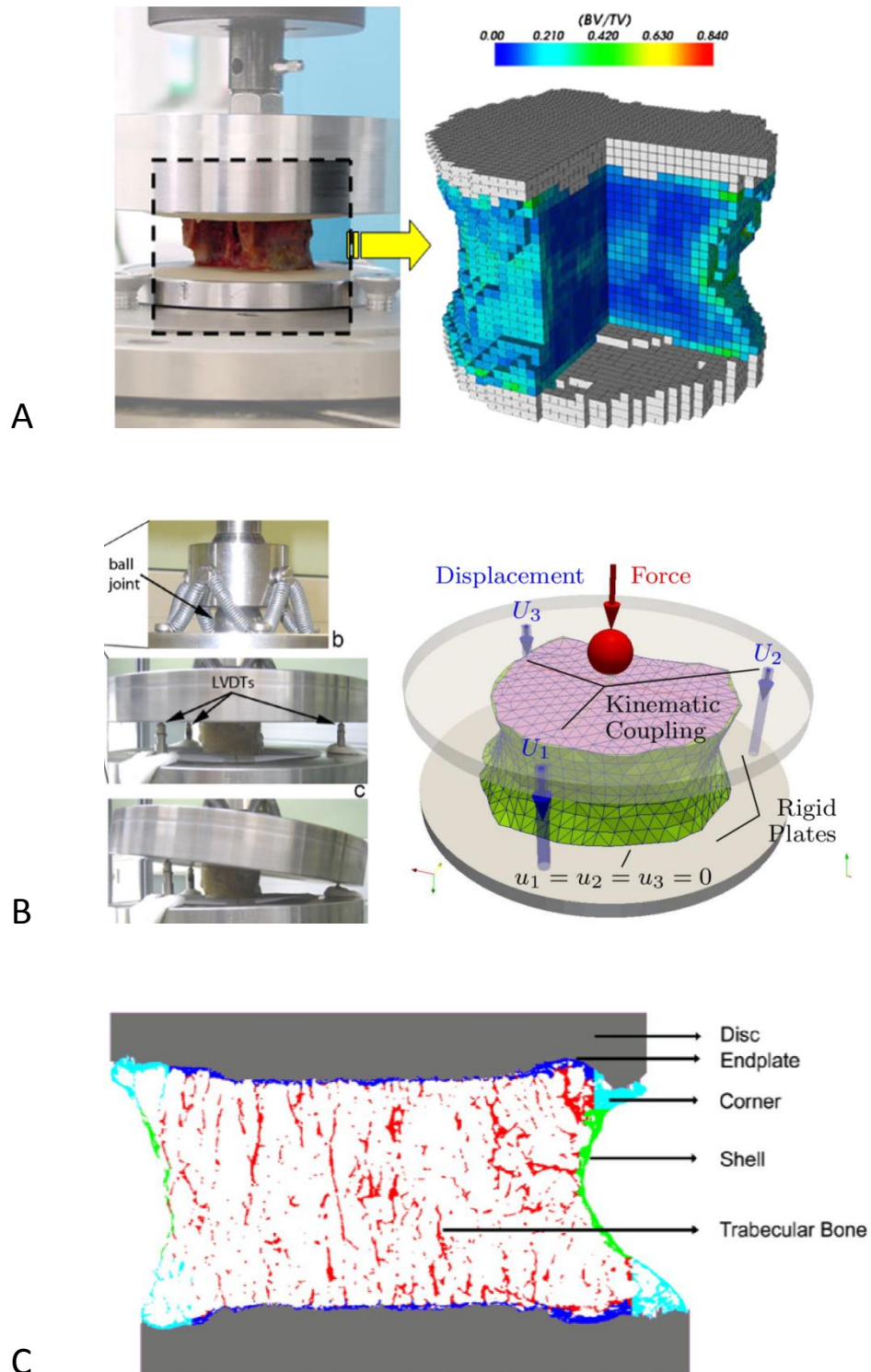


Fig. 8. Types of FE models of the vertebral body and boundary conditions. A. In vitro compression and QCT-based voxel model of an embedded vertebral body (Chevalier et al. 2009), B. In vitro compression and HRpQCT-based smooth model of a vertebral section (Dall'Ara et al. 2010, Pahr et al. 2012b) and C. μ CT-based FE model of a vertebral body surrounded by intervertebral discs (Eswaran et al. 2007).

softening and densification (Hosseini et al. 2012) or bone remodelling (Doblaré and Garcia 2002, Homminga et al. 2011) besides the bone anisotropy (Carretta et al. 2013). Besides, the smooth models usually run on a standard PC (Pahr et al. 2009).

To be reliable, the models require proper validations. Even if the *in vitro* settings do not mimic perfectly the *in vivo* conditions, the physiological conditions are too complex to allow an easy reproducibility (Cristofolini et al. 2010). Hence, most models are validated by comparing the FE predictions of vertebral strength to the experimental fracture load under axial compression, which remains the loading of choice. The validation of the FE models is usually performed with endplates embedded in PMMA (Chevalier et al. 2009, Sapin de Brosse et al. 2012) or without endplates (Dall'ara et al. 2010, Pahr et al. 2012b) to have well-defined boundary conditions. Few authors decided to integrate intervertebral disc models in their FE models of vertebral bodies (Homminga et al. 2004, Eswaran et al. 2006, Eswaran et al. 2007, Fields et al. 2010, Homminga et al. 2011, Erdem et al. 2011) but different types of vertebral fractures are induced by various grade of degeneration of the neighbouring discs (Seymour et al. 1998, Lee 2000, Ortiz et al. 2011).

4. Conditions of the intervertebral disc

4.1 Intervertebral disc degeneration

The first studies about the mechanical behaviour of the lumbar spine reported abnormal motions in elderly subjects (Panjabi et al. 1994). The degenerative condition is held responsible for changes in the spine biomechanics potentially leading to low back pain. The degenerative alterations are illustrated on Fig. 10.

Notwithstanding the unclear pathogenesis, many morphological and biochemical alterations are reported for both nucleus and annulus. While early degeneration seems to increase the disc flexibility, a highly degenerated disc, thinner and dehydrated, tends to behave in a solid-like manner featuring a stiffer behaviour in compression and shear (Iatridis et al. 1997a, Iatridis et al. 1997b, Iatridis et al. 1998, Iatridis et al. 1999). The degenerative alterations impact not only the intervertebral mechanics with changes in stiffness (Haughton et al. 1999) and range of motion (Tanaka et al. 2001) but also the stress distribution on the underlying vertebra (Adams and Roughley 2006). As the disc narrows, the load is progressively shifted towards the peripheral posterior regions of the cortical

endplates until the posterior arch eventually carries most of the axial load (Pollintine et al. 2004) leading to a painful osteoarthritis of the facet joints (Robson-Brown et al. 2008).

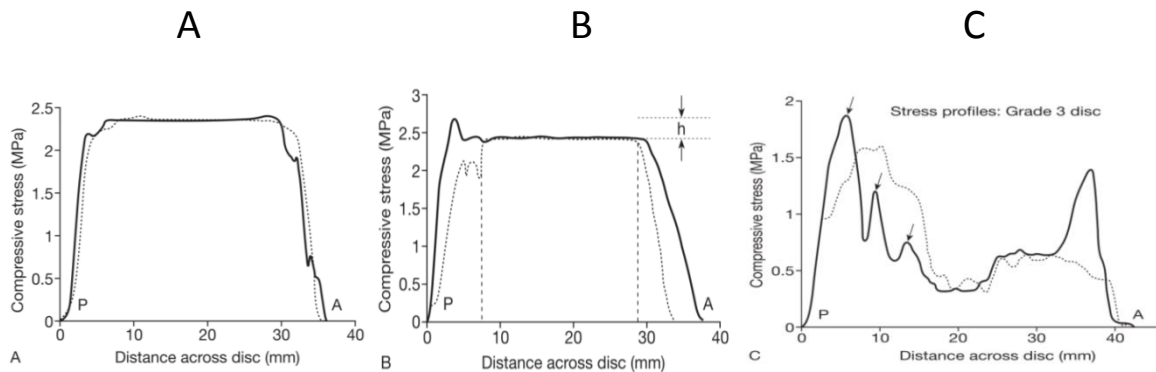


Fig. 9. Distribution of compressive stress along the midsagittal diameter of lumbar intervertebral discs under to 2 kN compression. A Young disc, B Middle-aged disc with stress concentration in the posterior annulus and C Degenerated disc with irregular stress profile (Adams and Roughley 2006).

Furthermore, the annulus fibrosus is sensitive to mechanical loading and fatigue (Adams and Dolan 2012). High shear between its layers causes delamination of its ply-laminate structure, large tension ruptures its collagen fibres while its matrix is cracked under tension exerted perpendicular to the fibres direction (Iatridis et al. 2004). Consequent radial tears in the posterior annulus can lead to protrusion and herniation of nucleus material in the vicinity of the nerve root causing pain (Veres et al. 2009, Marshall et al. 2010, Veres et al. 2010b, Michalek et al. 2012) when the IVD is undergoing torsion and flexion at high rate (Veres et al. 2008, Schollum et al. 2008, Veres et al. 2010a).

Besides, endplate-driven degenerative mechanism characterised by the presence of Schmorl's node, the migration of nucleus material through the innervated endplate under axial loading, can occur (Adams and Dolan 2012). Usually involving early degenerated discs and weak endplates (Hamanishi et al. 1994), it highlights the importance of the disc condition in the load transfer to a vertebral body, possibly osteoporotic.

To summarize, low back pain can be attributed to muscular and ligamentous strain, facet joint arthritis, or pressure exerted by the intervertebral disc on the annulus fibrosus, the cortical endplates or spinal nerves (Wise 2011). The direct surgical expenses (laminectomy*, discectomy*, lumbar spinal fusion*) reach roughly 15 billion dollars per year in the U.S. (Katz

2006). Even if in a majority of patients, the pathogenesis of back pain cannot be established with certainty, the early detection of disc degeneration is necessary to better select the patients who really need operative treatments while conservative procedures such as chiropractic, exercise, pain medication are usually prescribed (Zigler et al. 2013).

**Laminectomy: section of parts of the lamina (cf. Fig. 2) to decompress the neural root.*

**Discectomy: removal of herniated nucleus material pressing on the nerve root.*

**Lumbar spinal fusion: replacement of the IVD by a bone graft with eventually fusion between the vertebral bodies due to the natural bone growth and stabilisation via posterior instrumentation.*

4.2 Evaluation of the degeneration grade

Cryotome sections of cadaver intervertebral segments were first used to illustrate the disc degeneration (Thompson et al. 1990). Fortunately, a non-invasive assessment is possible via anatomical qualitative MRI (Jarvik et al. 2000, Haughton, 2006). However, despite an accurate description of the disc anatomy, those imaging methods are rather unspecific and highly dependent on the clinician's experience.

Briefly, MRI devices use the magnetic properties of a tissue to produce an image. The net magnetisation vector M_0 around which precess particles such as electrons and protons (hydrogen, H^+), abundant in the human body because of high water content, get aligned with the magnetic field B_0 generated by a powerful magnet. In this equilibrium state, the longitudinal component of the magnetization vector M_{long} equals M_0 and the transverse components are null (M_{tr}). This equilibrium is then disturbed by a variable magnetic field at resonance frequency (42.57 MHz). When this field is turned off, relaxation occurs, M_{tr} returns to 0, decreasing by 63% after T_2 ms while M_{long} returns to M_0 , increasing by 63% after T_1 ms (Suetens 2002). Considering the influence of water content and collagen structure on T_1 and T_2 relaxation times, an assessment based quantitative MRI is possible (Watanabe et al. 2007, Mwale et al. 2008, Marinelli et al. 2009) via $T_{1\rho}/T_2$ -weighted (Benneker et al. 2005) or T_2/T_2^* maps (Trattinig et al. 2010, Stelzeneder et al. 2012) -based grading schemes.

A healthy IVD is characterised by higher T_2/T_2^* in the nucleus but as it decreases dramatically because of the loss of water content in the nucleus, this relaxation time remains roughly constant in the annulus during the degenerative process (Watanabe et al.

2007, Welsch et al. 2011, Hoppe et al. 2012). Hence, High Intensity Zone in the annulus in T_2 images might be interpreted as herniated nuclear material, source of pain (Trattnig et al. 2010).

While clinicians visually evaluate the hydration of the disc based on the intensity and homogeneity of the signal, equivalent evaluations can be quantitatively achieved by measuring T_2/T_2^* at various locations (Hoppe et al. 2012, Stelzeneder et al. 2012), computing entropy of the signal and geometry-based criteria (Mayerhofer et al. 2012).

$T_{1\rho}$ is affected by low-frequency interactions between the water and glycosaminoglycan (GAG) nuclear content (Blumenkrantz et al. 2006, Johannessen et al. 2006). Thus, $T_{1\rho}$ measurements were performed to detect early changes. Other advanced methods such as Magnetization Transfer Ratio (MTR, Choi et al. 2011) and Apparent Diffusion Coefficient maps (ADC, Antoniou et al. 2004), sensible to collagen content or diffusion properties, can provide extra information about the structural integrity of the collagen network of the annulus fibrosus while Diffusion Tensor Imaging (DTI) is able to measure degree of anisotropy and the orientation of the collagen fibres of the annulus (Hsu et al. 1999).

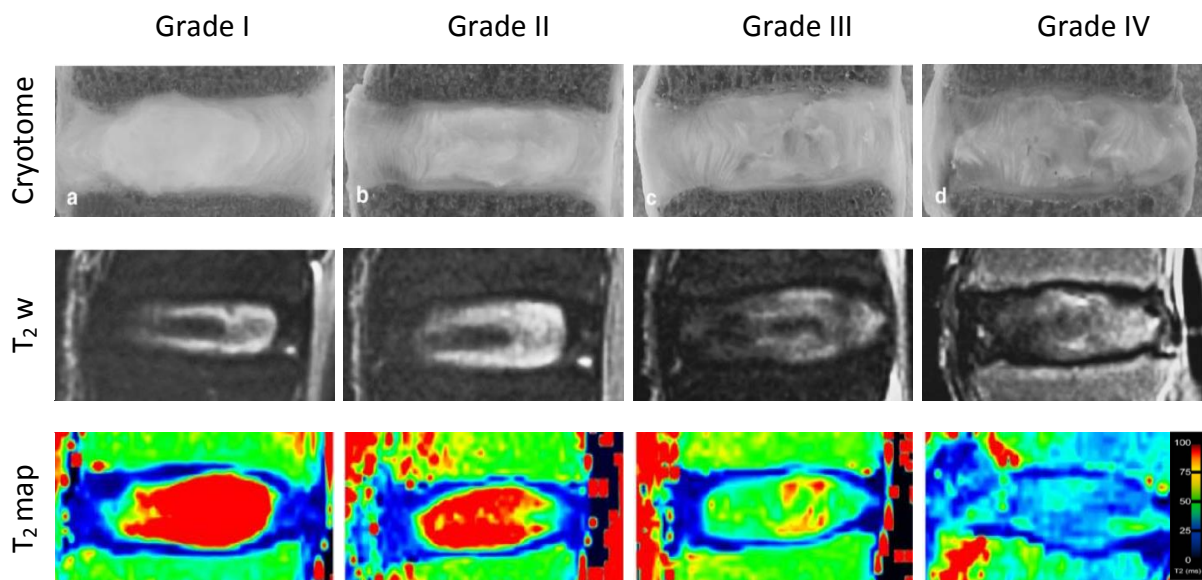


Fig. 10. Midsagittal cryomicrotome sections, T_2 weighted, Sagittal T_2 maps and axial T_2 maps of the intervertebral disc with disc degeneration from grades I to IV (Benneker et al. 2005, Stelzeneder et al. 2012, Watanabe et al. 2007).

4.3 Subject-specific finite element models of the intervertebral disc

FE models of the IVD are far from a clinical use and a step behind what is being done for the vertebral body in terms of subject-specific geometry, material properties and validation.

Indeed, the geometry is often simplified with dimensions of the annulus and nucleus taken from the literature (Galbusera et al. 2011, Malandrino et al. 2012) or guessed from the shape of the neighbouring vertebrae on CT (Moramarco et al. 2010, Homminga et al. 2012) or Dual Fluoroscopic images via 2 fluoroscopes positioned perpendicular to each other (Wang et al. 2012), the IVD being extruded from their cranial and caudal endplates. Considering the high impact of the disc's morphology on its mechanical response (Meijer et al. 2011, Niemeyer et al. 2012), it is rather surprising that only few authors based the geometry of their models on MRI images (Li et al. 2006, Swider et al. 2010, Castro Mateos et al. 2012).

Then, increasingly complex poroelastic models, valuable in terms of understanding of biochemical principles but hardly fitting a disc-specific framework and seldom validated, which limits clinical potential, are developed (Ehlers et al. 2009, Schroeder et al. 2010, Galbusera et al. 2011, Malandrino et al. 2012, Ateshian and Weiss 2013). On the other hand, most of the current models are able to simulate the anisotropy of the IVD, its heterogeneity and hyperelasticity, which is sufficient to represent the quasi-static non-linear response of the disc (Moramarco et al. 2010, Homminga et al. 2012), simulate its prolapse (Schmidt et al. 2007), the initiation of tears in the annulus (Schmidt et al. 2009) and analyse the structural response of the disc to impact loading (Marini et al. 2012). Few attempts of unspecific damage model (Qasim et al. 2012) and degeneration-wise disc material properties (Hussain et al. 2012) can be reported but nothing comparable to the CT-based bone material models. Notwithstanding the numerous quantitative MRI sequences developed for the IVD evaluation or detect deflection, the authors hardly calibrate the material properties of their models on MRI data.

Finally, most authors compare the FE predictions of their models against similar experimental results found in the literature (Schmidt et al. 2007, Pérez del Palomar et al. 2008, Moramarco et al. 2010), which is not trustworthy considering the large standard deviation in experimental results due to the wide diversity in degree of degeneration, loading history or geometry of the IVD hardly taken into account (Jones et al. 2008).

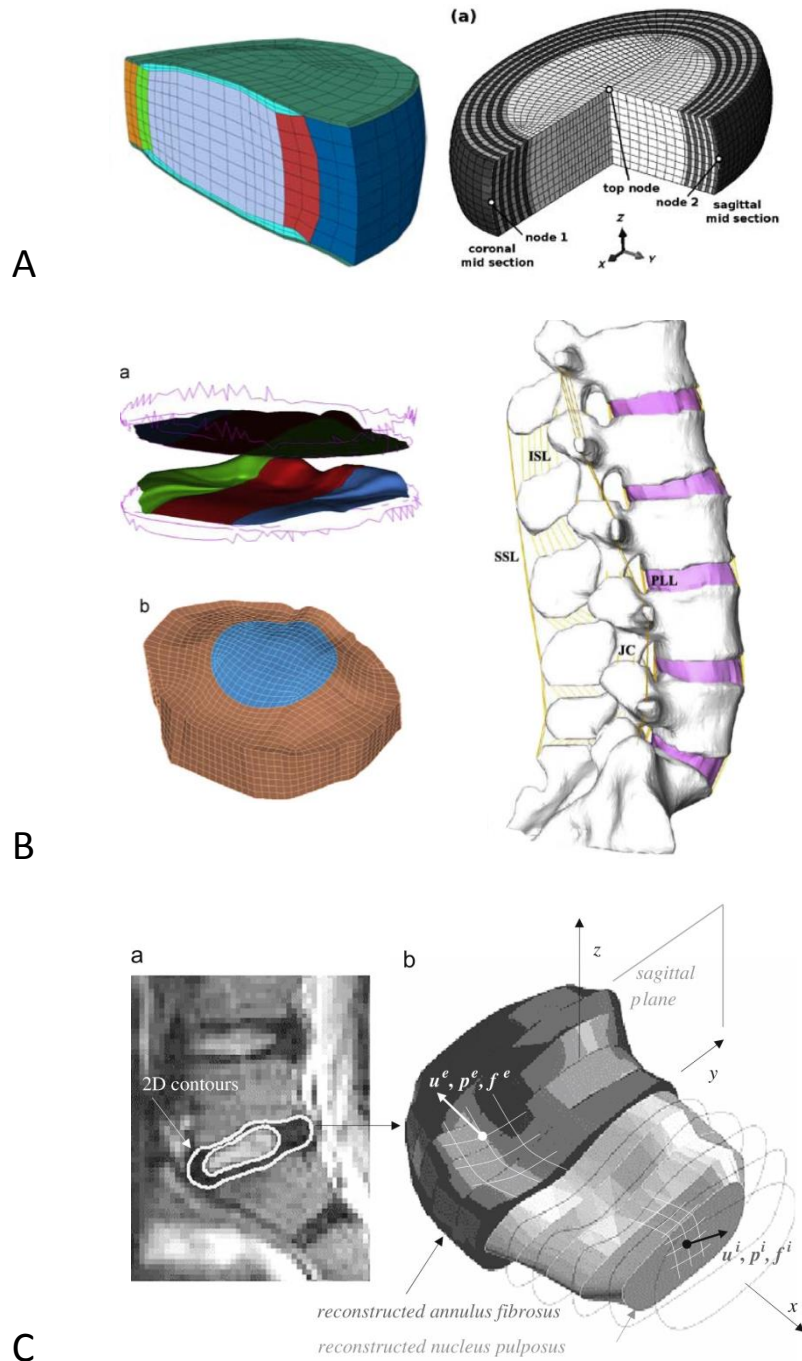


Fig. 11. Examples of FE models of IVD with different purposes. A. Poroelastic (Malandrino et al. 2012) and hyperelastic (Marini et al. 2012) models with simplified geometry to study the biochemical and biomechanical principles, B. Hyperelastic disc model generated from the geometry of the CT-based cortical endplates to simulate the mechanical response of the lumbar spine (Moramarco et al. 2010), C. MRI-based intervertebral disc geometry with substructuring (Swider et al. 2010)

Indeed, while it is common to normalise the apparent stiffness of bone (Mosekilde et al. 1987), muscle (Ryan et al. 2011) or tendon (Fouré et al. 2012) using cross-sectional area for instance, only in few authors normalised the measurements of IVD stiffness by the disc geometry (Elliott and Sarver 2004, Beckstein et al. 2008, Showalter et al. 2012).

Conversely, examples of model validation against *in vivo* kinematics using Dual Fluoroscopic images show great promises (Wang et al. 2012). Disc-specific geometry, material properties and direct validation of FE models are required for any models to have a clinical benefit (Kallemeyn et al. 2010, Gefen 2012).

5. Objectives of the thesis

Considering the clinical relevance of accurate diagnosis tools and the limitations of the current state of the art for vertebral strength and intervertebral disc degeneration assessment, the goal of this thesis is twofold.

The first aim is to evaluate the effect of the boundary conditions on the prediction of vertebral strength and damage by CT-based FE models:

1. highlight the bias induced by the choice of rigid boundary conditions in the models
2. show the potential influence of disc degeneration on the FE results

The second goal pertains to the improvements of the current evaluation of the IVD:

3. propose a normalisation protocol for the disc's stiffness with respect to its morphology
4. introduce a MRI-based methodology to evaluate the biomechanical status of the intervertebral disc.

6. Outline of the thesis

Chapter 1 presented the anatomy of the lumbar spine and provided the state of the art for vertebral strength and intervertebral disc degeneration assessment and finite element models.

Chapter 2 is a FE study focusing on the comparison of two rigid boundary conditions commonly applied on the cortical endplates during experimental compression test of cadaver vertebral bodies, vertebral sections and PMMA embedded vertebral bodies. The 12 QCT-based voxel FE models compute almost identical vertebral strengths and damage distributions in both cases.

Chapter 3 highlights the large influence of the intervertebral disc's compliance on the vertebral strength, damage distribution and damage initiation. Compression tests were simulated on two extreme cases using 12 HRpQCT-based homogenized smooth models, idealistic healthy disc or PMMA embedding mimicking a highly degenerated disc.

Chapter 4 introduces a new protocol for the normalisation of the stiffness of intervertebral discs loaded in compression, torsion, lateral bending and flexion/extension using accurate MRI-based data to account for its morphology. This protocol, tested on 20 FE models with various dimensions, was applied on the stiffness of 14 human lumbar intervertebral discs.

Chapter 5 proposes a new criterion for disc degeneration from Axial T_2 maps. Otsu threshold computed in the posterior annulus fibrosus is related to the disc mechanics and meet objectivity and simplicity required for a clinical application. The degeneration grades of 14 human lumbar intervertebral discs evaluated using MRI data and quantitative T_2 measures were related to the specimens' stiffness in compression, torsion, lateral bending and flexion/extension.

Chapter 6 summarises the strengths and limitations of each study and presents further improvements and applications.

References

- Adams M.A. and Roughley P.J. 2006. What is Intervertebral Disc Degeneration, and What Causes It? *Spine*. 31(18): 2151–2161
- Ateshian G.A. and Weiss J.A. 2013. Finite Element Modeling of Solutes in Hydrated Deformable Biological Tissues. *Computer Models in Biomechanics*. 231-249
- Antoniu J. [et al.]. 2004. Apparent diffusion coefficient of intervertebral discs related to matrix composition and integrity *Magn Reson.Imaging*. 7(22): 963-972
- Beckstein J.C., Sen S., Schaer T.P., Vresilovic E.J. and Elliott D.M. 2008. Comparison of animal discs used in disc research to human lumbar disc axial compression mechanics and glycosaminoglycan content. *Spine*. 33:E166–E173
- Blumenkrantz G. [et al.]. 2006. A feasibility study of in vivo T1rho imaging of the intervertebral disc *Magn Reson.Imaging*. 8(24): 1001- 1007
- Bogduk, N. 2005. *Clinical anatomy of the lumbar spine and sacrum*. Churchill Livingstone.
- Boutroy S., Hans D., Sornay-Rendu E., Vilayphiou N., Winzenrieth R., Chapurlat R. 2013. Trabecular bone score improves fracture risk prediction in non-osteoporotic women: the OFELY study. *Osteoporos Int*. 24:77–85
- Carretta R., Lorenzetti S. and Müller R. 2013. Towards patient-specific material modeling of trabecular bone post-yield behaviour. *Int. J. Numer. Meth. Biomed. Engng*. 29:250–272
- Castro Mateos I., Humbert L., Whitmarsh T., Lazary A., Del Rio Barquero L. M. and Frangi A.F. 2012. 3D reconstruction of intervertebral discs from T1-weighted magnetic resonance images. In *Biomedical Imaging (ISBI), 2012 9th IEEE International Symposium on* (pp. 1695-1698). IEEE
- Chevalier Y., Zysset P.K. 2012. A patient-specific computer tomography-based finite element methodology to calculate the six dimensional stiffness matrix of human vertebral bodies. *J Biomech Eng*. 134(5)
- Chevalier Y., Pahr D. and Zysset P. K. 2009. The role of cortical shell and trabecular fabric in finite element analysis of the human vertebral body. *Journal of biomechanical engineering*. 131(11): 111003
- Choi J.A. and Gold G.E. 2011. MR imaging of articular cartilage physiology. *Magn Reson. Imaging Clin N Am*. 2(19): 249-282
- Crawford R.P., Cann C.E. and Keaveny T.M. 2003. Finite element models predict in vitro vertebral body compressive strength better than quantitative computed tomography. *Bone* 33(4): 744-750
- Cristofolini L., Schileo E., Juszczyk M., Taddei F., Martelli S. and Viceconti M. 2010. Mechanical testing of bones: the positive synergy of finite-element models and in vitro experiments. *Philosophical transactions. Series A, Mathematical, physical, and engineering sciences* 368(1920): 2725-2763
- Dall'Ara, E., Schmidt, R., Pahr, D., Varga, P., Chevalier, Y., Patsch, J., Kainberger, F. and Zysset, P. 2010, A nonlinear finite element model validation study based on a novel experimental technique for inducing anterior wedge-shape fractures in human vertebral bodies in vitro. *Journal of biomechanics* 43(12): 2374-2380
- Doblaré M., García J.M. 2002. Anisotropic bone remodelling model based on a continuum damage–repair theory. *Journal of Biomechanics*. 35(1):1–17

- Dubousset J., Charpak G., Wafa Skalli W., Deguise J. and Gabriel Kalifa G. 2010. Eos: a new imaging system with low dose radiation in standing position for spine and bone & joint disorders. *Journal of Musculoskeletal Research*. 13 (1): 1-12
- Ehlers W., Karajan N. and Markert B. 2009. An extended biphasic model for charged hydrated tissues with application to the intervertebral disc. *Biomech Model Mechanobiol*. 8:233–251
- Elliott D.M. and Sarver J.J. 2004. Young investigator award winner: validation of the mouse and rat disc as mechanical models of the human lumbar disc. *Spine*. 29:713–722
- Erdem I., Truumees E. and van der Meulen M.C.H. 2011. Simulation of the behaviour of the L1 vertebra for different material properties and loading conditions. *Computer Methods in Biomechanics and Biomedical Engineering*, iFirst article. 1–11
- Eswaran S.K., Gupta A., Adams M.F. and Keaveny T.M. 2006. Cortical and trabecular load sharing in the human vertebral body. *Journal of bone and mineral research*. 21(2): 307-314
- Eswaran S.K., Gupta A. and Keaveny T.M. 2007. Locations of bone tissue at high risk of initial failure during compressive loading of the human vertebral body. *Bone* 41(4): 733-739
- Fields A.J., Lee G.L. and Keaveny T.M. 2010, Mechanisms of initial endplate failure in the human vertebral body. *Journal of biomechanics* 43(16): 3126-3131
- Fouré A., Cornu C. and Nordez A. 2012. Is tendon stiffness correlated to the dissipation coefficient? *Physiol. Meas.* 33:N1–N9
- Galbusera F., Schmidt H., Neidlinger-Wilke C., Gottschalk A., Wilke H.J. 2011. The mechanical response of the lumbar spine to different combinations of disc degenerative changes investigated using randomized poroelastic finite element models. *Eur Spine J*. 20:563–571
- Gefen A. 2012. Patient-Specific Modeling in Tomorrow's Medicine. Springerlink. *Studies in Mechanobiology, Tissue Engineering and Biomaterials*.
- Glaser D.A., Doan J. and Newton P.O. 2012. Comparison of 3-Dimensional Spinal Reconstruction Accuracy: Biplanar Radiographs With EOS Versus Computed Tomography. *Spine*. 37(16):1391–1397
- Glüer C.C., Marin F., Ringe J.D., Hawkins F., Möricke R., Papaioannu N., Farahmand P., Minisola S., Martínez G., Nolla J.M., Niedhart C., Guañabens N., Nuti R., Martín-Mola E., Thomasius F., Kapetanios G., Peña J., Graeff C., Petto H., Sanz B., Reisinger A., Zysset P.K. 2013. Comparative Effects of Teriparatide and Risedronate in Glucocorticoid-Induced Osteoporosis in Men: 18-Month Results of the EuroGIOPs Trial. *Journal of Bone and Mineral Research*
- Graeff C., Marin F., Petto H., Kayser O., Reisinger A., Peña J., Zysset P., Glüer C.. 2013. High resolution quantitative computed tomography-based assessment of trabecular microstructure and strength estimates by finite-element analysis of the spine, but not DXA, reflects vertebral fracture status in men with glucocorticoid-induced osteoporosis. *Bone*. 52: 568–577
- Graeff C, Chevalier Y, Charlebois M, Varga P, Pahr D, Nickelsen TN, Morlock MM, Glüer CC and Zysset PK. 2009. Improvements in vertebral body strength under teriparatide treatment assessed in vivo by finite element analysis: results from the EUROFORS study. *J Bone Miner Res*. 24(10):1672-80
- Griffith J.F., Genant H.K. 2008. Bone mass and architecture determination: state of the art. *Best Practice & Research Clinical Endocrinology & Metabolism*. 22(5):737–764

- Hamanishi C, Kawabata T, Yosii T, et al. 1994. Schmorl's nodes on magnetic resonance imaging. Their incidence and clinical relevance. *Spine*. 19:450–453
- Haughton V.M., Lim T.H. and An H. 1999. Intervertebral disk appearance correlated with stiffness of lumbar spinal motion segments. *AJNR Am J Neuroradiol*. 20:1161-1165
- Haughton V. 2006. Imaging intervertebral disc degeneration *J.Bone Joint Surg.Am*. 88. Suppl 2: 15-20
- Homminga J., and Van-Rietbergen B., Lochmüller E. M., Weinans H., Eckstein F. and Huiskes R. 2004. "The Osteoporotic Vertebral Structure Is Well Adapted to the Loads of Daily Life, but Not to Infrequent "Error" Loads". *Bone*. 343: 510–516
- Homminga J., Aquarius R., Bultink V.E., Jansen C.T.J., Verdonschot N. 2011. Can vertebral density changes be explained by intervertebral disc degeneration? *Med Eng Phys*. 101016/jmedengphy201108003.
- Hoppe S., Quirbach S., Mamisch T.C., Krause F.G., Werlen S. and Benneker L.M. 2012. Axial T2* mapping in intervertebral discs: a new technique for assessment of intervertebral disc degeneration. *Eur Radiol*. 22:2013–2019
- Hosseini H.S., Pahr D.H. and Zysset P.K. 2012. Modelling and experimental validation of trabecular bone damage, softening and densification under large compressive strains *Journal of the Mechanical Behavior of Biomedical Materials*. 15:93-102
- Hussain M., Natarajan R.N, An H.S., Andersson G.B.J. 2012. Progressive disc degeneration at C5–C6 segment affects the mechanics between disc heights and posterior facets above and below the degenerated segment: A flexion–extension investigation using a poroelastic C3–T1 finite element model. *Medical Engineering & Physics*. 34. 552–558
- Hsu E. W. et Setton L. A. 1999. Diffusion tensor microscopy of the intervertebral disc annulus fibrosus *Magn Reson.Med*. 5(41): 992-999
- Iatridis J.C. [et al.]. 1997a. Alterations in the mechanical behavior of the human lumbar nucleus pulposus with degeneration and aging. *J Orthop Res*. 2(15): 318-322
- Iatridis J.C. [et al.]. 1997b. The viscoelastic behavior of the non-degenerate human lumbar nucleus pulposus in shear. *J Biomech*. 10(30): 1005-1013
- Iatridis J.C. [et al.]. 1998. Degeneration affects the anisotropic and nonlinear behaviors of human annulus fibrosus in compression. *J Biomech*. 6(31): 535-544
- Iatridis J.C. [et al.]. 1999. Shear mechanical properties of human lumbar annulus fibrosus. *J Orthop Res*. 5(17): 732-737
- Iatridis J.C. [et al.]. 2009b. Localized Intervertebral Disc Injury Leads to Organ Level Changes in Structure, Cellularity, and Biosynthesis. *Cell Mol Bioeng*. 3(2): 437-447
- Iatridis J.C. and Iolo G. 2004. Mechanisms for mechanical damage in the intervertebral disc annulus fibrosus. *J Biomech*. 8(37): 1165-1175
- Illes T. and Somoskeoy S. 2012. The EOS imaging system and its uses in daily orthopaedic practice. *International Orthopaedics*. 36:1325–1331
- Jarvik J.G. and Deyo R.A. 2000. Imaging of lumbar intervertebral disk degeneration and aging, excluding disk herniations. *Radiologic Clinics of North America*. 6(8): 1255-66
- Johannessen W. [et al.]. 2006. Assessment of human disc degeneration and proteoglycan content using T1rho-weighted magnetic resonance imaging. *Spine*. 11(31): 1253-1257
- Kallemeyn N. [et al.]. 2010. Validation of a C2-C7 cervical spine finite element model using specimen-specific flexibility data. *Med Eng Phys*. 5(32): 482-489

- Kanis J.A., McCloskey E.V., Johansson H., Oden A., Melton III L.J., Khaltsev N. 2008. A reference standard for the description of osteoporosis. *Bone*. 42: 467 – 475
- Katz J.N. 2006. Lumbar Disc Disorders and Low-Back Pain: Socioeconomic Factors and Consequences. *The Journal Bone & Joint Surgery*. 88(A). Suppl. 2
- Keaveny T.M., Donley D.W., Hoffmann P.F., Mitlak B.H., Glass E.V., San Martin J.A. 2007. Effects of teriparatide and alendronate on vertebral strength as assessed by finite element modeling of QCT scans in women with osteoporosis. *J Bone Miner Res* 22:149–157
- Kurutz M. and L. Oroszvary L. 2010. Finite element analysis of weightbath hydrotraction treatment of degenerated lumbar spine segments in elastic phase. *J Biomech*. 43(3):433–441
- Lee K.S. 2000. The Effect of Disc Degeneration in Osteoporotic Vertebral Fracture. *J Korean Soc Spine Surg*. 7(4):558-564
- Li H. and Wang Z. 2006. Intervertebral disc biomechanical analysis using the finite element modeling based on medical images. *Comput Med Imaging Graph*. 7(30): 363-370.
- Malandrino A., Noailly J. and Lacroix D. 2012. Regional annulus fibre orientations used as a tool for the calibration of lumbar intervertebral disc finite element models. *Comput Methods Biomech Biomed Engin*. DOI: 10.1080/10255842.2011.644539
- Marinelli N.L, Haughton V.M., Munoz A. and Anderson P.A. 2009. T2 Relaxation Times of Intervertebral Disc Tissue Correlated With Water Content and Proteoglycan Content. *Spine*. 34(5):520 –524
- Marini G. and Ferguson S.J. 2012. Nonlinear numerical analysis of the structural response of the intervertebral disc to impact loading. *Computer Methods in Biomechanics and Biomedical Engineering* iFirst article, 2012, 1–10
- Mayerhofer M.E., Stelzener D., Bachbauer W., Welsch G.H, Mamisch T.C., Szczypinski P., Weber M., Peters N., Fruehwald-Pallamar J., Puchner S. and Siegfried Trattng. 2012. Quantitative analysis of lumbar intervertebral disc abnormalities at 3.0 Tesla: value of T2 texture features and geometric parameters. *NMR Biomed*. 25: 866–872
- Meijer Gerdine JM. [et al.]. 2011. Influence of interpersonal geometrical variation on spinal motion segment stiffness: implications for patient-specific modeling. *Spine*. 14(36): E929-E935
- Michalek A.J. and Iatridis J.C. 2012. Height and torsional stiffness are most sensitive to annular injury in large animal intervertebral discs. *Spine J*. 5(12): 425-432
- Michalek A.J., Gardner-Morse M.G., Iatridis J.C. 2012b. Large residual strains are present in the intervertebral disc annulus fibrosus in the unloaded state. *Journal of Biomechanics*. 45: 1227–1231
- Moramarco V., Perez del Palomar A., Pappalettere C., Doblaré M. 2010. An accurate validation of a computational model of a human lumbosacral segment. *J Biomech*. 43:334–342
- Mosekilde L., Mosekilde L. and Danielsen C.C. 1987. Biomechanical competence of vertebral trabecular bone in relation to ash density and age in normal individuals. *Bone*. 8:79–85
- Mwale F., Iatridis J.C., Antoniou J. 2008. Quantitative MRI as a diagnostic tool of intervertebral disc matrix composition and integrity. *EurSpineJ*. 17(4):S432–S440
- Niemeyer F., Wilke H.J. et Schmidt H. 2012. Geometry strongly influences the response of numerical models of the lumbar spine—a probabilistic finite element analysis. *J Biomech*. 8(45): 1414-1423

- Ortiz A.O. and Bordia R. 2011. Injury to the vertebral endplate-disk complex associated with osteoporotic vertebral compression fractures. *Am J Neuroradiol.* 32:115–20.
- Panjabi M.M., Oxland T.R., Yamamoto I., Crisco J.J. 1994. Mechanical behavior of the human lumbar and lumbosacral spine as shown by three-dimensional load–displacement curves. *J Bone Joint Surg.* 76:413-424
- Pahr D.H., Dall'Ara E., Varga P. and Zysset P.K. 2012a. HR-pQCT-based homogenised finite element models provide quantitative predictions of experimental vertebral body stiffness and strength with the same accuracy as μ FE models. *Computer Methods in Biomechanics and Biomedical Engineering.* 15(7): 711-720
- Pahr D.H., Schwiedrzik J., Dall'Ara E., Zysset P.K. 2012b. Clinical versus pre-clinical FE models for vertebral body strength predictions. *Journal of the Mechanical Behavior of Biomedical Materials.* doi: 10.1016/j.jmbbm.2012.11.018
- Pahr D.H. and Zysset P.K. 2009. A comparison of enhanced continuum fe with micro fe models of human vertebral bodies. *J Biomech.* 424:455-462.
- Pérez_del_Palomar A., Calvo B. et Doblaré M. 2008. An accurate finite element model of the cervical spine under quasi-static loading. *J Biomech.* 3(41): 523-531
- Pollintine P., Przybyla A.S., Dolan P. 2004. Neural arch load-bearing in old and degenerated spines. *J Biomech.* 37: 197–204.
- Prithvi R.P. 2008. *Intervertebral Disc: Anatomy-Physiology-Pathophysiology-Treatment.* Pain Practice. 8(1): 18–44
- Qasim M., Natarajan R.N, An H.S., Andersson G.B.J. 2012. Initiation and progression of mechanical damage in the intervertebral disc under cyclic loading using continuum damage mechanics methodology: A finite element study. *JBiomech.* 45:1934–1940
- Robson-Brown K., Pollintine P., Adams M.A. 2008. Biomechanical implications of degenerative joint disease in the apophyseal joints of human thoracic and lumbar vertebrae. *Am J Phys Anthropol* 136, 318–326
- Roh J. S., Teng A. L., Yoo J. U., Davis J., Furey C., Bohlman H. H.. 2005. *Degenerative disorders of lumbar and cervical spine.* Orthopedic clinics of North America 36: 255-262
- Roux J.P., Wegrzyn J., Boutroy S., Bouxsein M.L., Hans D., Chapurlat R. 2013. The predictive value of trabecular bone score (TBS) on whole lumbar vertebrae mechanics: an ex vivo study. *Osteoporos Int.* epub
- Ryan E.D., Thompson B.J., Herda T.J., Sobolewski E.J., Costa P.B., Walter A.A. and Cramer J.T. 2011. The relationship between passive stiffness and evoked twitch properties: the influence of muscle CSA normalization. *Physiol. Meas.* 32:677–686
- Sapin de Broses E., Jolivet E., Travert C., Mitton D., and Skalli W. 2012. Prediction of the vertebral strength using a finite element model derived from low-dose biplanar imaging benefits of subject-specific material properties. *Spine.* 37(3): 156–162
- Schmidt Hendrik [et al.]. 2007. The risk of disc prolapses with complex loading in different degrees of disc degeneration - a finite element analysis. *Clin Biomech.* 9(22): 988-998.
- Schmidt H., Heuer F. et Wilke H.J. 2009. Dependency of disc degeneration on shear and tensile strains between annular fiber layers for complex loads. *Med Eng Phys.* 6(31): 642-649
- Schollum M.L., Robertson P.A. et Broom N.D. 2008. ISSLS prize winner: microstructure and mechanical disruption of the lumbar disc annulus: part I: a microscopic investigation of the translamellar bridging network. *Spine.* 25(33): 2702-2710

- Schünke M., Schulte E., Schumacher U., Voll M., Wesker M., 2007. *Allgemein Anatomie und Bewegungssystem. PROMETHEUS LernAtlas der Anatomie. 2. Auflage – überarbeitet und erweitert!* © 2005, 2007 Georg Thieme Verlag. ISBN 978 – 3 – 13 – 139522 – 1.
- Schwiedrzik J.J. et Zysset P.K. 2012. An anisotropic elastic-viscoplastic damage model for bone tissue. *Biomech Model Mechanobiol.* 12(2):201-13
- Seymour R., Williams L.A., Rees J.I., Lyons K. and Lloyd D.C.F. 1998. Magnetic Resonance Imaging of Acute Intraosseous Disc Herniation. *Clin Radiol.* 53:363-368
- Showalter B.L., Beckstein J.C., Martin J.T., Beattie E.E., Espinoza Orías A.A., Schaer T.P., Vresilovic E.J. and Elliott D.M. 2012. Comparison of animal discs used in disc research to human lumbar disc. *Spine.* 7:E900–E907
- Stelzeneder D., Welsch G.H., Kovács B.K., Goed S., Paternostro-Sluga T., Vlychou M., Friedrich K., Mamisch T.C. and Trattnig S. 2012. Quantitative T2 evaluation at 3.0 T compared to morphological grading of the lumbar intervertebral disc: A standardized evaluation approach in patients with low back pain. *European Journal of Radiology.* 81:324-330
- Suetens P. 2002. *Fundamentals of medical imaging.* Cambridge University Press.
- Swider P., Pedrono A., Ambard D., Accadbled F., Sales de Gauzy J. 2010. Substructuring and poroelastic modelling of the intervertebral disc. *J Biomech.* 43:1287-1291.
- Tanaka N., An H.S., Lim T., Fujiwara A., Jeon C., Houghton V.M. 2001. The relationship between disc degeneration and flexibility of the lumbar spine. *The Spine Journal.* 1:47–56
- Thompson J.P., Pearce R.H., Schechter M.T., Adams M.E., Tsang I.K., Bishop P.B. 1990. Preliminary evaluation of a scheme for grading the gross morphology of the human intervertebral disc. *Spine* 15:411–415
- Trattnig S., Stelzeneder D., Goed S., Reissegger M., Mamisch T.C., Paternostro-Sluga T., Weber M., Szomolanyi P., Welsch G.H. 2010. Lumbar intervertebral disc abnormalities: comparison of quantitative T2 mapping with conventional MR at 3.0T. *Eur Radiol.* 20:2715–2722
- Veres S.P., Robertson P.A. et Broom N.D. D. 2008. ISSLS prize winner: microstructure and mechanical disruption of the lumbar disc annulus: part II: how the annulus fails under hydrostatic pressure. *Spine.* 25(33): 711-2720
- Veres S.P., Robertson P.A. et Broom N.D. 2009. The morphology of acute disc herniation: a clinically relevant model defining the role of flexion. *Spine.* 21(34): 2288-2296
- Veres S.P., Robertson P.A. et Broom N.D. 2010a. ISSLS prize winner: how loading rate influences disc failure mechanics: a microstructural assessment of internal disruption. *Spine.* 21(35): 1897-1908
- Veres S.P., Robertson P.A. et Broom N.D. D. 2010b. The influence of torsion on disc herniation when combined with flexion. *Eur Spine J.* 9(19): 1468-1478
- Wang S., Park W.M., Gadikota H.R., Miao J., Kim Y.H., Kirkham B. Wood & Li G. 2012. A combined numerical and experimental technique for estimation of the forces and moments in the lumbar intervertebral disc. *Computer Methods in Biomechanics and Biomedical Engineering.* iFirst
- Watanabe A., Benneker L.M., Boesch C., Watanabe T., Obata T., Anderson S.E. 2007. Classification of Intervertebral Disk Degeneration with Axial T2 Mapping. *AJR.* 189:936–942
- Watts N.B. 2001. Osteoporotic vertebral fractures. *Neurosurg Focus.* 10 (4): 12

- Welsch G.H, Trattng S., Paternostro-Sluga T., Bohndorf K., Goed S., Stelzeneder D., Mamisch T.C. 2011. Parametric T2 and T2* mapping techniques to visualize intervertebral disc degeneration in patients with low back pain: initial results on the clinical use of 3.0 Tesla MRI. *Skeletal Radiol.* 40:543–551
- Wise C. 2011. Back Pain and Common Musculoskeletal Problems. *ACP Medicine.*
- White A.A. and Panjabi M.M. 1990. *Clinical biomechanics of the spine (Vol. 446).* Philadelphia: Lippincott.
- Wolfram U., Wilke H.J., Zysset P.K. 2011. Damage accumulation in vertebral trabecular bone depends on loading mode and direction. *Journal of Biomechanics.* 44(6):1164–1169.

Chapter 2: The influence of the endplate on vertebral strength

From the manuscript

Removal of the cortical endplates has little effect on ultimate load and damage distribution in QCT-based voxel models of human lumbar vertebrae under axial compression

G. Maquer ^a, E. Dall'Ara ^a and P.K. Zysset ^b

^a Institute of Lightweight Design and Structural Biomechanics, Vienna University of Technology, Austria

^b Institute of Surgical Technology and Biomechanics, University of Bern, Switzerland

Published in: Journal of Biomechanics 45 (2012) 1733–1738

DOI: <http://dx.doi.org/10.1016/j.jbiomech.2012.03.019>

Abstract

Every year, 500'000 osteoporotic vertebral compression fractures occur in Europe. Quantitative computed tomography (QCT)-based Finite Element (FE) voxel models predict ultimate force whether they simulate vertebral bodies embedded in polymethylmethacrylate (PMMA) or vertebral sections with both endplates removed. To assess the effect of endplate removal in those predictions, non-linear FE analyses of QCT-based voxel models of human vertebral bodies were performed. High Resolution pQCT images of 11 human lumbar vertebrae without posterior elements were coarsened to clinical resolution and bone volume fraction was used to determine the elastic, plastic and damage behaviour of bone tissue. Three model boundary conditions (BCs) were chosen: the endplates were cropped (BC1, BC2) or voxel layers were added on the intact vertebrae to mimic embedding (BC3). For BC1 and BC3, the bottom nodes were fully constrained and the top nodes were constrained transversely while both node sets were free transversely for BC2. Axial displacement was prescribed to the top nodes. In each model, we compared ultimate force and damage distribution during post-yield loading. The results showed that ultimate forces obtained with BC3 correlated perfectly with those computed with BC1 ($R^2=0.9988$) and BC2 ($R^2=0.9987$), but were in average 3.4% lower and 6% higher respectively. Moreover, good correlation of damage distribution calculated for BC3 was found with the one of BC1 ($R^2=0.92$) and BC2 ($R^2=0.73$). This study demonstrated that voxel models of vertebral sections provide the same ultimate forces and damage distributions than embedded vertebral bodies for less preprocessing and computing time.

Keywords: Boundary Conditions, Finite Element Analysis, Quantitative Computed Tomography, Osteoporosis, Vertebral Strength

1. Introduction

Osteoporosis is characterized by low bone mass and degradation in bone architecture (Kanis et al. 2006). Dual energy X-ray Absorptiometry (DXA) is used for non-invasive fracture prediction by measuring areal BMD (Griffith and Genant 2008), but geometry and local variation in bone density are not included in these measurements (McDonnell et al. 2007).

Subject-specific voxel finite element models generated from QCT images with a clinical resolution of about 1mm (Engelke et al. 2008) are the current state of art for vertebral fracture risk prediction *in vivo* (Ruffoni and vanLenthe 2011). Geometry and BMD are taken into account and the simulations run on standard PCs, but the loading conditions should be realistic and allow their experimental validation (Cristofolini et al. 2010). Axial compression is often chosen for its reproducibility (Buckley et al. 2007, Chevalier et al. 2008) and the boundary conditions are diverse. Vertebral endplates embedded in polymethylmethacrylate (PMMA) (Crawford et al. 2003, Liebschner et al. 2003, Buckley et al. 2007, Christiansen et al. 2011) are a gold standard but the endplates can be removed to create vertebral sections (Ebbesen et al. 1999, Dall'Ara et al. 2011). These two validated models compute compressive ultimate load and provide a better fracture risk prediction than densitometric methods (Crawford et al. 2003, Buckley et al. 2007). However, the absence of endplate or their embedding may lead to distinct structural properties.

The choice of vertebral sections instead of embedded vertebrae save computational resources as segmentation of the endplates is not necessary, PMMA layers need not to be generated and the resulting models have fewer elements.

Accordingly, the aim of this work is to determine if ultimate forces and damage distribution predictions computed from subject-specific, QCT-based voxel finite element models of embedded vertebrae and vertebral sections are equivalent.

2. Materials and methods

2.1 CT scans of the vertebral bodies

Images of vertebrae were obtained from a previous study (Chevalier et al., 2008): 11 cadaveric vertebral bodies were extracted (L1-L5, age 47-83), soft tissues were removed and posterior elements were sectioned at the pedicles. They were scanned individually in a

water-filled container with a HRpQCT system (XtremeCT, 82 μm , 59.4 kV, 1000 mA, Scanco Medical AG, Zurich, Switzerland).

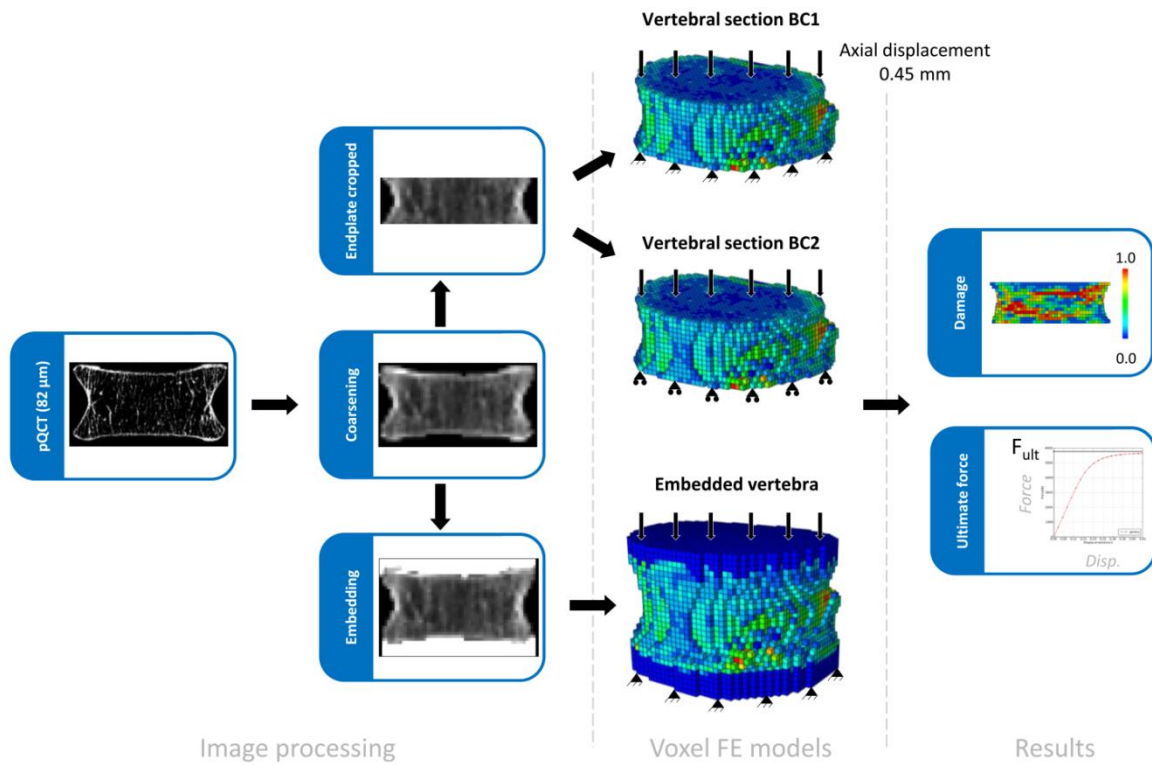


Fig. 1. Overview of the study: first the high resolution peripheral QCT images are coarsened and two sets of images are created either by cropping the endplates or embedding the vertebrae. Then voxel FE models of 11 vertebral bodies are generated from a described technique (Chevalier et al., 2008) and 3 types of boundary conditions are tested in axial compression until ultimate force is reached. Damage distribution and ultimate force computed for each loading case are eventually compared.

2.2 Image processing

Based on a published procedure (Chevalier et al. 2008), we coarsened HRpQCT images (82 μm voxel size) to low resolution (1.3mm voxel size) to simulate *in vivo* resolution and segmented the coarsened images (Fig. 1).

The bone material law was based on bone volume fraction (BV/TV) but the resolution of the original images could induce errors in a direct measurement of BV/TV. Therefore, we calculated BV/TV from BMD of the coarsened voxels by mean of a calibration equation based on experimental ash density and scaled from 0 to 250:

$$\frac{BV}{TV} = \begin{cases} 0, & BMD < -100 \\ \frac{(BMD + 100.5)^2}{1050 * (BMD + 225.849)}, & -100 \leq BMD \leq 1059 \\ 1, & BMD > 1059 \end{cases}$$

Two sets of data were created: embedding in PMMA by adding voxels layers on the endplates (Chevalier et al. 2008, Crawford et al. 2003) or cropping superior and inferior voxel layers of the vertebrae to remove cortical endplates (Dall'Ara et al. 2010).

2.3 Voxel FE models and boundary conditions

Voxels were automatically converted into linear hexahedral elements (approximately 10000 elements per section, 24000 elements per embedded vertebra). We defined PMMA as linear isotropic with $E = 3000$ MPa, $\nu = 0.3$ and chose a nonlinear constitutive law (Garcia et al. 2009) to compute the elastoplastic behaviour of bone from BV/TV. Bone material symmetry was defined as transverse isotropic in the cranio-caudal direction and damage (D) was considered as a scalar ranging from 0 (no damage) to 1 (full damage) accounting for the stiffness reduction of the bone elements due to the formation of microcracks.

We applied three distinct boundary conditions. The nodes of the superior and inferior surfaces of BC3 were fully constrained (Buckley et al. 2007, Chevalier et al. 2009). Similar condition was chosen for the vertebral section BC1 (Dall'Ara et al. 2010). Roller type boundary condition (superior and inferior nodes were transversely free) was used for vertebral section BC2 (Eswaran et al. 2006). We prescribed an axial displacement of 0.45mm to the superior nodes for each BC to reach the ultimate load.

The ultimate forces obtained with the three BCs were compared with linear regressions among the 11 vertebrae, while damage distribution were compared with linear regressions of damage level on a voxel per voxel basis for all voxels common to the three models. Pearson's correlation coefficient (R^2), the concordance correlation coefficient (ccc) and the standard error were calculated for all regressions.

2.4 Simulations

Abaqus (Abaqus 6.9, Simulia, Dassault Systemes, Velizy-Villacoublay, France) was chosen for non-linear analyses. A UMAT subroutine was used for the bone constitutive law described

above. We computed damage distribution, force-displacement curves and used linear interpolation to determine the ultimate forces from each simulation.

3. Results

On a four 3 GHz processors PC with 24GB RAM, the embedded vertebra simulations lasted 7 minutes, the vertebral section ones, 2 minutes.

3.1 Comparison of ultimate forces

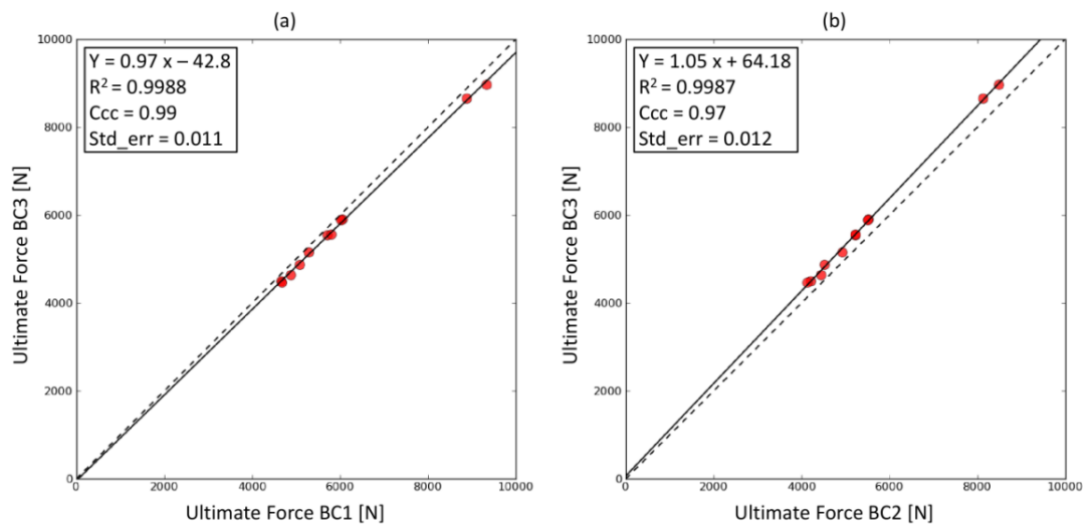


Fig. 2. Correlations between the ultimate force of BC₃ and BC₁ (a) and BC₂ (b) were both excellent.

We compared the computed ultimate forces with *in vitro* results. The ultimate force from our embedded vertebrae simulations (BC3) was 5831 ± 1489 N, while Chevalier et al. 2009 measured 5455 ± 2208 N from their experiments on the same specimens (6% difference). Dallara et al. 2010 measured an *in vitro* ultimate force equal to 5307 ± 1670 N for their vertebral sections. We calculated 6030 ± 1527 N from our vertebral section models (BC1) (12%) with a different set of vertebra.

The average ultimate force obtained with BC3 was 3.5 % lower than the one computed for BC1 and 6.1% higher than the one computed with BC2. Furthermore, excellent correlation was observed between the ultimate forces BC3 and BC1 ($R^2 = 0.999$, $ccc = 0.99$, $std_err = 0.011$) and BC3 and BC2 ($R^2 = 0.999$, $ccc = 0.97$, $std_err = 0.012$) (Fig. 2).

3.2 Comparison of the damage distribution

Histograms of damage for the three BCs are displayed for one vertebra in Fig. 3. Axial, coronal and sagittal views of the damage distribution are shown for another specimen (176L4) in Fig. 4. The map of damage of the embedded vertebra BC3 and the sections BC1 were similar. However, the damage in BC2 was quite different in the superior and inferior layers of elements.

Excellent correlation was obtained between damage in BC1/BC3 and BC2/BC3 ($R^2 = 0.92$, $ccc = 0.956$, $std_err = 0.001$ and $R^2 = 0.73$, $ccc = 0.842$, $std_err = 0.001$ respectively). Better correlations were obtained with superior and inferior elements excluded from the analysis ($R^2 = 0.94$, $ccc = 0.964$, $std_err = 0.001$ for BC3/BC1 and $R^2 = 0.79$, $ccc = 0.881$, $std_err = 0.005$ for BC3/BC2). The correlations for specimen 176L4 are presented in Fig. 5.

4. Discussion

The literature is abundant about tests on embedded vertebrae (Crawford et al. 2003, Liebschner et al. 2003, Buckley et al. 2007, Christiansen et al. 2011) but only few tests on vertebral sections are reported (Ebbesen et al. 1999, Dall'Ara et al. 2011). Concerns were raised about the lack of realism of such models.

Ultimate forces of BC3 and vertebral sections were similar to experimental results of the literature. Ultimate load for BC3 was 6.1% higher than BC2's but 3.5% lower than BC1's with very high correlations (BC1/BC3: $ccc = 0.99$ and BC2/BC3: $ccc = 0.97$). The nodes of the superior and inferior surfaces were fixed (BC1) or transversely free (BC2). Therefore, BC3 is a compromise between BC1 and BC2 since PMMA undergoes small deformations.

Our study shows that the evolution (Fig. 3) and the distribution of damage (Fig. 4) were also close across the BCs. To confirm our observations, we compared the damage computed with the different models element per element for each specimen (Fig. 5 a, c). The best correlation, concordance and the lowest scattering were obtained when comparing embedded vertebra with vertebral section BC1 (BC3/BC1: $ccc = 0.956$ and BC3/BC2: $ccc = 0.842$). A closer look to the damage patterns (Fig. 4) suggested that the damage was different mainly in the superior and inferior elements of the sections.

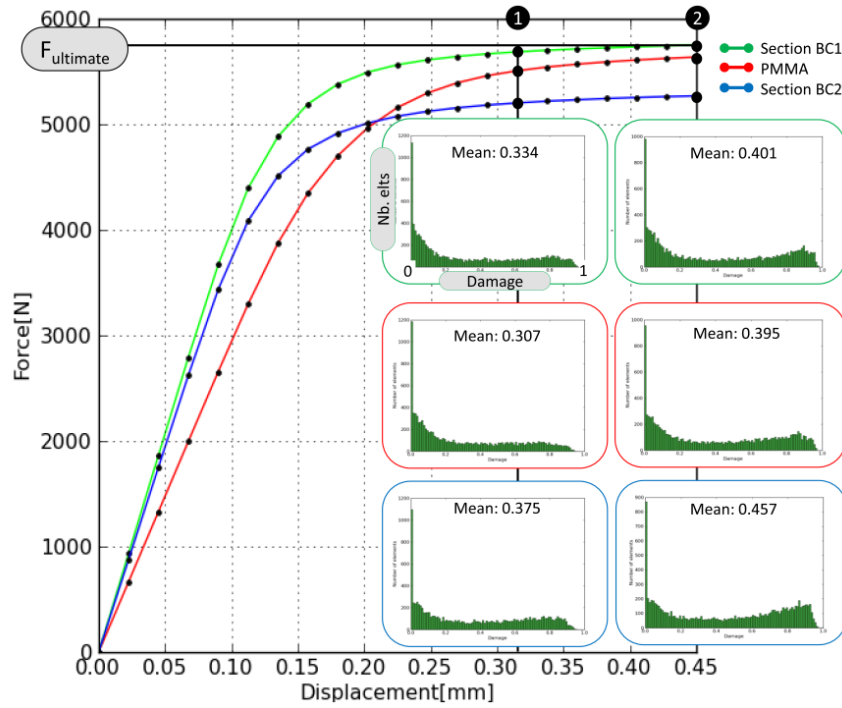


Fig. 3. Example of force-displacement curve computed for the 3 boundary conditions until ultimate force is reached for a vertebral body with the histograms of damage.

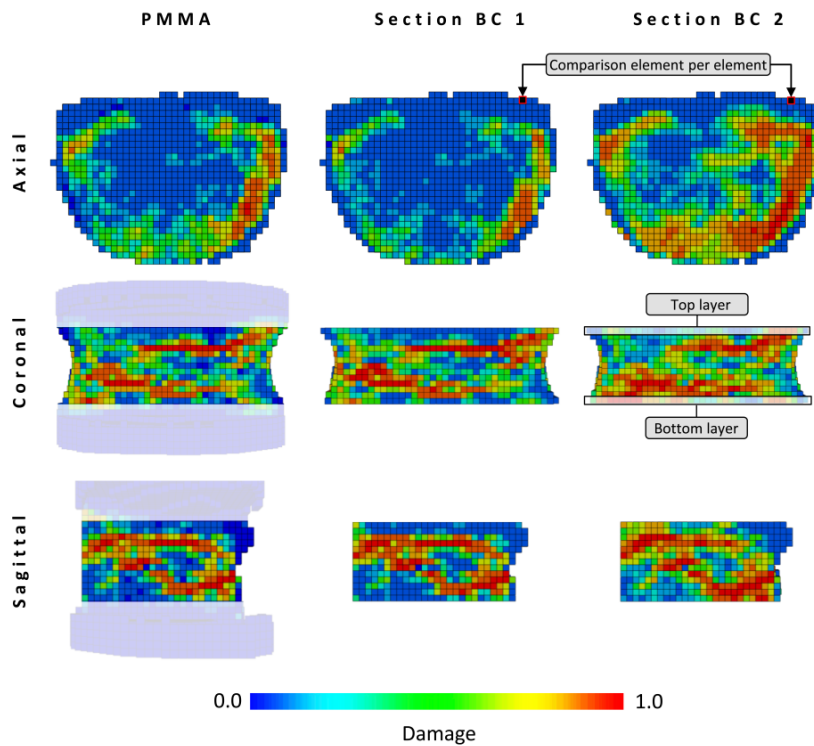


Fig. 4. Damage plots of the simulation of a vertebral body at ultimate force for each of the three boundary conditions. Element per element damage comparisons are performed.

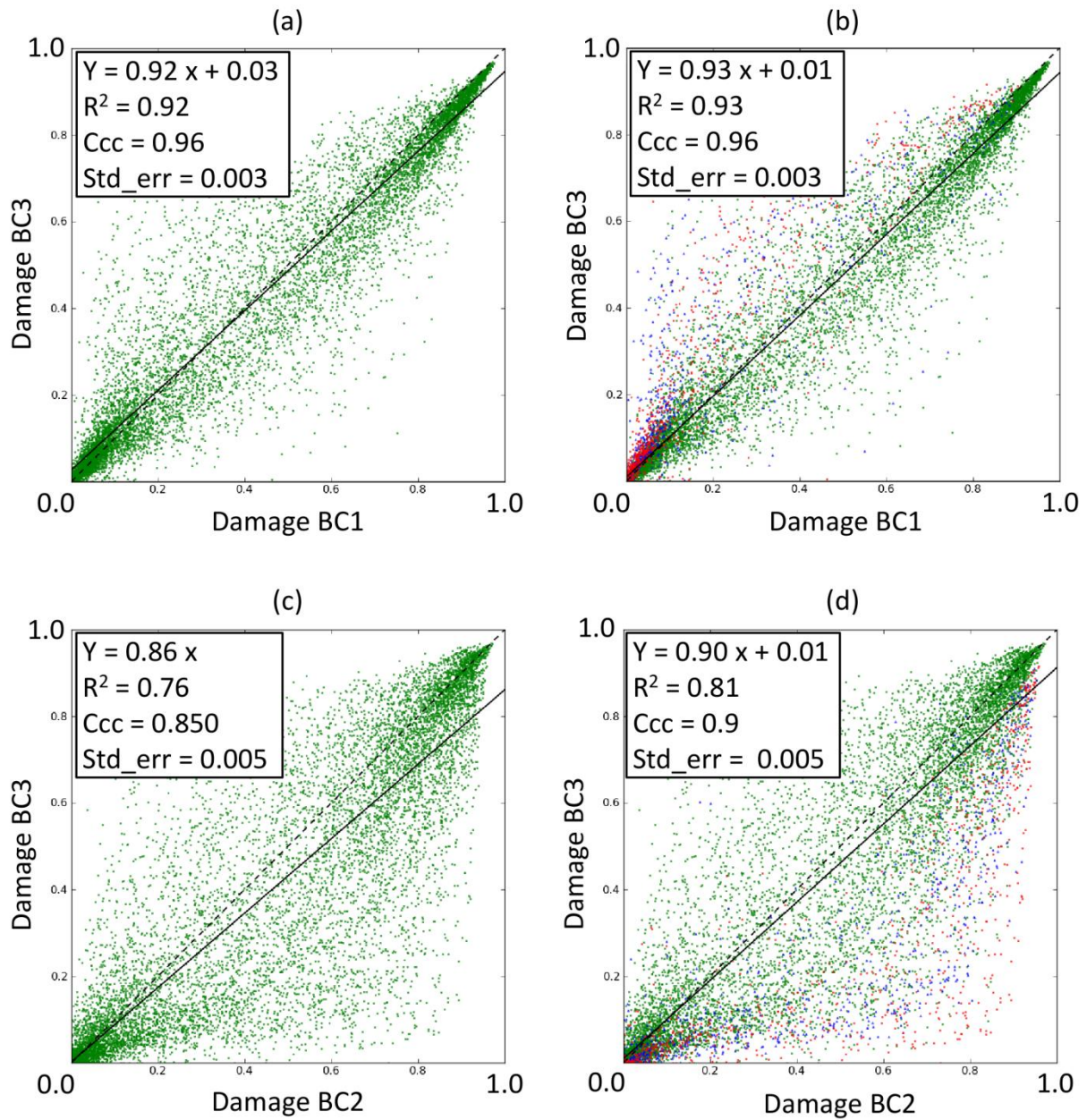


Fig. 5. Example of damage correlations for a typical vertebra (176L4) between voxel models of embedded vertebra (BC_3) and models of the sections BC_1 and BC_2 . Green dots represent the elements taken into account for the correlation, red squares are elements of the bottom layer and blue triangle the elements of the top layer (cf. Fig. 3) (a) and (c) show the correlations between the embedded models and the sections with all elements taken into account while (b) and (d) display the same correlations when the top and bottom layers are excluded from the statistics.

That was confirmed by damage correlations (BC3/BC1: $ccc = 0.964$ and BC3/BC2: $ccc = 0.881$) (Fig. 5 b, d). Damage level of those elements was higher when the boundary condition was looser: BC1 had the lowest damage, BC2 the highest. This suggested that the most influential parameter was the boundary condition of the superior and inferior nodes. For the tested BCs, removal of the endplates had low influence on the ultimate force and overall damage distribution.

Our study presents limitations. First, we used *in vitro* CT scans but due to noise and artefacts caused by the soft tissues around the bone, *in vivo* FE models would be less reliable (Keyak and Falkinstein 2003). Secondly, the cortex thickness is about 500 μm for young individuals and 300 μm in elderly patients (Christiansen et al. 2011), thus coarsening the voxels size to 1.3mm lowers BV/TV of the cortex elements due to partial volume effect. Then, the damage variable of our bone material model was initially set to zero, although osteoporotic vertebrae may exhibit preexisting microdamage (McDonnell et al. 2007).

We did not compare computational and experimental damage distributions quantitatively. However, damage localization computed using the same bone constitutive law was validated qualitatively against experiments for vertebral sections (Dall'Ara et al. 2010). Finally, since axial compression is the standard procedure in experiments, we only tested uniaxial compression although more sophisticated tests were used (lateral bending, flexion-extension, combined load cases) by Chevalier et al. 2008. As done in most cases when using subject-specific QCT-based models, we sectioned the posterior elements. The process removal might affect the damage distribution, but Hulme et al. 2007 and Pollintine et al. 2004 showed that in physiological conditions, only a small portion of the load is carried by the posterior elements under axial compression. Eswaran et al. 2007 and Fields et al. 2010 showed that endplates were at higher risk when loaded via intervertebral discs compared to PMMA. However, healthy intervertebral disks may not lead to more realistic boundary conditions than PMMA for elderly osteoporotic vertebrae.

Despite these limitations, this study demonstrated that voxel finite element models of vertebral sections provide the same ultimate forces and damage distributions in axial compression than models of embedded vertebra for less preprocessing and computing time.

Acknowledgments

The project was made possible through funding obtained from the European Community, Grant Agreement n° PITN-GA-2009-238690-SPINEFX.

References

- Bergot, C., Laval-Jeantet, A. M., Hutchinson, K., Dautraix, I., Caulin, F. and Genant, H. K. 2001, A comparison of spinal quantitative computed tomography with dual energy X-ray absorptiometry in European women with vertebral and nonvertebral fractures. *Calcified tissue international* 68(2): 74-82
- Buckley, J. M., Cheng, L., Loo, K., Slyfield, C. and Xu, Z. 2007, Quantitative computed tomography-based predictions of vertebral strength in anterior bending. *Spine (Phila Pa 1976)* 32(9): 1019-1027
- Chevalier, Y., Charlebois, M., Pahr, D., Varga, P., Heini, P., Schneider, E. and Zysset, P. 2008, A patient-specific finite element methodology to predict damage accumulation in vertebral bodies under axial compression, sagittal flexion and combined loads. *Computer methods in biomechanics and biomedical engineering* 11(5): 477-487
- Chevalier, Y., Pahr, D. and Zysset, P. K. 2009, The role of cortical shell and trabecular fabric in finite element analysis of the human vertebral body. *Journal of biomechanical engineering* 131(11): 111003
- Christiansen, B. A., Kopperdahl, D. L., Kiel, D. P., Keaveny, T. M. and Bouxsein, M. L. 2011, Mechanical contributions of the cortical and trabecular compartments contribute to differences in age-related changes in vertebral body strength in men and women assessed by QCT-based finite element analysis. *Journal of bone and mineral research* 26(5): 974-983
- Crawford, R. P., Cann, C. E. and Keaveny, T. M. 2003, Finite element models predict in vitro vertebral body compressive strength better than quantitative computed tomography. *Bone* 33(4): 744-750
- Cristofolini, L., Schileo, E., Juszczyk, M., Taddei, F., Martelli, S. and Viceconti, M. 2010, Mechanical testing of bones: the positive synergy of finite-element models and in vitro experiments. *Philosophical transactions. Series A, Mathematical, physical, and engineering sciences* 368(1920): 2725-2763
- Dall'Ara, E., Pahr, D., Varga, P., Kainberger, F. and Zysset, P. 2011, QCT-based finite element models predict human vertebral strength in vitro significantly better than simulated DEXA. *Osteoporosis international*
- Dall'Ara, E., Schmidt, R., Pahr, D., Varga, P., Chevalier, Y., Patsch, J., Kainberger, F. and Zysset, P. 2010, A nonlinear finite element model validation study based on a novel experimental technique for inducing anterior wedge-shape fractures in human vertebral bodies in vitro. *Journal of biomechanics* 43(12): 2374-2380
- Ebbesen, E. N., Thomsen, J. S., Beck-Nielsen, H., Nepper-Rasmussen, H. J. and Mosekilde, L. 1999, Lumbar vertebral body compressive strength evaluated by dual-energy X-ray absorptiometry, quantitative computed tomography, and ashing. *Bone* 25(6): 713-724
- Engelke, K., Adams, J. E., Ambrecht, G., Augat, P., Bogado, C. E., Bouxsein, M. L., Felsenberg, D., Ito, M., Prevrhal, S., Hans, D. B. and Lewiecki, E. M. 2008, Clinical use of

- quantitative computed tomography and peripheral quantitative computed tomography in the management of osteoporosis in adults: the 2007 ISCD Official Positions. *Journal of clinical densitometry* 11(1): 123-162
- Eswaran, S. K., Gupta, A., Adams, M. F. and Keaveny, T. M. 2006, Cortical and trabecular load sharing in the human vertebral body. *Journal of bone and mineral research* 21(2): 307-314
- Eswaran, S. K., Gupta, A. and Keaveny, T. M. 2007, Locations of bone tissue at high risk of initial failure during compressive loading of the human vertebral body. *Bone* 41(4): 733-739
- Fields, A. J., Lee, G. L. and Keaveny, T. M. 2010, Mechanisms of initial endplate failure in the human vertebral body. *Journal of biomechanics* 43(16): 3126-3131
- Garcia, D., Zysset, P. K., Charlebois, M. and Curnier, A. 2009, A three-dimensional elastic plastic damage constitutive law for bone tissue. *Biomechanics and modeling in mechanobiology* 8(2): 149-165
- Griffith, J. F. and Genant, H. K. 2008, Bone mass and architecture determination: state of the art. *Best practice & research. Clinical endocrinology & metabolism* 22(5): 737-764
- Hulme P.A, Boyd S.K., Ferguson S.J 2007, Regional variation in vertebral bone morphology and its contribution to vertebral fracture strength. *Bone* 41: 946–957
- Kanis, J. A., Johnell, O., Oden, A., Johansson, H., Eisman, J. A., Fujiwara, S., Kroger, H., Honkanen, R., Melton, L. J., O'Neill, T., Reeve, J., Silman, A. and Tenenhouse, A. 2006, The use of multiple sites for the diagnosis of osteoporosis. *Osteoporosis international* 17(4): 527-534
- Keyak, J. H. and Falkinstein, Y. 2003, Comparison of in situ and in vitro CT scan-based finite element model predictions of proximal femoral fracture load. *Medical engineering & physics* 25(9): 781-787
- Liebschner, M. A., Kopperdahl, D. L., Rosenberg, W. S. and Keaveny, T. M. 2003, Finite element modeling of the human thoracolumbar spine. *Spine (Phila Pa 1976)* 28(6): 559-565
- Lin L, 1989, A Concordance Correlation Coefficient to Evaluate Reproducibility. *Biometrics*, 45 (1): 255-268
- McDonnell, P., McHugh, P. E. and O'Mahoney, D. 2007, Vertebral osteoporosis and trabecular bone quality. *Annals of biomedical engineering* 35(2): 170-189
- Pahr, D. H., Dall'Ara, E., Varga, P. and Zysset, P. K. 2011, HR-pQCT-based homogenised finite element models provide quantitative predictions of experimental vertebral body stiffness and strength with the same accuracy as μ FE models. *Computer methods in biomechanics and biomedical engineering*. 2011 Apr 1:1 [Epub]
- Pollintine, P., Przybyla, A.S, Dolan, P., Adams, M.A. 2004, Neural arch load-bearing in old and degenerated spines. *Journal of Biomechanics* 37: 197–204
- Ruffoni D. and van Lenthe G.H. 2011, Finite Element Analysis in Bone Research: A Computational Method Relating Structure to Mechanical Function. *Comprehensive Biomaterials*, 3: 91-111
- Silva, M. J. 2007, Biomechanics of osteoporotic fractures. *Injury* 38 Suppl 3: S69-S76
- Varga, P., Baumbach, S., Pahr, D. and Zysset, P. K. 2009, Validation of an anatomy specific finite element model of Colles' fracture. *Journal of biomechanics* 42(11): 1726-1731

Chapter 3: The influence of intervertebral disc degeneration on vertebral strength

From the manuscript

Embedding of human vertebral bodies leads to higher ultimate load and altered damage localisation under axial compression

G. Maquer, J.J. Schwiedrzik and P.K. Zysset

Institute of Surgical Technology and Biomechanics, University of Bern, Bern, Switzerland

Published in: Computer Methods in Biomechanics and Biomedical Engineering (2012) 1-12

DOI: <http://10.1080/10255842.2012.744400>

Abstract

Computer tomography (CT-) based finite element (FE) models of vertebral bodies assess fracture load *in vitro* better than DXA, but boundary conditions affect stress distribution under the endplates that may influence ultimate load and damage localization under post-yield strains. Therefore, HRpQCT-based homogenized FE models of 12 vertebral bodies were subjected to axial compression with two distinct boundary conditions: embedding in polymethylmethacrylate (PMMA) and bonding to a healthy intervertebral disc (IVD) with distinct hyperelastic properties for nucleus and annulus. Bone volume fraction and fabric assessed from HRpQCT data were used to determine the elastic, plastic and damage behaviour of bone. Ultimate forces obtained with PMMA were 22% higher than with IVD but correlated highly ($R^2=0.99$). At ultimate force, distinct fractions of damage were computed in the endplates (PMMA: 6%, IVD: 70%), cortex and trabecular sub-regions, which confirms previous observations that in contrast to PMMA embedding, failure initiated underneath the nuclei in healthy IVDs. In conclusion, axial loading of vertebral bodies via PMMA embedding versus healthy IVD overestimates ultimate load and leads to distinct damage localization and failure pattern.

Keywords: Boundary Conditions, Finite Element Analysis, Osteoporosis, Vertebral Strength, Intervertebral Disc

1. Introduction

With 490 000 cases a year in Europe, compression fractures of osteoporotic vertebrae are among the most common type of osteoporotic fractures with high morbidity and health care costs (Johnell and Kanis 2005). Dual energy X-ray absorptiometry (DXA), the usual technique for diagnosis and follow up of osteoporosis in the vertebra, does not account for morphology and local variation of bone density and thus, is not a satisfactory surrogate of bone strength (Griffith and Genant 2008, McDonnell et al. 2007, Dall'Ara et al. 2012). Yet, more advanced methods such as QCT, HRQCT and CT-based finite element (FE) models are now used in clinical trials to estimate vertebral bone strength for various load cases (Keaveny et al. 2007, Graeff et al. 2009).

Several studies suggest that vertebral strength is more sensitive to the boundary condition on the endplates than to bone quality (Buckley et al. 2006, Jones and Wilcox 2007). Therefore, due to the uncertainties introduced by various degrees of disc degeneration in elderly spines, validation of the FE models were performed with endplates embedded in PMMA (Crawford et al. 2003, Chevalier et al. 2009) or without endplates (Dall'ara et al. 2010). These boundary conditions, recently found to be equivalent (Maquer et al. 2012), may be appropriate for mimicking a highly degenerated IVD that applies a more uniform load on the endplates compared to a healthy IVD (Keller et al. 1993).

However, a higher proportion of wedge fractures is observed clinically for vertebral bodies adjacent to degenerated IVD, while patients with healthy IVD rather undergo biconcave fractures (Seymour et al. 1998, Lee 2000, Ortiz et al. 2011). Thus, the absence of endplates or their embedding would probably generate boundary conditions that are different from a healthy IVD and may lead to distinct structural properties.

In fact, several authors simulated intervertebral discs as boundary condition for their μ FE models of vertebral bodies but only stress or strain distributions were computed and linear elastic models of the IVD were used (Homminga et al. 2004, Eswaran et al. 2006, Eswaran et al. 2007, Fields et al. 2010). The recent introduction of hyper-elastic and anisotropic models of intervertebral disc would guarantee a more realistic boundary condition but such models were only used to investigate disc degeneration (Galbusera et al. 2011) and its effects on

the range of motion and stiffness of the spine (Rohlmann et al. 2006) or on the disc stress profile (Dolan et al. 2001).

Thus, while damage and strength of embedded vertebral bodies have been computed in some FE studies, the literature is poor in case of specimens surrounded by intervertebral discs. Furthermore, although boundary conditions are a critical aspect of biomechanical testing, its impact on the failure behaviour of the vertebral body remains unclear as no comparison between PMMA embedding and intervertebral discs was undertaken.

Accordingly, the aim of this work was to determine whether strength and damage localisation predictions computed from homogenized finite elements models of human vertebral bodies were influenced by the choice of boundary condition. To this end, two sets of models based on 12 samples were produced before axial compression was applied: either embedding in PMMA was simulated as often done in biomechanical studies *in vitro* or the specimens were surrounded by healthy intervertebral discs.

2. Materials and Methods

An overview of the automatic homogenized finite element (hFE) model generation is given in Fig. 1 and Fig. 2.

2.1 CT scans of the vertebral bodies

HRpQCT data of 12 vertebral bodies taken from another study (Chevalier et al. 2008) were used to generate the FE models (Fig. 1). The authors extracted the vertebrae (L1-L5, age 47-83, all male), removed the soft tissues, sectioned the posterior elements at the pedicles and scanned the vertebral bodies in a water-filled container (XtremeCT, 82 μm , 59.4 kV, 1000 mA, Scanco Medical AG, Zürich, Switzerland).

2.2 Image processing

The image processing and meshing were performed automatically with in-house software on the HRpQCT data following a published method (Pahr and Zysset 2008). A Laplace–Hamming filter was first used to remove noise (Laib et al. 1998), the images were then scaled to a range of 1–250 and segmented between cortical and trabecular masks using a ‘fill’ algorithm described by Pahr and Zysset (2008) (Fig. 1).

2.3 Mesh generation

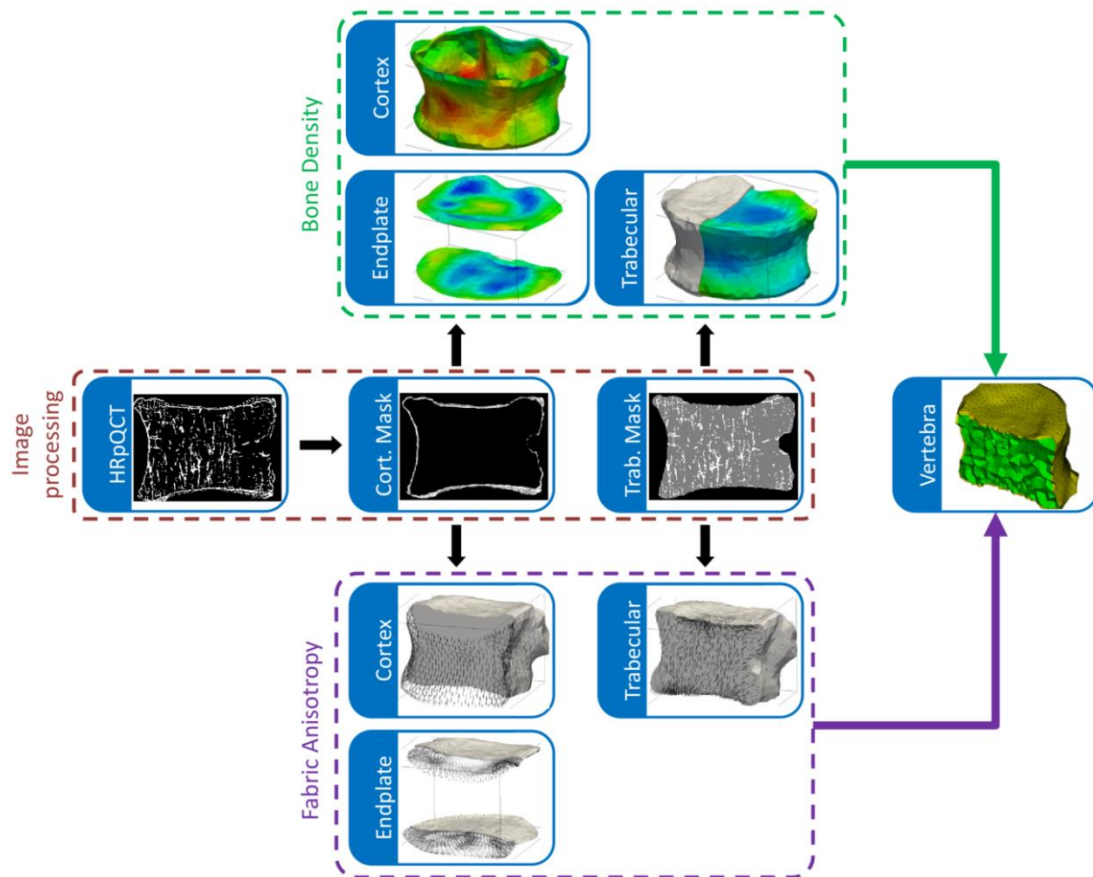


Fig. 1. Generation of the *fE* models of the vertebral body. The HRpQCT data were segmented, cortical and cancellous bone separated and three element sets (endplates, cortical and trabecular bone) generated using a published method (Pahr and Zysset 2008). Bone density and fabric were assessed from the CT images (Pahr and Zysset 2009).

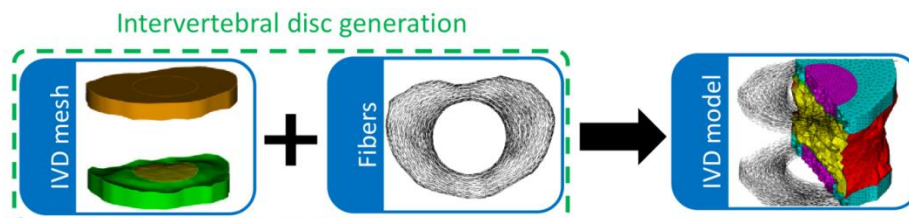


Fig. 2. Generation of the IVDs meshes. Two volumes were extruded from the meshes of the cranial and caudal cortical endplates of the vertebral body model previously generated. Each volume was separated into two domains to distinguish between nucleus pulposus and annulus fibrosus and then meshed. The fibres were oriented circumferentially around the nucleus by changing the local orientation of each annulus element.

Isosurf (Treece et al. 1999) was used to create a triangle mesh on the surface of the trabecular mask. This was only a surface mesh without cortex representation yet. Therefore, to produce volume meshes for trabecular and cortical bone, the algorithm described in Pahr and Zysset 2008 was used. This algorithm generates quadratic wedge elements for the cortex by extruding the positions of the nodes of the triangle mesh until the thickness of the wedge elements and the local thickness of the cortical mask matches. The trabecular bone was meshed by generating quadratic tetrahedral elements within the volume determined by the triangle mesh. Endplate elements were selected from the cortex elementset based on the angle between the normal of the triangular surface and the anatomical cranio-caudal direction. Compared to the published procedure, an extra step became necessary. The meshes were imported in Cubit (Cubit mesh generation environment, Version 12.2, CUBIT Development Team, Sandia National Laboratory, Albuquerque) and the endplate elements were remeshed in order to account for the morphology of the nucleus pulposus. The geometry of the half discs (Roaf, 1960) was extruded from the mesh to create two independent volume domains (Fig. 2: nucleus pulposus and annulus fibrosus). The meshing of the IVD using tetrahedral elements was therefore easier and contact between bone and IVD during the simulations was no longer necessary thanks to the perfect bonding between the meshes. The dimensions of the intervertebral disc are usually taken from measurements (Schroeder et al. 2006, Shirazi-Adl et al. 2010), MRI (Périé et al. 2001, Schmidt et al. 2006) or QCT data (Ayturk et al. 2010, Moramarco et al. 2010, Homminga et al. 2011) assuming the volume of the nucleus and its positioning within the disc (Jones and Wilcox 2008). Thus, a height of 5 mm was used for the two half-intervertebral discs (Amonoo-Kuofi 1991, Inoue et al. 1999) and a volumetric ratio of 42% between nucleus pulposus and annulus fibrosus chosen (Goto et al. 2002, Moramarco et al. 2010). The cranial and caudal mid-surfaces of the discs were chosen flat (Jones and Wilcox 2008).

2.4 Material properties

2.4.1 Bone constitutive model

The elastic and strength properties of each bone element were assigned based on morphology information obtained from the HRpQCT images following the methodology of Pahr and Zysset 2009. This method provides a bone volume fraction map and fabric tensors

describing the morphology of the bone. A background grid with a spacing of 3.0 mm was superimposed on the image data. Bone volume fraction and local morphological properties were computed inside a spherical sub-region with a diameter of 7.5 mm diameter centred at each point of the grid. The bone volume fraction in each sub-region was derived from the image data using a calibration curve relating bone volume fraction to apparent bone mineral density (Chevalier et al. 2008). The fabric tensor was calculated using the mean intercept length method (MIL) (Laib et al. 1998) after segmentation of the scan images at a constant threshold (masks). The information was then linearly interpolated between the grid points in order to assign the properties to the elements of the FE mesh.

To model the mechanical behaviour of vertebral bone, a recently proposed visco-plastic damage model by Schwiedrzik and Zysset (2012) was adapted. The rheological model is a damageable elastic spring in series with a plastic pad, which is in parallel with a dashpot element. In the elastic regime, the model shows no strain rate dependence. The plastic strains are accumulating viscously. Damage accumulation is assumed coupled to the plasticity using a damage function reducing all elements of the stiffness tensor. D is limited between 0 (no damage) and 1 (complete failure) accounting for the stiffness reduction of the bone elements due to the formation of micro-cracks. The orthotropic elasticity tensor was assigned to each element based on the morphological information obtained from the images and fabric relationships proposed by Zysset and Curnier (1995) and identified by Rincon and Zysset (2009). The elastic domain is bound by an orthotropic fabric and density based Tsai-Wu criterion that was fitted to the uni and multiaxial strength data of Rincon and Zysset (2009). The viscosity of the plastic accumulation was essentially switched off and the hardening/softening function was identified with experimental force-displacement curves of vertebral sections (Dall'Ara et al. 2010).

2.4.2 Intervertebral disc constitutive model

While linear elastic isotropic models of the disc are available for μ FE studies (Homminga et al 2004, Eswaran et al. 2006, Fields et al. 2010), two methods are commonly used to model the anisotropy of the annulus in hFE models: explicit representation of the collagen fibres by bar elements embedded in a matrix (Goto et al. 2002, Rohlmann et al. 2006, Dreischarf et al. 2011) or homogenized hyperelastic constitutive law of the matrix and fibres. This option, developed by Holzapfel and Gasser (2000) to model arteries, was adapted to the annulus

fibrosus (Eberlein et al. 2001, Eberlein et al. 2004). Porous models were also developed (Swider et al. 2010, Malandrino et al. 2010, Galbusera et al. 2011) but anisotropic models may be sufficient to represent the instantaneous response of the intervertebral disc (Jones and Wilcox 2008). Therefore, the following free energy functions were derived for the IVD:

$$\begin{aligned}\psi_{\text{nucleus}} &= C_{10}(J_1 - 3) + \frac{1}{\Delta}(J - 1)^2 \\ \psi_{\text{annulus}} &= C_{10}(J_1 - 3) + C_{20}(J_1 - 3)^2 + \frac{1}{\Delta}(J - 1)^2 + \psi_{\text{fibres}_4} \\ &+ \psi_{\text{fibres}_6}\end{aligned}$$

$$\psi_{\text{fibres}_i} = \frac{K_1}{2K_2} \{ \exp[K_2(J_i - 1)^2] - 1 \}$$

The modified invariants were defined as:

$$J_4 = \mathbf{a}_0 \mathbf{C}^* \mathbf{a}_0 \quad J_6 = \mathbf{b}_0 \mathbf{C}^* \mathbf{b}_0$$

with $\mathbf{a}_0 = [\cos(\phi), \sin(\phi), 0]^t$ and $\mathbf{b}_0 = [\cos(\phi), -\sin(\phi), 0]^t$ being unitary vectors giving fibres direction and \mathbf{C}^* is the modified right Green strain tensor:

$$\mathbf{C}^* = \frac{1}{4} \mathbf{F}^{*t} \mathbf{F}^* \quad \text{and} \quad \mathbf{F}^* = J^{-1/3} \mathbf{F}$$

\mathbf{F} is the deformation gradient and $J = \det(\mathbf{F})$. This constitutive model was chosen by several authors (Perez del Palomar et al. 2008, Moramarco et al. 2010) and validated against the literature (Brown et al. 1957, Markolf and Morris 1974, Panjabi et al. 1994, Guan et al. 2007). The value of the coefficients C_{10} , C_{20} (matrix material), Δ (compressibility modulus), K_1 and K_2 (fibres stiffness) were taken from Moramarco et al. 2010.

An angle $\phi = \pm 30^\circ$ was chosen relative to a transverse plane and both fibre families were acting only in tension ($J_i < 1$, $\psi_{\text{fibres}_i} = 0$, Peyrault et al. 2009). The fibres were placed circumferentially: thanks to a python script, the local orientation of each annulus elements was defined according to the geometry of the annulus contours. A smooth distribution was achieved by means of a linear interpolation between the orientation at the inner contour around the nucleus and outer contour of the annulus fibrosus (Fig. 2). PMMA was defined as

linear isotropic with $E = 3000 \text{ MPa}$, $\nu = 0.3$ and prescribed to the nucleus and annulus elementsets without modifying the meshes for the PMMA boundary condition.

2.5 Simulations

The constitutive laws have been implemented as FORTRAN subroutine (UMAT) and non-linear analyses were performed with Abaqus (Abaqus6.9, Simulia, DassaultSystemes, Velizy-Villacoublay, France). The nodes of the caudal surface of the inferior discs were fixed axially and a displacement (PMMA: 3 mm, IVD: 6 mm) was applied on the nodes of the cranial surface of the superior discs at slow constant displacement rate of 5 mm/min (Chevalier et al. 2008). The nodes of both surfaces were free transversely. We computed force-displacement curves, determined the ultimate forces (Ult_{PMMA} and Ult_{IVD}) and damage distribution of the vertebral bodies.

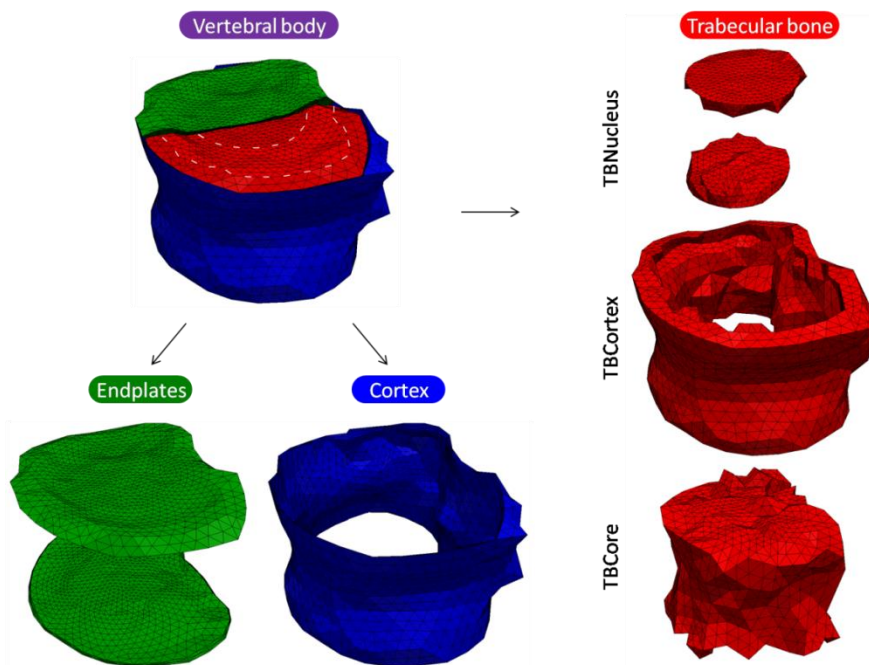


Fig. 3. Regions of interest of the vertebral bodies: 1, subdiscal trabecular elements located underneath the nuclei, 2, trabecular elements adjacent to cortical wall, 3, elements of the cancellous core, 4, cortical endplates, 5, cortical shell and 6, full vertebral body.

To understand the mechanisms of damage accumulation in bone, the fraction volume damaged (FVD) and weighted mean damage (WMD) were calculated in six element sets: the complete vertebral body, its endplates, cortex and the trabecular bone composed of three

sub-regions: the elements of the trabecular core located underneath the nucleus pulposus (the same elements were picked in case of PMMA boundary condition), the elements besides the cortical wall and the elements of the core (Fig. 3).

$$FVD = \frac{\sum V_i^D}{\sum V_i} * 100 \qquad WMD = \frac{\sum (V_i^D * D_i)}{\sum V_i}$$

V_i being the volume of the i^{th} element of the element set, D_i the damage level of the i^{th} element and V_i^D , the volume of the i^{th} element of the element set if $D_i > 0$. Therefore, $\sum V_i^D$ is the volume of the element set that is damaged. Moreover, WMD describes the extent of damage accumulation within an element set.

2.6 Statistics

Pearson's correlation coefficient (R^2), regression equation, concordance correlation coefficient (ccc, Lin 1989) and standard error was computed for the correlation of ultimate forces between the two loading conditions. Paired two-tailed Student's t-tests were performed for comparisons of volume damaged and weighted mean damaged. Significance level was set to 95% ($p < 0.05$).

3. Results

The meshes counted 12000 elements in average. PMMA and IVD simulations lasted 5h and 13h on a four 3 GHz processors PC with 24GB RAM.

3.1 Comparison of force-displacement curves

3.1.1 Verification of the force-displacement curves

Ultimate force was defined as the maximum force reached before softening (Fig. 4) and we computed ultimate forces with PMMA ($Ult_{PMMA} = 3610 \pm 1419$ N) and IVD ($Ult_{IVD} = 2841 \pm 1064$ N). Using the same protocol with PMMA, Chevalier et al. (2008) measured experimentally an ultimate force equal to 5339 ± 2138 N and the correlation obtained between our ultimate forces and their experimental measurements is excellent ($R^2 = 0.898$). By compressing *in vitro* lumbar vertebrae surrounded by intervertebral discs, Jiang et al. (2010) measured a failure load of 2900 N.

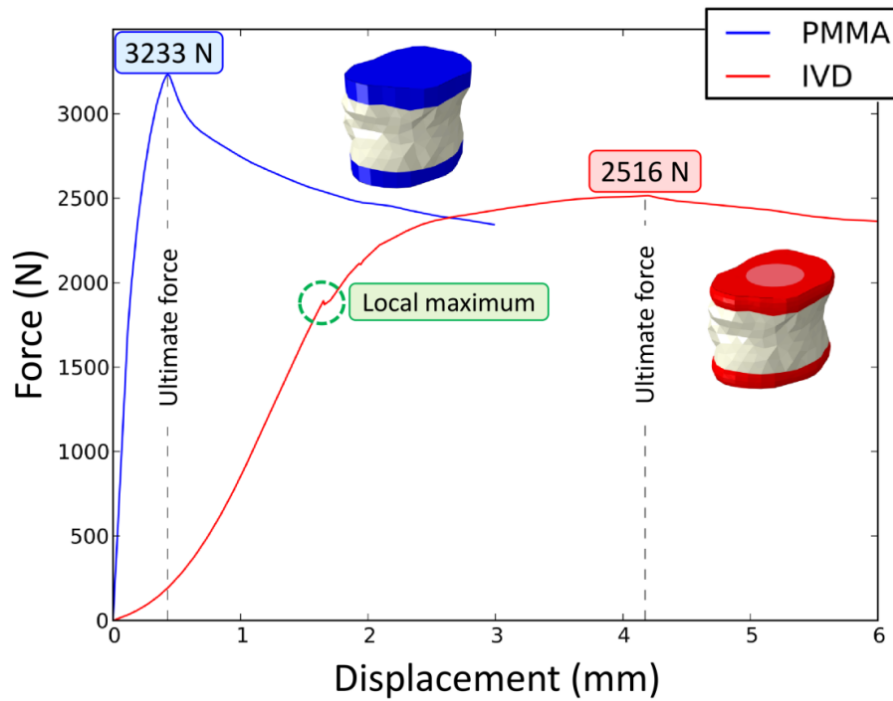


Fig. 4. Force-deflection curve computed for the two boundary conditions. Ultimate forces reported as the maximal force obtained before softening occurs were significantly different.

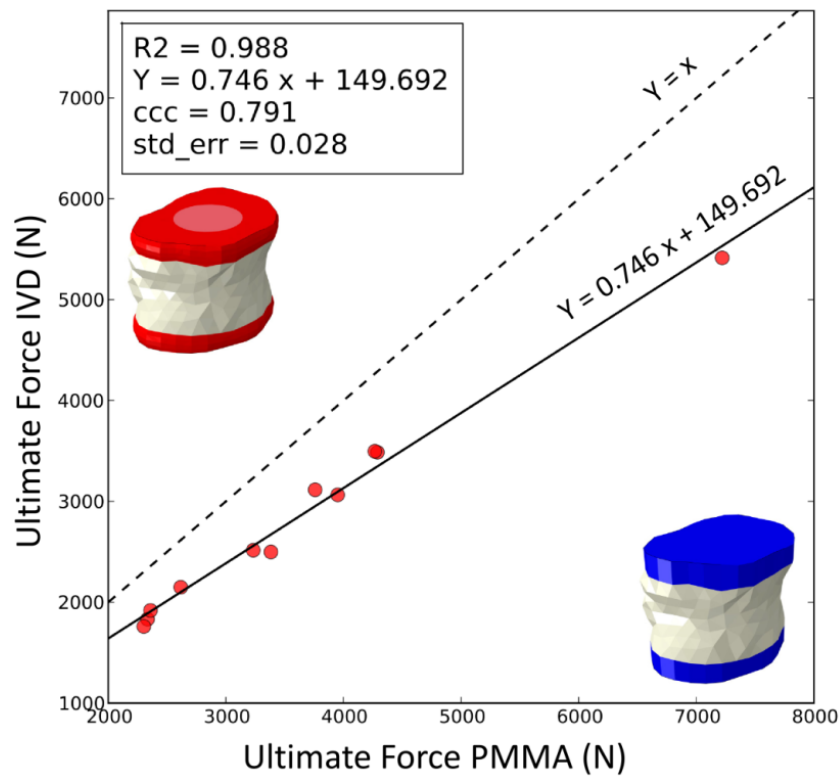


Fig. 5. Although the ultimate forces computed IVD and PMMA boundary conditions were significantly different, their correlation was high.

3.1.2 Pre-yield local force maxima

One or several local maxima were seen on force-deflection curves of every IVD simulation before the ultimate force was reached (Fig. 4). These peaks were observed in previous *in vitro* tests (Roaf 1960, Henzel et al. 1968, Shirado et al. 1992).

3.1.3 The effect of boundary condition on the yield behaviour

The average Ult_{PMMA} was 22 % higher than Ult_{IVD} . However, excellent correlation was found between Ult_{PMMA} and Ult_{IVD} ($R^2 = 0.988$, $ccc = 0.79$, $std_err = 0.028$) (Fig. 5). Moreover, in both cases, softening was observed after reaching the ultimate force. However, the decrease in force due to softening was always higher with PMMA than with IVD. The embedded vertebral bodies were also more brittle than the ones with discs and yield occurred earlier. The deformation of the compliant intervertebral discs explains partly these observations but not entirely: embedded specimens appeared also to dissipate more energy than specimens surrounded by discs.

3.2 Comparison of damage localisation

3.2.1 Evolution of damage

The evolution of FVD and WMD during the compression of a vertebral body (Fig. 6) shows a faster increase of the volume damaged in trabecular and cortical bone with PMMA. Moreover, the endplates were more subject to damage when not constrained by the embedding material: the volume of damaged elements and their damage was rising higher and faster.

3.2.2 Damage localization with IVD at the pre-yield local force maxima

One or several local force maxima were observed on the force-deflection curves of the IVD boundary condition. Damage maps of a few increments before (Fig. 7 a) and after that peak (Fig. 7 b) show that this small but sudden decrease of force seemed to be related to damage initiation in the cancellous bone below the nucleus.

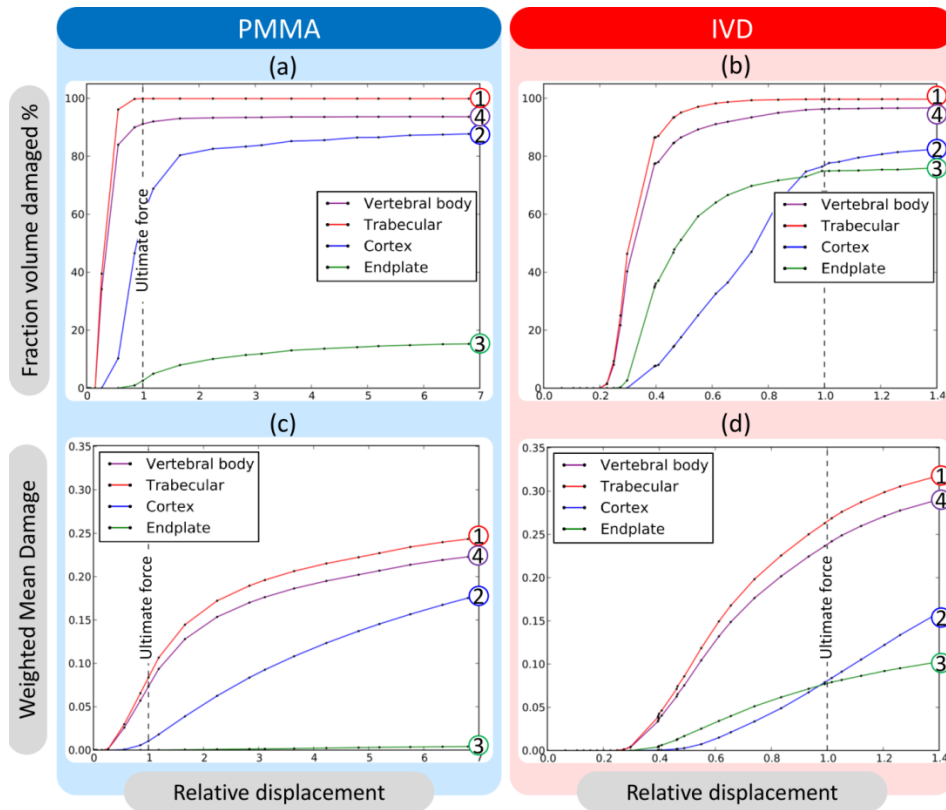


Fig. 6. Evolution of the FVD (a and b) and of the WMD (c and d) in the element sets of a vertebral body plotted against the relative displacement. The relative displacement is 1 at the ultimate force. 1, trabecular bone, 2, cortical shell, 3, endplates and 4, vertebral body.

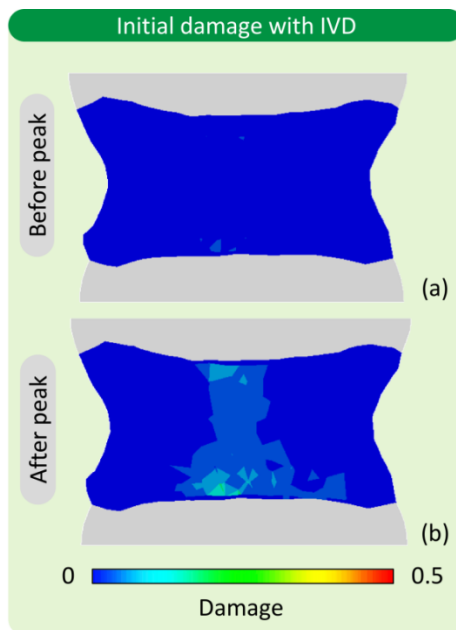


Fig. 7. Damage plots (a) before and (b) after the local maximum observed on Fig. 4 for a vertebral body.

3.2.3 Qualitative observations from damage plots

Coronal views of the damage localisation for a typical specimen (176L4) display the map of damage of the embedded vertebra PMMA and the IVD boundary conditions. They were different, especially in the endplates region. Indeed, at ultimate force (Fig. 8 a, c), the highest levels of damage are seen in the trabecular bone underneath the nuclei, while the embedding seemed to “protect” this area of the bone even for displacements superior to the ultimate displacements (Fig. 8 b, d).

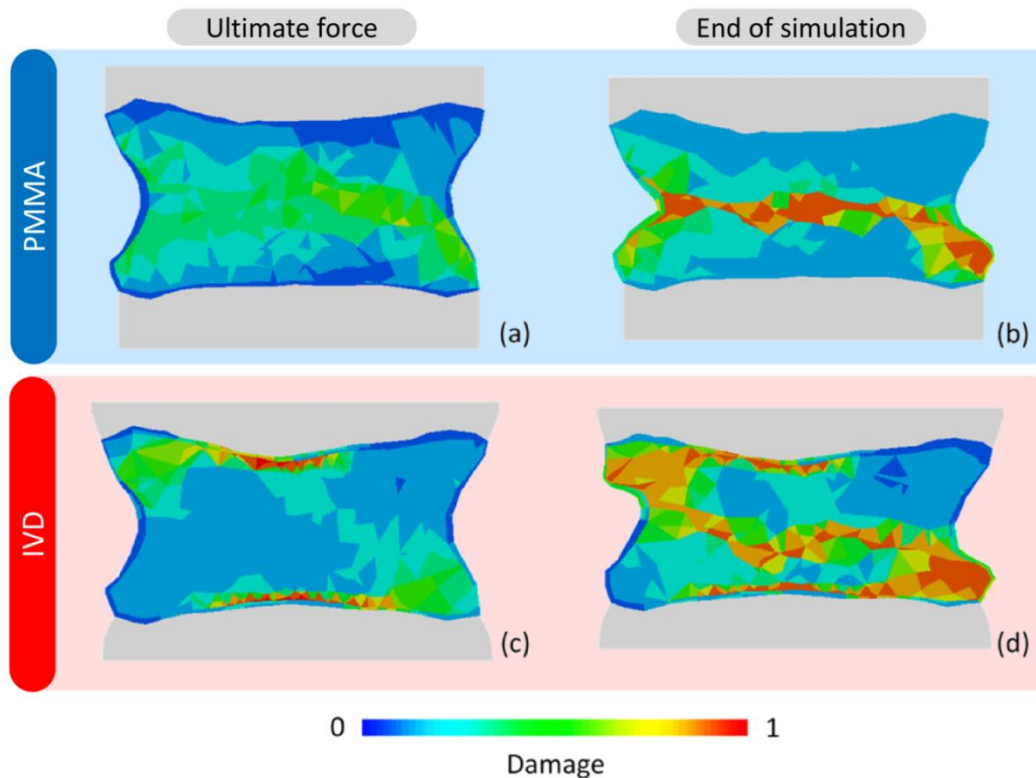


Fig. 8. Damage plots during compression of a typical vertebral body (176L4). Damage localisations at ultimate force (a and c) and at the end of the simulation (b and d) are displayed in the coronal mid-plane for each boundary condition.

3.2.4 Quantitative evaluation of damage

The FVD and WMD were compared between both types of boundary conditions (Fig. 9). The volume of cancellous bone damaged was similar for both boundary conditions but the localisation of damage within the trabecular bone itself was studied specifically (Fig. 9 a). The fraction of volume damaged in the trabecular core was higher with PMMA (TBCore:

$FVD_{PMMA} = 66\% - FVD_{IVD} = 59\%$, $p = 0.1$) but this difference was not significant. The cortical region of the trabecular bone was more likely to damage with PMMA (TBCortex: $FVD_{PMMA} = 17\% - FVD_{IVD} = 7\%$, $p=0.008$) while the trabecular region under the nuclei was more sensible with IVD (TBNucleus: $FVD_{PMMA} = 7\% / FVD_{IVD} = 19\%$, $p<0.001$). Those results were coherent with the FVD of the cortex ($FVD_{PMMA} = 65\% / FVD_{IVD} = 58\%$, $p = 0.02$) and endplates ($FVD_{PMMA} = 18\% / FVD_{IVD} = 77\%$, $p < 0.001$).

However, a quick glance at WMD (Fig. 9b) suggests that damage accumulated significantly more in all elementsets ($p_{TBNucleus}$, $p_{TBCortex}$ and $p_{endplate} < 0.001$, $p_{TBCore}=0.02$) but the cortex when the IVD boundary condition was used. We observed qualitatively that every region of the trabecular bone and the cortical endplates seemed protected when loaded via PMMA. This is also shown by a significantly higher damage level in the complete vertebral body ($WMD_{PMMA} = 0.12 - WMD_{IVD} = 0.17$, $p=0.02$).

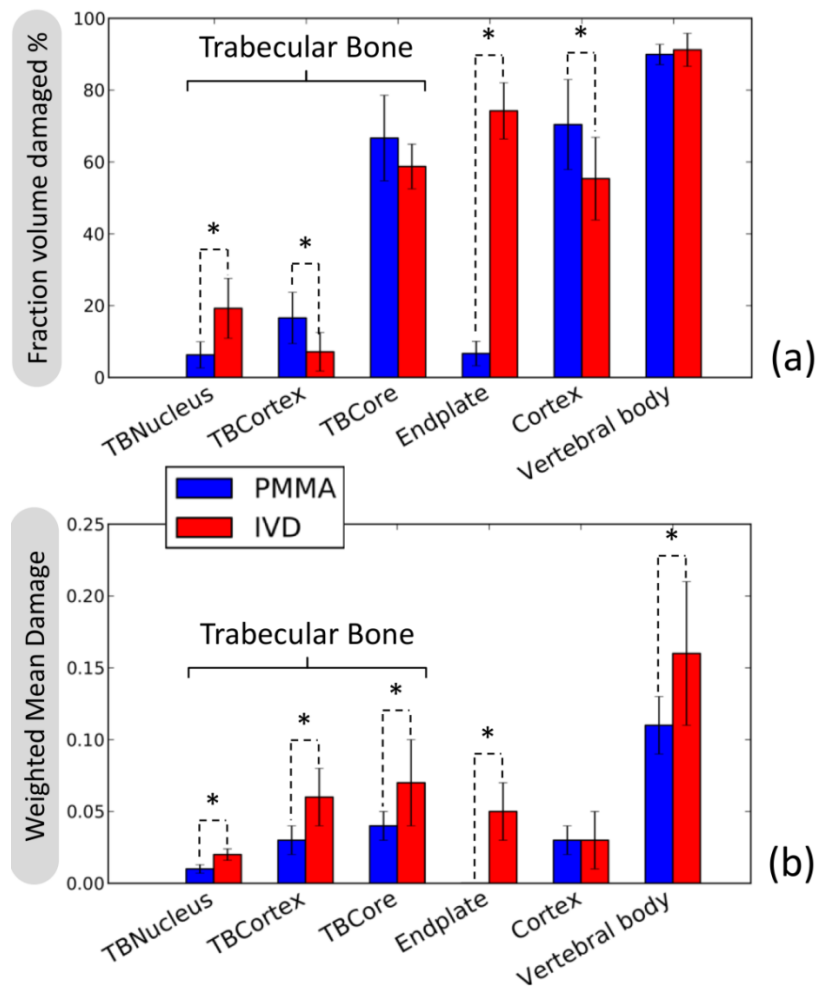


Fig. 9. Effect of the boundary conditions on FVD and WMD per region of interest at ultimate

force. *TBNucleus* (subdiscal trabecular elements located underneath the nuclei), *TBCortex* (trabecular elements adjacent to cortical wall), *TBCore* (elements of the cancellous core), endplates, cortex and vertebral body. Significant differences are marked with *.

4. Discussion

Several authors studied the effects of boundary conditions during loading (Homminga et al. 2004, Eswaran et al. 2006, Fields et al. 2010, Homminga et al. 2011) using computationally expensive linear elastic μ FE models. They did not attempt to compute the ultimate force, keystone of fracture risk prediction from FE (Crawford et al. 2003, Buckley et al. 2007, Chevalier et al. 2008), nor did they quantify damage in the bone. In this study, we use the state-of-the-art intervertebral disc and bone models to measure the effect of fully degenerated (PMMA) and healthy (IVD) boundary conditions on ultimate force and damage localisation.

A closer look to the force-deflection curves reveals that our simulations are able to capture fine details: local force maxima are seen on every computed force-deflection curves before yield. Interestingly, Roaf (1960), Henzel et al. (1968) and Shirado et al. (1992) observed peaks before failure of the vertebral body, referring to them as endplates disruptions which is coherent with the sudden increase in damage observed after the peaks in the endplates and trabecular region under the nuclei in *in vitro* (Jiang et al. 2010), *in vivo* (Ortiz et al. 2011) and *in silico* (Fields et al. 2010) studies. Moreover, this injury is occurring with healthy intervertebral disc as our models of discs.

Ult_{PMMA} is higher than Ult_{IVD} . The force-deflection curves highlight the effects of the boundary condition on ultimate force: the stiffness of the embedding material compared to the relative softness of the healthy intervertebral disc affects the way the endplates distribute stress in the vertebral body and the overall ductility of the vertebral bodies (Nekkanty et al. 2010). Indeed, *in vitro* (Shirado et al. 1992 and Dai 1998) and FE (Homminga et al. 2001, Polikeit et al. 2004) studies reports less risk of fracture for an osteoporotic vertebral body when surrounded by degenerated discs: the trabecular bone acting as an energy absorber carries a higher fraction of the load than the cortical shell when the vertebra is surrounded by healthy discs, while this fraction is lower in case of a stiff degenerated disc (Kurowski and Kubo 1986, Homminga et al. 2001, Adams et al. 2006,

Homminga et al. 2011). The underestimation of our FE predictions compared to experimental data is explained by the non-viscous nature of our constitutive law for bone. Although, switching on the viscosity term of the bone material would improve the FE prediction of the ultimate forces measured by Chevalier et al. (2008), this switch would affect equally the FE simulations with PMMA and IVD boundary conditions.

The ability of our models to compute damage localisation provides further insight to our understanding of damage mechanisms. We found that the PMMA embedding keeps the endplates intact whereas damage is easily initiated via intervertebral discs under the nucleus. The stiff embedding material provides rigid boundary conditions that prevent any deformations in the endplates as Fields et al. 2010 showed by suppressing the Poisson effect of the discs. Additional measures show that the endplates and the trabecular bone underneath the nuclei are the weakest regions in osteoporotic vertebral bodies and undergo the highest deformation when loaded with healthy intervertebral discs (Kurowski and Kubo 1986, Eswaran et al. 2007, Fields et al. 2010).

The relative difference Ult_{PMMA} / Ult_{IVD} is always about 20% and good correlation exists between Ult_{PMMA} and Ult_{IVD} ($R^2 = 0.988$). This suggests that FE models with embedding material are actually as good as FE models with intervertebral discs to compute vertebral strength of the vertebral bodies knowing the shift between the two predictions ($Ult_{IVD} = Ult_{PMMA} * 0.746 + 149.692$). Therefore, an explicit modelling of the intervertebral disc does not seem necessary for transversal and longitudinal comparisons of vertebral strength as suggested by Buckley et al. (2006). This high correlation between Ult_{PMMA} and Ult_{IVD} might seem surprising. The stiffness of the specimen decreases while its overall level of damage increases. However, only a damage localisation band through the entire vertebral body can explain why a specimen reaches ultimate force. This band corresponds approximately to the elements with the lowest BTV and is independent of the boundary condition, which may explain the high correlation. Therefore, although the growth of damage is depending on the boundary condition, with high areas of damage occurring initially under the endplates with IVD, the damage localisation band at ultimate load presents similarities and the difference between Ult_{PMMA} and Ult_{IVD} becomes almost independent of the specimen tested. The higher damage level under the nuclei explains the non-visibility of “central band of damage” from Fig. 8 c while visible on Fig. 8 a, b, d).

The first limitation to highlight concern the material tested. The number of specimens used is limited (12). However, considering the wide range of age (47-83 y.o.), level (L1-L5), BMD (0.29-1.22 g.cm⁻²) and shape, excellent correlation of ultimate forces and similar damage localisation were computed from our specimens. A second limitation pertains to the damage that does not take in account a pre-existing micro-damage. Finally, we only tested rigid uniaxial compression although sophisticated loading cases were tested (lateral bending, flexion-extension, combined load cases) by Chevalier et al. (2008). However, Chevalier and Zysset (2012) showed that all major stiffnesses correlated well with the axial stiffness. In addition, no experimental tests were performed to validate our spine unit models with the ideal intervertebral discs. Nevertheless, both models of bone and discs had been already validated independently in previous studies (Pahr et al. 2011, Moramarco et al. 2010) and the ultimate forces computed were in agreement with the available literature. Finally, while embedding of the vertebral endplates is commonly used as a biomechanical testing protocol, our study demonstrated that ultimate force and damage distribution of vertebral bodies were affected significantly by the presence of a soft intervertebral disc using hFE models running 100 times faster than corresponding μ FE models even on a standard PC.

Acknowledgements

This study was made possible thanks to funding obtained from the European Community, Grant Agreement n° PITN-GA-2009-238690-SPINEFX. The authors would like to thank Yan Chevalier for the HRpQCT data and Dieter Pahr for the support with the in-house software.

References

- Adams MA, Pollintine P, Tobias JH, Wakley GK, and Dolan P. 2006. Intervertebral Disc Degeneration Can Predispose to Anterior Vertebral Fractures in the Thoracolumbar Spine. *J Bone Miner Res.* 21(9).
- Amonoo-Kuofi HS. 1991. Morphometric changes in the heights and anteroposterior diameters of the lumbar intervertebral discs with age. *J Anat.* 175:159-168.
- Ayturk UM, Garcia JJ and Puttlitz CM. 2010. The micromechanical role of the annulus fibrosus components under physiological loading of the lumbar spine. *J Biomech Eng.* 132.
- Brown T, Hansen RJ, Yorra AJ. 1957. Some mechanical tests on the lumbosacral spine with particular reference to intervertebral disc. *J BoneJoint Surg.* 39:1135–1164.

- Buckley JM, Leang DC, Keaveny TM. 2006. Sensitivity of vertebral compressive strength to endplate loading distribution. *J Biomech Eng.* 128(5):641–646.
- Buckley JM, Cheng L, Loo K, Slyfield C, and Xu Z. 2007. Quantitative computed tomography-based predictions of vertebral strength in anterior bending. *Spine.* 329:1019–1027.
- Chevalier Y, Charlebois M, Pahr D, Varga P, Heini P, Schneider E, and Zysset P. 2008. A patient-specific finite element methodology to predict damage accumulation in vertebral bodies under axial compression, sagittal flexion and combined loads. *Comput Methods Biomech Biomed Eng.* 11:477–487.
- Chevalier Y and Zysset P. 2012. A patient-specific CT-based finite element methodology to calculate the 6D stiffness matrix of vertebral bodies. *Comput Methods Biomech Biomed Eng.* 12:77–79.
- Crawford RP, Cann CE, and Keaveny TM. 2003. Finite element models predict in vitro vertebral body compressive strength better than quantitative computed tomography. *Bone.* 334:744–750.
- Crawford RP, Rosenberg WS, and Keaveny TM. 2003. Quantitative computed tomography-based finite element models of the human lumbar vertebral body: effect of element size on stiffness, damage, and fracture strength predictions. *J Biomech Eng.* 1254:434–438.
- Dai L. 1998. The relationship between vertebral body deformity and disc degeneration in lumbar spine of the senile. *Eur Spine J.* 7:40–44.
- Dall’Ara E, Schmidt R, Pahr D, Varga P, Chevalier Y, Patsch J, Kainberger F, Zysset P. 2010. A nonlinear finite element model validation study based on a novel experimental technique for inducing anterior wedge-shape fractures in human vertebral bodies in vitro. *J Biomech.* 43:2374–2380
- Dall’Ara E, Pahr D, Varga P, Kainberger F and Zysset P. 2012. QCT-based finite element models predict human vertebral strength in vitro significantly better than simulated DEXA. *Osteoporos Int.* 23(2):563–72.
- Dolan P and Adams MA. 2001. Recent advances in lumbar spinal mechanics and their significance for modelling. *Clinical Biomechanics.* 16:S8–S16.
- Dreischarf M, Rohlmann A, Bergmann G, Zander T. 2011. Optimised loads for the simulation of axial rotation in the lumbar spine. *J Biomech.* 44:2323–2327.
- Eberlein R, Holzapfel HA and Schulze-Bauer CAJ. 2001. An anisotropic model for annulus tissue and enhanced finite element analyses of intact lumbar disc bodies. *Comput Methods Biomech Biomed Eng.* 4:209–229.
- Eberlein R, Holzapfel G A, Frohlich M. 2004. Multi-segment FEA of the human lumbar spine including the heterogeneity of the annulus fibrosus. *Computational Mechanics.* 34:147–163.
- Eswaran SK, Gupta A, Adams MF, and Keaveny TM. 2006. Cortical and trabecular load sharing in the human vertebral body. *J Bone Miner Res.* 212:307–314.
- Eswaran SK, Gupta A and Keaveny TM 2007. Locations of bone tissue at high risk of initial failure during compressive loading of the human vertebral body. *Bone.* 41(4):733–739.
- Fields AJ, Lee G L and Keaveny TM. 2010. Mechanisms of initial endplate failure in the human vertebral body. *J Biomech.* 43(16):3126–3131.
- Galbusera F, Schmidt H, Neidlinger-Wilke C, Gottschalk A, Wilke HJ. 2011. The mechanical response of the lumbar spine to different combinations of disc degenerative changes

- investigated using randomized poroelastic finite element models. *Eur Spine J.* 20:563–571.
- Goto K, Tajima N, Chosa E, Totoribe K, Kuroki H, Arizumi Y and Arai T. 2002. Mechanical analysis of the lumbar vertebrae in a three-dimensional finite element method model in which intradiscal pressure in the nucleus pulposus was used to establish the model. *J OrthopSci.* 7:243–246.
- Graeff C, Chevalier Y, Charlebois M, Varga P, Pahr D, Nickelsen TN, Morlock MM, Glüer CC and Zysset PK. 2009. Improvements in vertebral body strength under teriparatide treatment assessed in vivo by finite element analysis: results from the EUROFORS study. *J Bone Miner Res.* 24(10):1672-80.
- Griffith JF, Genant HK. 2008. Bone mass and architecture determination: state of the art. *Best Pract Res ClinEndocrinolMetab.* 22:737–764.
- Guan Y, Yoganandan N, Moore J, Pintar FA, Zhang J, Maiman DJ, Laud P. 2007. Moment-rotation responses of the lumbosacral spinal column. *J Biomech.* 40:1975–1980.
- Hansson T, Roos B. 1981. The relation between bone mineral content, experimental compression fractures, and disc degeneration in lumbar vertebrae. *Spine.* 6(2):147-53.
- Henzel JH, Mohr GC and von Gierke HE. 1968. Reappraisal of biodynamic implications of human ejections. *Aerosp Med.* 39(3):231-40.
- Holzappel GA and Gasser TC. 2000. A new constitutive framework for arterial wall mechanics and a comparative study of material models. *J Elast.* 61: 1–48.
- Homminga J, Weinans H, Gowin W, Felsenberg D, Huiskes R. 2001. Osteoporosis changes the amount of vertebral trabecular bone at risk of fracture but not the vertebral load distribution. *Spine.* 26(14):1555-1561.
- Homminga J, and Van-Rietbergen B, Lochmüller E M, Weinans H, Eckstein F and Huiskes R. 2004. The osteoporotic vertebral structure is well adapted to the loads of daily life, but not to infrequent error loads. *Bone.* 34:510–516.
- Homminga J, Aquarius R, Bultink VE, Jansen CTJ, Verdonschot N. 2011. Can vertebral density changes be explained by intervertebral disc degeneration? *Med Eng Phys.* 101016/jmedengphy201108003.
- Inoue H, Ohmori K, Miyasaka K, Hosoe H. 1999. Radiographic evaluation of the lumbosacral disc height. *Skeletal Radiol.* 8:638–643.
- Jiang G, Luo J, Pollintine P, Dolan P, Adams MA, Eastell R. 2010. Vertebral fractures in the elderly may not always be osteoporotic. *Bone.* 47:111–116.
- Johnell O, Kanis J. 2005. Epidemiology of osteoporotic fractures. *Osteoporos Int.* 16(Suppl 2):S3–S7.
- Jones AC, and Wilcox RK. 2007. Assessment of factors influencing finite element vertebral model predictions. *J Biomech Eng.* 129:898–903.
- Jones AC and Wilcox RK. 2008. Finite element analysis of the spine: towards a framework of verification, validation and sensitivity analysis. *Med Eng Phys.* 30:1287–1304.
- Keaveny TM, Donley DW, Hoffmann PF, Mitlak BH, Glass EV and Martin JAS. 2007. Effects of teriparatide and alendronate on vertebral strength as assessed by finite element modelling of qct scans in women with osteoporosis. *J Bone Miner Res.* 22:149–157.
- Keller TS, Ziv I, Moeljanto E, Spengler DM. 1993. Interdependence of lumbar disc and subdiscal bone properties: a report of the normal and degenerated spine. *J Spinal Disord.* 6:106–113.

- Kurowski P, Kubo A. 1986. The relationship of degeneration of the intervertebral disc to mechanical loading conditions on lumbar vertebrae. *Spine*. 11:726-731.
- Laib A, Huelmann HJ, Regsegger P. 1998. In vivo high-resolution 3D-QCT of the human forearm. *Technol Health Care*. 6(5-6):329-337.
- Lee Kyu Sung. 2000. The Effect of Disc Degeneration in Osteoporotic Vertebral Fracture. *J Korean Soc Spine Surg*. 7(4):558-564
- Lin L-K, 1989. A concordance correlation coefficient to evaluate reproducibility. *Biometrics*. 45:255-268.
- Malandrino A, Planell JA, Lacroix D. 2009. Statistical factorial analysis on the poroelastic material properties sensitivity of the lumbar intervertebral disc under compression. Flexion and axial rotation. *J Biomech*. 42:2780-2788.
- Maquer G, Dall'Ara E, Zysset PK. 2012. Removal of the cortical endplates has little effect on ultimate load and damage distribution in QCT-based voxel models of human lumbar vertebrae under axial compression. *J Biomech*. 45:1733-1738.
- McDonnell P, McHugh PE, O'Mahoney D. 2007. Vertebral osteoporosis and trabecular bone quality. *Ann Biomed Eng*. 35:170-189.
- Markolf KL, Morris JM. 1974. The structural components of the vertebral disc: a study of their contribution to the ability of the disc to withstand compressive force. *J Bone Joint Surg*. 56:675-687.
- Moramarco V, Perez del Palomar A, Pappalettere C, Doblare M. 2010. An accurate validation of a computational model of a human lumbosacral segment. *J Biomech*. 43:334-342.
- Nekkanty S, Yerramshetty J, Kim D, Zuel R, Johnson E, Cody DD, Yeni YN. 2010. Stiffness of the endplate boundary layer and endplate surface topography are associated with brittleness of human whole vertebral bodies. *Bone*. 47:783-789.
- Ortiz AO and Bordia R. 2011. Injury to the vertebral endplate-disk complex associated with osteoporotic vertebral compression fractures. *Am J Neuroradiol*. 32:115-20.
- Pahr DH and Zysset PK. 2008. From high-resolution CT data to finite element models: development of an integrated modular framework. *Comput Methods Biomech Biomed Eng*. 12:45-57.
- Pahr DH, and Zysset PK. 2009. A comparison of enhanced continuum fe with micro fe models of human vertebral bodies. *J Biomech*. 424:455-462.
- Pahr DH, Dall'Ara E, Varga P and Zysset PK. 2011. HR-pQCT-based homogenised finite element models provide quantitative predictions of experimental vertebral body stiffness and strength with the same accuracy as μ FE models. *Comput Methods Biomech Biomed Eng*. DOI: 10.1080/10255842.2011.556627.
- Panjabi MM, Oxland TR, Yamamoto I, Crisco JJ. 1994. Mechanical behavior of the human lumbar and lumbosacral spine as shown by three-dimensional load-displacement curves. *J Bone Joint Surg*. 76:413-424
- Périer D, Sales De Gauzy J, Curnier D, Hobathoc MC. 2001. Intervertebral disc modelling using a MRI method: Migration of the nucleus zone within scoliotic intervertebral discs. *Magn Reson Imaging*. 19:1245-1248.
- Perez del Palomar A, Calvo B, Doblare M. 2008. An accurate finite element model of the cervical spine under quasi-static loading. *J Biomech*. 41:523-531.
- Peyrault F, Renaud C, Labed N, Feng Z. 2009. Modélisation de tissus biologiques en hyperélasticité anisotrope – Étude théorique et approche éléments finis. *C R Mécanique*. 337:101-106.

- Polikeit A, Nolte L, Ferguson S. 2004. Simulated influence of osteoporosis and disc degeneration on the load transfer in a lumbar functional spinal unit. *J Biomech.* 37:1061-1069.
- Rincon-Kohli L and Zysset P. 2009. Multi-axial mechanical properties of human trabecular bone. *J Biomech Model Mechanobiol.* 8(3):195–208.
- Roaf R. 1960. A study of the mechanism of spinal injuries. *J Bone Joint Surg.* 42B:810-823.
- Rohlmann A, Zander T, Schmidt H, Wilke HJ, Bergmann G. 2006. Analysis of the influence of disc degeneration on the mechanical behaviour of a lumbar motion segment using the finite element method. *J Biomech.* 39:2484-2490.
- Schwiedrzik JJ, Zysset PK. 2012. An anisotropic elastic viscoplastic damage model for bone tissue. *Biomech Model Mechanobiol.* DOI 101007/s10237-012-0392-9.
- Schroeder Y, Wilson W, Huyghe JM, Baaijens FPT. 2006. Osmoviscoelastic finite element model of the intervertebral disc. *Eur Spine J.* 15(3):S361–71.
- Schmidt H, Heuer F, Simon U, Kettler A, Rohlmann A, Claes L. 2006. Application of a new calibration method for a three-dimensional finite element model of a human lumbar annulus fibrosus. *ClinBiomech.* 21(4):337–44.
- Seymour R, Williams LA, Rees JI, Lyons K and Lloyd DCF. 1998. Magnetic Resonance Imaging of Acute Intraosseous Disc Herniation. *Clin Radiol.* 53:363-368.
- Shirado O, Kaneda K, Tadano S, Ishikawa H, McAfee PC and Warden KE. 1992. Influence of disc Degeneration on Mechanisms of Thoracolumbar Burst Fractures. *Spine.* 17(3):286-92.
- Shirazi-Adl A, Taheri M, Urban JPG. 2010. Analysis of cell viability in intervertebral disc: Effect of endplate permeability on cell population. *J Biomech.* 43:1330-1336.
- Swider P, Pedrono A, Ambard D, Accadbled F, Sales de Gauzy J. 2010. Substructuring and poroelastic modelling of the intervertebral disc. *J Biomech.* 43:1287-1291.
- Treece GM, Prager RW, Gee AH. 1999. Regularised marching tetrahedra: improved iso-surface extraction. *ComputGraph.* 23(4):583-598.
- Zysset PK and Curnier A. 1995. An alternative model for anisotropic elasticity based on fabric tensors. *Mech Mater.* 21(4):243-250.

Chapter 4: Normalisation of intervertebral disc compliances

From the manuscript

Normalisation of human intervertebral disc compliances to account for size

G. Maquer ^a, M. Laurent ^a, V. Brandejsky ^b, M.L. Pretterklieber ^c and P.K. Zysset ^a

^a Institute of Surgical Technology and Biomechanics, University of Bern, Switzerland

^b Department of Clinical Research, Inselspital, University of Bern, Switzerland

^c Centre of Anatomy and Cell Biology, Department of Applied Anatomy, Medical University of Vienna, Austria

Submitted to: Journal of Biomechanics (March, 20th 2013)

Abstract

Disc degeneration, associated with low back pain and loss of intervertebral stiffness, represents a major health issue with high costs. As the intervertebral disc (IVD) morphology influences the stiffness measurements, the link between mechanical properties and degenerative grade is partially lost without normalisation with respect to geometry. Indeed, no stiffness normalisation has been defined systematically for 4 usual biomechanical tests (compression, torsion, lateral-bending, flexion/extension). Therefore, a parameter study involving simulations of those tests on 20 Finite Elements IVD models with identical non-linear hyperelastic material but various dimensions was carried out. Initial (initial slope), final (major slope) and total (load/displacement) apparent stiffnesses (K_i , K_f , K_t) computed from the simulated load-deflection data were normalised by height (H) and cross-sectional area (CSA), polar moment of inertia (J) or moments of inertia (I_{xx} , I_{yy}). This normalisation routine was applied to the experimental stiffnesses of 14 human lumbar IVDs for each of the 4 quasi-static biomechanical tests, H , CSA , J , I_{xx} and I_{yy} were computed from T1-weighted MRI to minimize shape approximations. The study confirmed that normalisation strongly attenuated the higher stiffness observed with wider IVDs, especially for the K_i . It also improved the correlations between K_i , K_f and K_t for each load case. No relations between the compressive normalised stiffness and other stiffnesses were found while torsion, bending and flexion/extension normalised stiffnesses were significantly correlated. The results show that the geometrical effect can be attenuated. The MRI-based normalisation proposed for all 4 biomechanical tests, requisite for inter-individual and inter-level comparisons of intervertebral stiffness, is necessary to relate the mechanical properties of an IVD to its degree of degeneration.

Keywords: Human intervertebral disc, Stiffness normalisation, Compression, Torsion, Bending.

1. Introduction

Half of the western population suffers from low back pain at least once in life, which represents a major health issue with billions spent in health care costs (Panjabi 2003). In a majority of patients, the pathogenesis of lower back pain cannot be determined with any degree of certainty. It is usually attributed to muscular or ligamentous strain, facet joint arthritis, or pressure exerted by the intervertebral disk on the annulus fibrosus, the vertebral end plates or nerve roots (Wise 2011).

The intervertebral stiffness loss resulting in greater spinal motions (spinal instability) is related to a clinical instability (pain or neurological deficit) (Panjabi 2003, Leone et al. 2007). Several structures affect the spinal stability: facets joints covered by articular cartilage, ligaments, muscles, intervertebral disc (IVD) (Kirkaldy-Willis et al. 1982, Stokes et al. 1987). Biomechanical testing on cadaver intervertebral segments highlighted the contribution of the intervertebral disc (IVD) with a change in load distribution (Dolan and Adams 2001), neutral zone (Panjabi 2003), range of motion (Tanaka et al., 2001) and stiffness (Haughton et al. 1999) after alterations due to the degenerative process (Nachemson et al. 1979). Indeed, the IVD stiffness decreases at early degeneration stages but increases at the latest grade during spondylophytes formation (Kirkaldy-Willis et al. 1982, Krismer et al. 2000).

Several experimental studies showed that the disc seems to become stiffer in compression, torsion, lateral bending, flexion/extension as its height decreases or CSA increases (Adams et al. 1990, Natarajan et al. 1999). As Finite Element (FE) provide further insight into our understanding of IVD's mechanics (Moramarco et al. 2010, Quasim et al. 2012). An FE parameter study confirmed the significant impact of its geometry on its stiffness regardless of its degeneration by varying height and cross-sectional area (CSA) of an IVD model with identical material properties, something impossible experimentally (Natarajan et al. 1999). Hence, any attempts to compare the stiffness of two specimens are biased by the inter-individual variability due to height and area changing with age (Koeller et al. 1986, Amonookuofi et al. 1991), spinal level (Koeller et al. 1984) or gender (Nachemson et al. 1979). Furthermore, as the morphology could prevail upon material properties, the correlation of the stiffness with the degenerative grade is hardly possible without a proper normalisation with respect to geometry. Performing level-wise studies reduces the inter-

specimen variability (Tanaka et al. 2001) but since it is sometimes challenging to obtain enough human material, direct comparisons are usually done (Schmidt et al. 1998, Bisschop et al. 2013).

Normalisation of bone (Mosekilde et al. 1987), muscle (Ryan et al. 2011) or tendon apparent stiffness (Fouré et al. 2012) using cross-sectional area is common. Surprisingly, similar approach was employed on the intervertebral disc only in few original contributions pertaining to inter-species comparisons of stiffness normalised by geometry (Elliott and Sarver 2004, Beckstein et al. 2008, Showalter et al. 2012). The authors divided the compressive or torsional stiffness of each IVD by its CSA or polar moment of inertia (J) and multiplied the results by the sample's height. The authors assumed an elliptical disc cross-section for the CSA/ J calculations but this analytical method has never been applied to lateral bending and flexion/extension measurements.

Such assumptions on the IVD's shape can be avoided using MRI (Magnetic Resonance Imaging) extensively used in clinics. Unlike CT (computed tomography), it provides high-resolution images accurately rendering the disc morphology (Belavy et al. 2012).

Considering the high impact of the geometry on the intervertebral mechanics and the lack of gold standard for stiffness normalisation, the aim of this work is to propose a new protocol for the normalisation of the stiffness of IVDs loaded in compression, torsion, lateral bending and flexion/extension using accurate MRI-based morphological data. This protocol, tested on 20 FE models with various dimensions, was applied on the stiffness of 14 human lumbar intervertebral discs.

2. Materials and methods

2.1 Method of normalisation

Assimilating the IVD to a short beam with minimal shear, its apparent moduli (K^N in MPa) can be computed by normalising its apparent stiffnesses (K) in compression (N/mm), torsion, lateral bending and flexion extension (Nmm/°) by height (H , mm), area (CSA, mm^2), polar moment of inertia (J , mm^4) or area moment of inertia (I_{xx} , I_{yy} , mm^4) of its cross-section, as commonly done in linear elasticity. I_{xx} , computed along the lateral diameter (x), is associated with lateral bending, I_{yy} , calculated along the anteroposterior diameter (y), is related to the flexion/extension stiffnesses.

$$K_{\text{comp}}^N = \frac{K_{\text{comp}} * H}{\text{CSA}}$$

$$K_{\text{torsion}}^N = \frac{K_{\text{torsion}} * H}{J}$$

$$K_{\text{latbending}}^N = \frac{K_{\text{latbending}} * H}{I_{xx}}$$

$$K_{\text{flex/ext}}^N = \frac{K_{\text{flex/ext}} * H}{I_{yy}}$$

2.2 Parameter study

A parameter study was conducted on 4 sets of 5 FE models of IVD using Abaqus (Abaqus 6.10, Simulia, Dassault-Systemes, France). Those 20 models had identical material properties but differed in height (z), lateral (x) and anteroposterior (y) diameters.

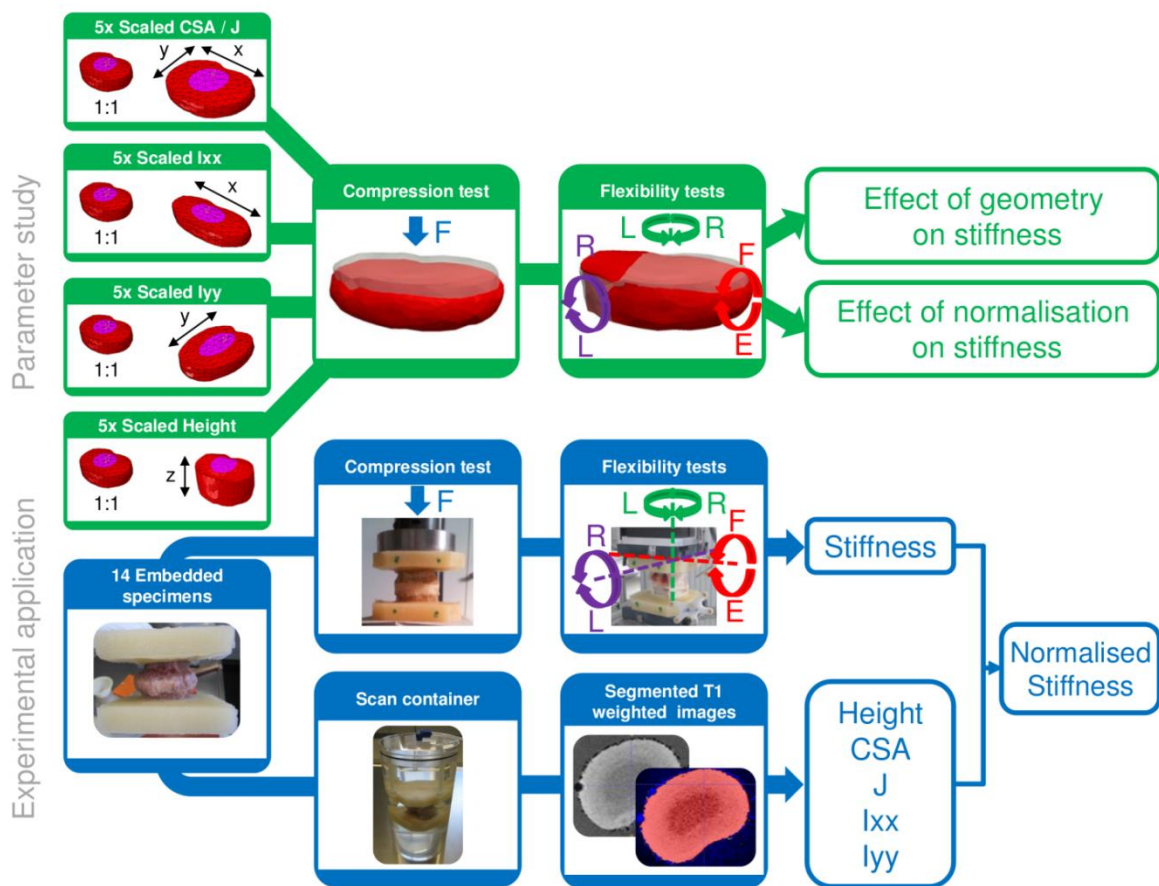


Fig. 1. Overview of the study. First, a parameter study was carried out on 20 FE models with various dimensions. Axial compression, torsion, lateral bending or flexion/extension were simulated and their apparent stiffness and moduli computed. The second part of the study dealt with the normalisation by geometry of experimental IVD stiffness measured from the data of biomechanical tests on 14 human intervertebral segments.

A constitutive law implemented in Fortran (UMAT) in a previous work (Maquer et al. 2012) was chosen. Identical Neo-hookean and fibre-reinforced anisotropic hyperelastic materials were simulating the material properties of nucleus pulposus and annulus fibrosus respectively in every model. A volumetric ratio of 42 % between nucleus and annulus was assumed and tension-only fibres were placed circumferentially in the annulus with a relative angle of $\pm 30^\circ$ relative to the transverse plane. The vertebral bodies, regarded as rigid bodies compared to the soft IVD, were not modelled.

To study the effect of CSA and J on compressive and torsional apparent stiffnesses, a first set was generated. X and y diameters of a mesh selected from the previous investigation were scaled simultaneously by 0.75, 1, 1.25, 1.5 and 1.75 while z was kept equal to the height of this original mesh. Axial compression up to 2 mm (15% strain) and torsion -3° to 3° were performed by applying displacements on the cranial nodes of the meshes, the nodes of the caudal surfaces being constrained. Then, two other sets were produced, to check the influence of I_{xx} and I_{yy} , by applying a similar scaling procedure either on x or y, leaving the other diameter and height unchanged and 3° lateral bending was performed when x was scaled, 3° flexion/extension when y was scaled. Finally, identical compression (15% strain), torsion, lateral bending and flexion/extension (-3° to 3°) tests were performed on the remaining set of models whose height was scaled from 0.75 to 2 as previously done keeping x and y unchanged.

As the stiffness definition remains variable in the literature, initial (K_i), final (K_f), total (K_t) apparent stiffnesses were computed for each set of FE data. K_i was defined as the initial slope of the loading curve (Markolf et al. 1974, Bisschop et al. 2013) and K_f as its final slope (Brown et al. 1957) and K_t as the ratio of the applied torque (or force) by the displacement achieved (Schmidt et al. 1998, Brown et al. 2002). An example on the experimental data can be found on Fig. 2.

The main diameters x and y of an ellipse fitted to the middle cross-section (Python script) of each model were used to approximate their CSA, J, I_{xx} and I_{yy} and compute the apparent moduli:

$$CSA_{\text{ellipse}} = \pi * x * y$$

$$J_{\text{ellipse}} = \frac{\pi (x^3 * y + y^3 * x)}{64}$$

$$I_{xx_{\text{ellipse}}} = \frac{\pi (y^3 * x)}{64}$$

$$I_{yy_{\text{ellipse}}} = \frac{\pi (x^3 * y)}{64}$$

To assess the geometry on the stiffness measurements and evaluate the benefit of the normalisation, the apparent stiffnesses and moduli were plotted against CSA, J , I_{xx} , I_{yy} and H . Finally, for verification, the procedure was repeated to the 4 sets of meshes with linear elastic material properties ($E = 3000$ MPa, $\nu = 0.3$).

2.3 Experimental application

After approval of the Ethics Committee of the Medical University of Vienna, 14 segments (T12-L1, L2-L3, L4-L5) were extracted from 6 human lumbar spines (63-89 y.o). All specimens were taken from individuals who voluntarily donated their bodies to the Center of Anatomy and Cell Biology of the Medical University of Vienna for postmortem studies by their last will. The posterior bony elements of the vertebrae and all soft tissues but intervertebral discs were removed. The free endplates of the surrounding vertebrae were embedded in a 10mm-thick layer of PMMA (polymethylmethacrylate). The specimens were stored at -20°C in sealed polyethylene bags and thawed at temperature room (20°C) the night before any manipulations (Fig. 1).

To minimize assumptions on the shape of the intervertebral discs when calculating the CSA and moments of inertia of the samples, T1-weighted anatomical images were acquired from each specimens placed in a custom-built container filled with 0.9% saline solution on a 3T VERIO Siemens MRI system (3D VIBE sequence, parameters: TR/TE = 12ms/5.58ms, 2 averages, flip angle 10 degrees, field of view 128x128x160, 0.25x0.25x0.5 mm³ resolution, a 15-channel knee coil was used for transmission and reception). ITKsnap (Yushkevich et al. 2006) was used to segment the IVD from the rest of the image (Fig. 1). The resolution being known ($x=0.25\text{mm}$, $y=0.25\text{mm}$, $z=0.5\text{mm}$), the volume (V) of the disc was calculated by summing the volume of the segmented voxels V_i (M voxels per disc). A similar approach was performed on the cross-sectional area A_i of voxels of the cross-section of the disc (N voxels per cross-section) to compute CSA, J , I_{xx} , I_{yy} using a Python script.

To facilitate the calculation of the moments of inertia of the disc, an in-plane rotation was applied to the segmented image to fit the disc's lateral and anteroposterior diameters to the x and y -axis of the coordinate system of the image. Special care was also taken to relate the moment of inertia calculation to the centroid (C_x , C_y) of its cross-section. Finally, the average height (H) of the specimen was determined from the values of CSA and V . The

anatomical data, polar and area moments of inertia of each specimen can be found in TableA.1 in the appendix:

$$\begin{aligned} \text{CSA} &= \sum_i^N A_i & V &= \sum_i^M V_i & H &= \frac{V}{\text{CSA}} \\ I_{xx} &= \sum_i^N (y_i - Cy)^2 & I_{yy} &= \sum_i^N (x_i - Cx)^2 & J &= I_{xx} + I_{yy} \end{aligned}$$

After the scanning, the samples were wrapped in 0.9% saline-soaked gauzes and non-destructive quasi-static experiments were conducted. Axial compression up to 1000 N and release was applied 5 times on the specimens at constant loading rate (2000 N/min) via a servohydraulic device (MTS, Bionix, U.S.A.) after alignment with the load axis. The displacement of the cranial vertebral body was recorded. Torsional and bending tests (bilateral torsion/bending, flexion/extension) were conducted on a spinal loading simulator without pre-load (Gédet et al. 2007, Gédet et al. 2009). Pure moments (-5 to 5 Nm) were applied 5 times on each specimen at constant displacement rate (0.8°/s) via brushless DC motors (EC40-BLD-120W-KL-2WE, Maxon, Switzerland) rigidly fixed to the PMMA layer of the cranial vertebral body. One X-shaped reflective marker (4 LEDs, resolution 0.1 mm) was attached on each PMMA layer. Their positions recorded via motion capture (Optotrak3020, Northern Digital, Canada) were used to compute the relative angular displacements of the vertebral bodies in Matlab (Mathworks, Natick, U.S.A.) while a 6-axis load cell (MC3A, AMTI, U.S.A.) recorded the moments applied on the superior vertebral body (Fig. 2).

The 5th loading-unloading cycle was kept for evaluation. As the data was irregularly distributed, a mathematical fit proved necessary to assess the compliance of our samples. An exponential and a double sigmoid function were fitted to the compression, rotational or bending data via a minimization of the residuals (optimize.leastsq, Python, vanRossum and deBoer 1991). The fit quality was assessed by coefficient of determination also computed from the residuals (Smit et al. 2011).

K_i , K_f , K_t were determined from the fitted load-deflection data from all biomechanical tests for each specimen (Fig. 2). K_f and K_t were calculated at the same deformation for each specimen to include even the stiffest discs: a 3° angle or 15% strain. Finally, the apparent moduli were calculated by normalising those measured stiffnesses using the morphological

data from the MRI as introduced in the previous section. To determine whether initial, final and total stiffnesses provide equivalent information about the intervertebral disc, correlations between K_i , K_f and K_t before and after normalisation were computed. Extra correlations between the normalised total stiffness of the 4 biomechanical tests were also performed.

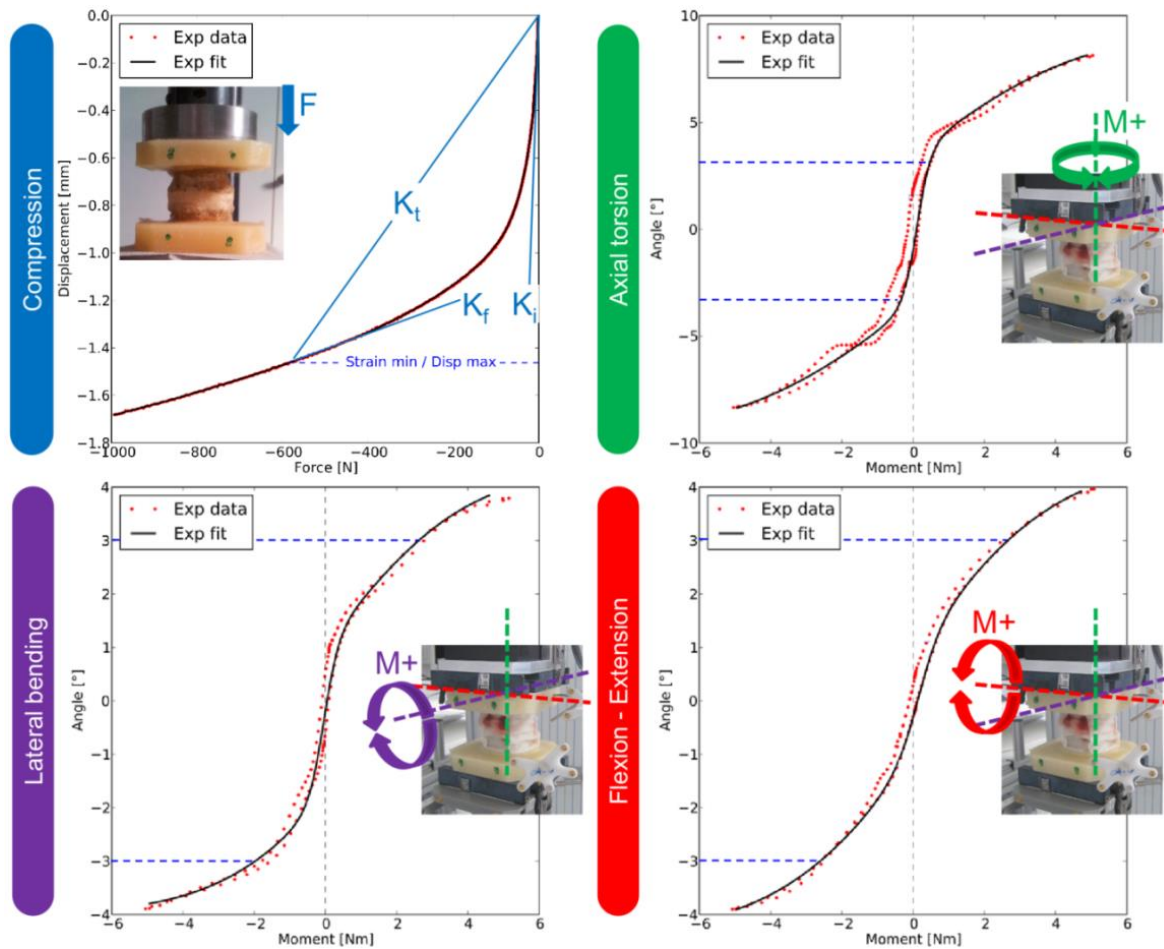


Fig. 2. An exponential function or a double sigmoid (Exp fit) was fitted to the experimental data (Exp data). K_i , K_f and K_t were computed as the initial slope, major slope of the curves and force applied over the displacement (or moment/angular displacement) respectively.

3. Results

3.1 Outcomes of the parameter study

Each simulation lasted 1 min on a 4-processors 3GHz PC with 24GB RAM (~2000 elements). As expected, a larger or a thinner IVD proved to be stiffer no matter the biomechanical test and regardless of the material (linear elastic or anisotropic hyperelastic). However, although

K_i , K_f and K_t were obviously equivalent with a linear elastic disc, they were clearly distinct when a non-linear material was used. As expected, the normalisation cancelled completely the change of stiffness with geometry in case of a linear elastic material, the apparent moduli K_i^N , K_f^N , K_t^N being identical. Such results were not obtained with the IVD but the normalisation attenuated the effect of geometry on the apparent stiffnesses especially on K_i (Fig. 3 and Fig. 4).

3.2 Experimental results

The fitting of the exponential and double-sigmoid to the experimental load-deflection data was satisfactory enough for stiffness calculation ($R^2 > 0.95$). The stiffness correlations between left (L in Fig. 1.) and right (R) torsion ($R^2 \sim 0.96$) and lateral bending ($R^2 \sim 0.97$) were excellent. The tested IVDs had a symmetrical behaviour in torsion and lateral bending, thus only stiffnesses measured from right torsion and bending were used in the rest of the study. Flexion and extension were still distinguished as only lower correlation was found ($R^2 \sim 0.73$).

For verification purposes, the experimental stiffnesses were compared to data from the literature data whenever a similar experiment was found. While the mean of each measurement was comparable to the literature, the standard deviations were large (Table1).

The full set of height, age, spine level, CSA, J, I_{xx} , I_{yy} , apparent stiffnesses and moduli for the 14 specimens can be found in TableA.1 in Appendix. Analysis of this table confirmed that larger IVDs were generally stiffer although exceptions were common especially when focusing on the apparent moduli. The correlations of K_i against K_f and K_t were significant for every load case and were significantly improved by the normalisation (Table2).

Further correlations showed that the total apparent modulus from the compression test could not be related to the apparent moduli of the other tests. However, significant correlations were found between the apparent moduli from torsion, lateral bending, flexion and extension tests (Fig. 5).

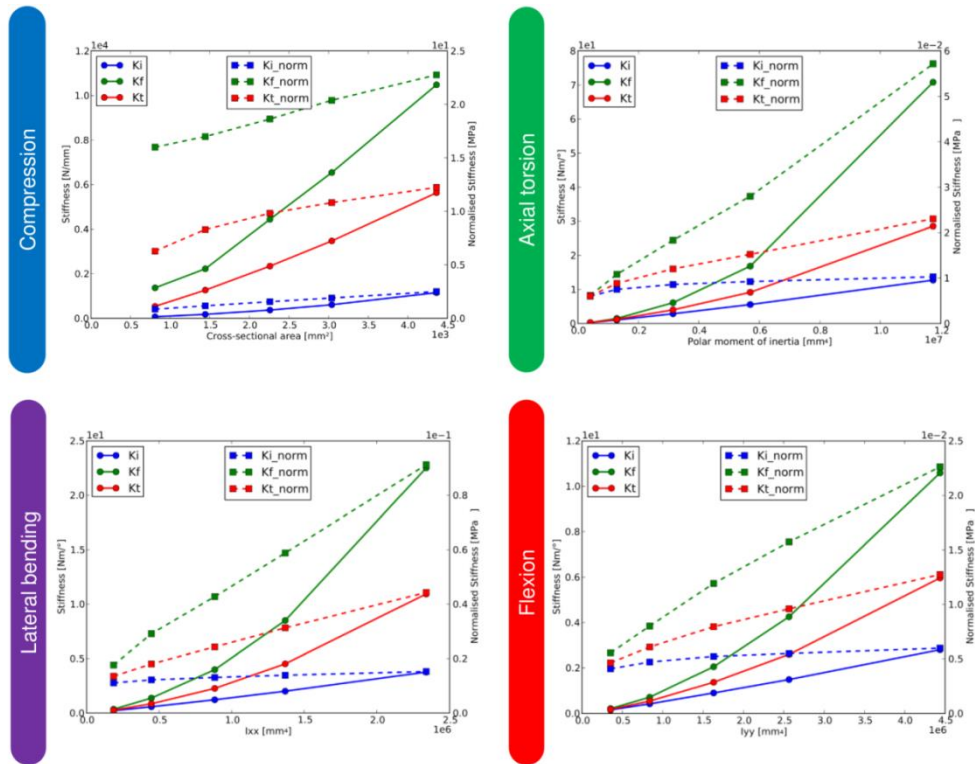


Fig. 3. Effect of CSA, J , I_{xx} , I_{yy} and normalisation on FE stiffnesses. No matter the type of stiffness, it increased with CSA, J , I_{xx} , I_{yy} . The normalisation only attenuated this tendency.

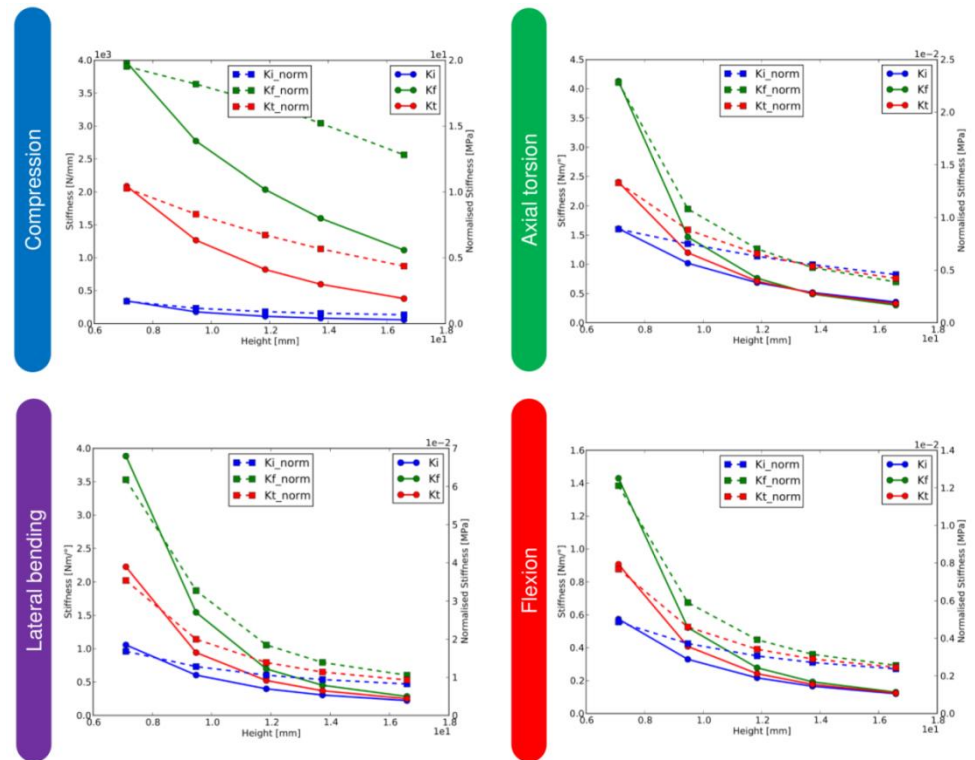


Fig. 4. Effect of H and normalisation on FE stiffnesses. No matter the type of stiffness, it decreased with H . The normalisation only attenuated this tendency.

Table 1. Stiffness compared to the available literature for human lumbar levels. [1] Showalter et al. 2012, [2] Brown et al. 1957, [3] Schmidt et al. 1998, [4] Smit et al. 2011.

		Current study	Literature data
Compression	N/mm	K_i	0.009±0.01
		K_f	1009±550
		K_t	1734±446 [1]
Axial torsion	Nm/°	K_i	327±210
		K_f	1.393±1.3
		K_t	2.273±2.09
Lateral bending	Nm/°	K_i	1.451±1.58
		K_f	2.2
		K_t	1.35 [3]
Flexion	Nm/°	K_i	0.567±0.35
		K_f	1.424±1.0
		K_t	0.863±0.72
Extension	Nm/°	K_i	0.309±0.22
		K_f	0.133±0.06 [4]
		K_t	0.781±0.94
		K_i	0.512±0.42
		K_f	0.9
		K_t	0.9 [3]
		K_i	0.313±0.21
		K_f	0.138±0.067 [4]
		K_t	0.832±0.75
		K_i	0.538±0.58
		K_f	1.75
		K_t	1.75 [3]

Table 2. The coefficient of determination (R^2) between measured stiffnesses (K_i against K_f and K_t) are displayed on the first line of this table, the second line focuses on the normalised ones (K_i^N against K_f^N and K_t^N).

R^2	Compression				Axial torsion				Lateral bending				Flexion				Extension				
	K_f	K_f^N	K_t	K_t^N	K_f	K_f^N	K_t	K_t^N	K_f	K_f^N	K_t	K_t^N	K_f	K_f^N	K_t	K_t^N	K_f	K_f^N	K_t	K_t^N	
K_i	0.56		0.75		0.95		0.97		0.79		0.75		0.45		0.58		0.62		0.79		
K_i^N		0.74		0.83		0.97		0.98		0.85		0.87		0.57		0.70		0.78		0.89	

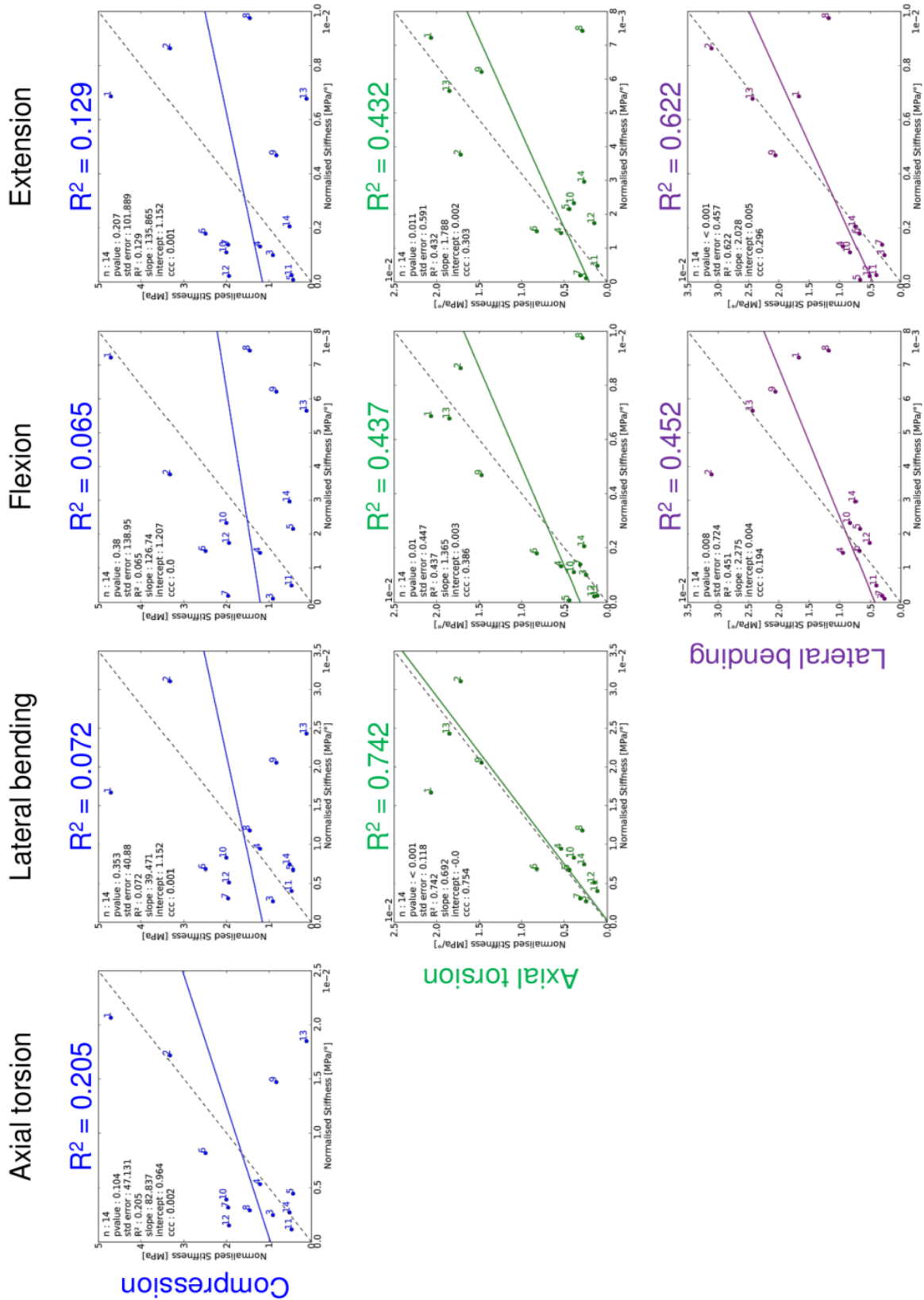


Fig. 5. Correlations of K_t^N between biomechanical tests. Compressive stiffness could not be related to the other tests' stiffnesses while torsion, bending and flexion/extension results were significantly correlated ($p < 0.05$).

4. Discussion

Scientific publications about biomechanical testing of the IVD are abundant. Yet, compression, torsion, lateral bending and flexion-extension were hardly performed successively on a set of human specimens with systematic computation of initial, final and total stiffnesses. Besides, large discrepancies due to diverse setups, protocols and specimen variability induce large standard deviations in the measurements, making inter-specimen comparisons challenging as long as no standard normalisation protocol is defined. Therefore, this study is introducing a normalisation method for every usual biomechanical test, tested on FE models and applied to human specimens of various sizes.

Our FE parameter study confirms the influence of the geometry on the disc's mechanical response: the larger the cross-sectional area, polar moment of inertia or area moments of inertia or the smaller the height, the stiffer the disc for every biomechanical test (Natarajan et al. 1999, Showalter et al. 2012). The effect of normalisation was also evaluated on IVDs with linear and non-linear materials. The normalised stiffness computed with a linear elastic disc is a constant apparent modulus. However, although the effect of the size when a more realistic material is chosen for the IVDs (non-linear hyperelastic constitutive law) is attenuated but not suppressed as geometrical and material non-linearity arise in this case. A non-linear material behaves more or less linearly for very small deformation. Therefore, it is not surprising that the outcome of the normalisation of K_i , the initial slope of the load-deflection curves, is almost a constant apparent modulus K_i^N . The material non-linearity could have been accounted for by normalising the measured stiffnesses by the relations between stiffness, H , CSA, J , I_{xx} and I_{yy} obtained from the non-linear FE simulations. This will be a possibility when the FE models of the IVD will be reliable enough to mimic completely the mechanics of a real intervertebral disc. As the current state of art is not that advanced yet, the FE models were used in this study only to verify the influence of the normalisation on the stiffness.

The experimental stiffnesses calculated presented large standard deviations, even after normalisation. The specimens were extracted from different donors whose age was ranging between 63 and 89 with a high variability in their height and area. With such a span, it would not be surprising to encounter diverse degrees of degeneration within our set of samples. Moreover, the apparent moduli computed from compression data do not correlate

with the moduli of the other tests. In fact, Michalek et al. (2010) showed that the disc degeneration affects differently compressive and torsional response, a loss of pressurization explaining the alteration in compression, a fibre disruption the change in torsion mainly because the collagen fibres only buckle when compressed but offer a strong stiffness in tension. On the other hand, the significant correlation between torsion, lateral bending, flexion and extension apparent moduli suggests that the behaviour of the IVD for those loading modes is affected by the same condition, potentially the fibre disruption hypothesised by Michalek et al. (2010). The disc degeneration influences the intervertebral stiffness, so does the presence of tears in the annulus (Haughton et al. 1999). Nevertheless, the behaviour of our samples was symmetrical in left and right torsion and lateral bending: either the intervertebral discs did not present major defects or the tears affect the mechanical response of the IVD to left or right solicitation similarly. Finally, the significant stiffness correlations obtained between initial, final or total stiffness suggest that those measures are not contradictory. Hence, it is somehow possible to relate the overall mechanical response of the intervertebral disc to its earliest stage of deformation, the neutral zone known to be a more sensitive measure of spinal destabilization than the range of motion (Smit et al. 2011).

A fast VIBE sequence was chosen for the imaging because it allows acquisition of the data in a relatively short time (~ 12 minutes). The obtained images were used for the fully automated computation of height, cross-sectional area, polar moment and area moments of inertia. To ensure proper loading of the RF coil and to avoid drying of the specimen, the studied samples were scanned in physiological saline solution and not in air. No swelling was observed for the duration of the measurements.

There are few limitations to be aware of. The removal of the posterior parts of the vertebrae and surrounding tissues obviously influences the mechanical behaviour of the segments. Then, to be reliable, in vitro testing procedures should be performed with well-controlled conditions. Thus, quasi-static tests were conducted, since the intervertebral compliance is dependent on the loading rate and the hydration of the disc. Nevertheless, various loading rates would most likely offset the stiffness measurements without deteriorating the correlation between quasi-static and dynamic mechanical tests results (vanEngelen et al. 2012). Finally, the specimens were frozen and thawed three times

(preparation/MRI/testing) but Tan and Uppuganti (2012) showed that the flexibility of human spinal segments is not affected by the four first freeze-thaw cycles.

In conclusion, a novel MRI-based stiffness normalisation protocol was proposed in this study. To our knowledge, normalisation has not been applied systemically to the stiffness of the intervertebral disc in all classical loadings (compression, torsion, lateral bending, flexion-extension). Moreover, accurate morphological data, computed automatically from anatomical MRI images, were used for the normalisation. Such a method, fast and easy to apply, can prove useful for inter-species, inter-individual and inter-level stiffness comparison of intervertebral discs and necessary when trying to relate its mechanical properties to its degree of degeneration.

Acknowledgments

The authors thank Alexander Bürki for his help regarding the mechanical tests, Urs Rohrer for producing the MRI-compatible container and Prof. Mauricio Reyes sharing his expertise in image processing (Institute of Surgical Technology and Biomechanics, University of Bern, Switzerland). We also would like to acknowledge Prof. Chris Boesch and Prof. Peter Vermathen (Department of Clinical Research, Inselspital, University of Berne, Switzerland) for the interesting discussions regarding MRI and its application to the intervertebral disc imaging. The project was made possible through funding obtained from the European Community, Grant Agreement n° PITN-GA-2009-238690-SPINEFX.

Appendix

Table A.1. The compressive (N/m), rotational and bending stiffnesses (Nm/°) and the apparent moduli (MPa) as well as the height, cross-sectional area (CSA), polar moment of inertia (J) and moments of inertia (Ixx, Iyy) used for the normalisation are presented for each test.

Specimen		1	2	3	4	5	6	7	8	9	10	11	12	13	14	
Age		63	70	70	70	63	68	68	68	71	71	71	89	89	87	
Level		L2-L3	T12-L1	L2-L3	L4-L5	L4-L5	L4-L5	L2-L3	T12-L1	T12-L1	L2-L3	L4-L5	L4-L5	T12-L1	L2-L3	
Height (mm)		9.5	7.5	11.3	9.8	8.2	10.5	9.8	7.6	6.9	9.7	7.7	10.5	7.3	7.8	
CSA (mm²)		1430	1637	2475	2301	1561	1899	1969	2037	1582	1936	2414	2328	1516	2367	
Compression	initial	K _i	0.026	0.025	0.009	0.001	0.001	0.007	0.006	0.007	0.003	0.012	0.001	0.005	0.015	0.004
		K _i ^N	0.170	0.116	0.040	0.004	0.006	0.037	0.030	0.024	0.013	0.062	0.004	0.021	0.072	0.013
	final	K _f	1.733	1.841	0.624	0.979	0.424	1.079	1.258	1.521	0.848	1.576	0.534	1.228	0.049	0.425
		K _f ^N	11.479	8.456	2.845	4.186	2.240	5.947	6.265	5.678	3.725	7.909	1.696	5.530	0.236	1.405
	total	K _t	0.711	0.724	0.199	0.283	0.082	0.452	0.394	0.389	0.188	0.399	0.147	0.431	0.024	0.156
		K _t ^N	4.706	3.328	0.908	1.210	0.432	2.493	1.962	1.453	0.827	2.004	0.468	1.942	0.117	0.516
J x10⁶ (mm⁴)		1.28	1.71	3.78	3.37	1.53	2.25	2.45	2.58	1.64	2.42	3.73	3.42	1.47	3.44	
Axial torsion	initial	K _i	2.833	3.187	0.561	1.302	0.561	1.315	0.498	0.572	3.317	0.459	0.417	0.279	4.129	1.052
		K _i ^N	0.021	0.014	0.002	0.004	0.003	0.006	0.002	0.002	0.014	0.002	0.001	0.001	0.021	0.002
	final	K _f	5.119	5.046	1.098	1.997	1.098	1.426	0.646	0.811	4.309	1.003	0.524	0.679	6.286	1.173
		K _f ^N	0.038	0.022	0.003	0.006	0.006	0.007	0.003	0.002	0.018	0.004	0.001	0.002	0.031	0.003
	total	K _t	2.792	3.913	0.833	1.832	0.833	1.765	0.797	0.992	3.484	0.980	0.566	0.499	3.725	1.199
		K _t ^N	0.021	0.017	0.002	0.005	0.004	0.008	0.003	0.003	0.015	0.004	0.001	0.002	0.018	0.003
Ixx x10⁵ (mm⁴)		4.41	5.64	14.8	10.5	4.99	7.61	8.51	9.59	5.42	7.56	11.5	11.0	5.15	12.6	
Lateral bending	initial	K _i	0.614	1.231	0.211	0.831	0.260	0.262	0.188	0.945	0.729	0.326	0.264	0.332	0.813	0.876
		K _i ^N	0.013	0.016	0.002	0.008	0.004	0.004	0.002	0.007	0.009	0.004	0.002	0.003	0.011	0.005
	final	K _f	0.967	14.335	0.416	1.370	0.753	0.959	0.400	2.527	2.979	1.053	1.253	1.076	2.312	1.490
		K _f ^N	0.021	0.191	0.003	0.013	0.012	0.013	0.005	0.020	0.038	0.014	0.008	0.010	0.033	0.009
	total	K _t	0.776	2.334	0.354	1.009	0.407	0.495	0.268	1.486	1.606	0.644	0.607	0.539	1.720	1.192
		K _t ^N	0.017	0.031	0.003	0.009	0.007	0.007	0.003	0.012	0.021	0.008	0.004	0.005	0.024	0.007
Iyy x10⁶ (mm⁴)		0.84	1.15	2.3	2.32	1.03	1.49	1.6	1.62	1.1	1.67	2.58	2.32	0.951	2.18	
Flexion	initial	K _i	0.582	0.466	0.100	0.302	0.096	0.230	0.139	0.630	0.702	0.241	0.103	0.163	0.298	0.334
		K _i ^N	0.007	0.003	0.000	0.001	0.001	0.002	0.001	0.003	0.004	0.001	0.000	0.001	0.002	0.001
	final	K _f	0.721	1.903	0.270	0.434	0.118	0.264	0.236	2.161	1.542	0.391	0.203	0.293	1.213	1.896
		K _f ^N	0.008	0.012	0.001	0.002	0.001	0.002	0.001	0.010	0.010	0.002	0.001	0.001	0.009	0.007
	total	K _t	0.608	1.319	0.202	0.309	0.010	0.254	0.225	2.078	0.743	0.188	0.085	0.049	0.885	0.572
		K _t ^N	0.007	0.009	0.001	0.001	0.000	0.002	0.001	0.010	0.005	0.001	0.000	0.000	0.007	0.002
Extension	initial	K _i	0.589	0.175	0.072	0.293	0.102	0.232	0.127	0.680	0.703	0.247	0.104	0.176	0.454	0.373
		K _i ^N	0.007	0.001	0.000	0.001	0.001	0.002	0.001	0.003	0.004	0.001	0.000	0.001	0.003	0.001
	final	K _f	0.708	1.851	0.072	0.309	0.117	0.239	0.134	3.434	0.979	0.340	0.104	0.239	1.070	1.331
		K _f ^N	0.008	0.012	0.000	0.001	0.001	0.002	0.001	0.016	0.006	0.002	0.000	0.001	0.008	0.005
	total	K _t	0.640	0.575	0.023	0.341	0.271	0.213	0.032	1.582	0.986	0.400	0.161	0.386	0.738	0.826
		K _t ^N	0.007	0.004	0.000	0.001	0.002	0.001	0.000	0.007	0.006	0.002	0.000	0.002	0.006	0.003

References

- Adams M.A., Dolan P., Hutton W.C. and Porter R.W. 1990. Diurnal changes in spinal mechanics and their clinical significances. *J Bone Joint Surgery*.72:266–70
- Amonoo-Kuofi, H.S. 1991. Morphometric changes in the heights and anteroposterior diameters of the lumbar intervertebral discs with age. *J Anat*. 175:159–168
- Alini M., Stephen M. Eisenstein S.M, Ito K., Little C., Kettler A.A., Masuda K., Melrose J., Ralphs J., Stokes I., Wilke H.J. 2008. Are animal models useful for studying human disc disorders / degeneration? *Eur Spine J*. 17:2–19
- Beckstein J.C., Sen S., Schaer T.P., Vresilovic E.J. and Elliott D.M. 2008. Comparison of animal discs used in disc research to human lumbar disc axial compression mechanics and glycosaminoglycan content. *Spine*. 33:E166–E173
- Belavy D.L., Armbrrecht G. and Felsenberg D. 2012. Evaluation of lumbar disc and spine morphology: long-term repeatability and comparison of methods. *Physiol. Meas*. 33: 1313–1321
- Bisschop A., Kingma I., Bleys R.L.A.W., Paul C.P.L., van der Veen A.J., van Royen B.J., van Dieën J.H. 2013. Effects of repetitive movement on range of motion and stiffness around the neutral orientation of the human lumbar spine. *J Biomech*. 46: 187–191
- Brown T., Hansen R.J., Yorra A.J. 1957. Some mechanical tests on the lumbosacral spine with particular reference to intervertebral disc. *J Bone Joint Surg*. 39:1135–1164
- Brown M.D., Holmes D.C., and Heiner A.D. 2002. Measurement of Cadaver Lumbar Spine Motion Segment Stiffness. *Spine*. 27:918–922
- Dolan P. and Adams M.A. 2001. Recent advances in lumbar spinal mechanics and their significance for modelling. *Clin Biomech*. 16-Suppl 1:S8-S16
- Elliott D.M. and Sarver J.J. 2004. Young investigator award winner: validation of the mouse and rat disc as mechanical models of the human lumbar disc. *Spine*. 29:713–722
- Fouré A., Cornu C. and Nordez A. 2012. Is tendon stiffness correlated to the dissipation coefficient? *Physiol. Meas*. 33:N1–N9
- Gédet P., Thistlethwaite P.A. and Ferguson S.J. 2007. Minimizing errors during in vitro testing of multisegmental spine specimens: considerations for component selection and kinematic measurement. *J Biomech*. 40:1881-1885
- Gédet P., Thistlethwaite P.A. and Ferguson S.J. 2009. Comparative biomechanical investigation of a modular dynamic lumbar stabilization system and the Dynesys system. *Eur Spine J*. 18:1504-1511
- Houghton V.M., Lim T.H. and An H. 1999. Intervertebral disk appearance correlated with stiffness of lumbar spinal motion segments. *AJNR Am J Neuroradiol*. 20:1161-1165
- Kirkaldy-Willis W.H. and Farfan H.F. 1982. Instability of the lumbar spine. *Clin Orthop Relat Res*. 165:110–123
- Koeller W., Meier W., Hartmann F. 1984. Biomechanical properties of human intervertebral discs subjected to axial dynamic compression: A comparison of lumbar and thoracic discs. *Spine*. 7:725–33
- Koeller W., Muehlhaus S., Meier W., Hartmann F. 1986. Biomechanical properties of human intervertebral discs subjected to axial dynamic compression-influence of age and degeneration. *J Biomech*. 19:807–16
- Krismer M., Haid C., Behensky H., Kapfinger P., Landauer F. and Rachbauer F. 2000. Motion in lumbar functional spine units during side bending and axial rotation moments depending on the degree of Degeneration. *Spine*. 25:2020-2027

- Leone A., Guglielmi G., Cassar-Pullicino V.N., Bonomo L. 2007. Lumbar Intervertebral Instability: A Review. *Radiology*. 245:1
- Maquer G., Schwiedrzik J. and Zysset P.K. 2012. Embedding of human vertebral bodies leads to higher ultimate load and altered damage localisation under axial compression. *Comput Methods Biomech Biomed Eng*. iFirst article, 1–12
- Markolf K.L., Morris J.M. 1974. The structural components of the vertebral disc: a study of their contribution to the ability of the disc to withstand compressive force. *J Bone Joint Surg*. 56:675–687
- Michalek A.J., Funabashi K.L. and Iatridis J.C. 2010. Needle puncture injury of the rat intervertebral disc affects torsional and compressive biomechanics differently. *EurSpineJ*. 19:2110–2116
- Mosekilde L., Mosekilde L. and Danielsen C.C. 1987. Biomechanical competence of vertebral trabecular bone in relation to ash density and age in normal individuals. *Bone*. 8:79–85
- Nachemson A.L., Schultz A.B. and Berkson M.H. 1979. Mechanical properties of human lumbar spine motion segments: influences of age, sex, disc level and degeneration. *Spine*. 4:1-8
- Natarajan R.N. and Andersson G.B.J. 1999. The influence of lumbar disc height and cross-sectional area on the mechanical response of the disc to physiologic loading. *Spine*. 24:1873–1881
- Panjabi M. 2003. Clinical spinal instability and low back pain. *Journal of Electromyography and Kinesiology*. 13:371–379
- Qasim M., Natarajan R.N, An H.S., Andersson G.B.J. 2012. Initiation and progression of mechanical damage in the intervertebral disc under cyclic loading using continuum damage mechanics methodology: A finite element study. *JBiomech*. 45:1934–1940
- Ryan E.D., Thompson B.J., Herda T.J., Sobolewski E.J., Costa P.B., Walter A.A. and Cramer J.T. 2011. The relationship between passive stiffness and evoked twitch properties: the influence of muscle CSA normalization. *Physiol. Meas*. 32:677–686
- Schmidt T.A., An H.S., Lim, T.H., Nowicki. B.H. and Haughton V.M. 1998. The stiffness of lumbar spinal motion segments with a high-intensity zone in the annulus fibrosus. *Spine*. 23:2167–2173
- Showalter B.L., Beckstein J.C., Martin J.T., Beattie E.E., Espinoza Orías A.A., Schaer T.P., Vresilovic E.J. and Elliott D.M. 2012. Comparison of animal discs used in disc research to human lumbar disc. *Spine*. 7:E900–E907
- Smit T. H., van Tunen M.S.L.M., van der Veen A.J., Kingma I., van Dieën J.H. 2011. Quantifying intervertebral disc mechanics: a new definition of the neutral zone. *BMC Musculoskeletal Disorders*. 12:38
- Stokes I.A., Frymoyer J.W. 1987. Segmental motion and instability. *Spine*. 12:688–691
- Tan J.S. and Uppuganti S. 2012. Cumulative Multiple Freeze-Thaw Cycles and Testing Does Not Affect Subsequent Within-Day Variation in Intervertebral Flexibility of Human Cadaveric Lumbosacral Spine. *Spine*. 37:E1238–E1242
- Tanaka N., An H.S., Lim T., Fujiwara A., Jeon C., Haughton V.M. 2001. The relationship between disc degeneration and flexibility of the lumbar spine. *The Spine Journal*. 1:47–56
- Van Engelen S.J.P.M., Ellenbroek M.H.M., van Royen B.J., de Boer A., van Dieën J.H. 2012. Validation of vibration testing for the assessment of the mechanical properties of human lumbar motion segments. *JBiomech*. 45:1753–1758

- Van Rossum G. and de Boer J. 1991. Interactively testing remote servers using the python programming language. *CWI Q.* 4:283–303
- Wise C. 2011. Back Pain and Common Musculoskeletal Problems. *ACP Medicine.*
- Yushkevich P.A., Piven J., Hazlett H.C., Smith R.G., Ho S., Gee J.C. and Gerig G.. 2006. User-guided 3D active contour segmentation of anatomical structures: Significantly improved efficiency and reliability. *NeuroImage.* 31:1116 – 1128

Chapter 5: An MRI-based methodology for biomechanical evaluation of degenerated intervertebral discs

From the manuscript

Human intervertebral disc stiffness correlates better with the Otsu threshold computed from axial T₂ map of its posterior annulus fibrosus than with clinical classifications

G. Maquer ^a, V. Brandejsky ^b, P. Vermathen ^b, L.M. Benneker ^c, A. Watanabe ^d and P. Zysset ^a

^a Institute of Surgical Technology and Biomechanics, University of Berne, Switzerland

^b Department of Clinical Research, Inselspital, University of Berne, Switzerland

^c Department of Orthopaedic Surgery, Inselspital, University of Berne, Switzerland

^d Department of Orthopaedic Surgery, Teikyo University, Ichihara, Japan

Submitted to: Medical Engineering & Physics (March, 20th 2013)

Abstract

Disc degeneration, sometimes associated with low back pain and abnormal spinal motions, represents a major health issue with high costs. A non-invasive degeneration assessment via qualitative or quantitative MRI (magnetic resonance imaging) is possible. Yet, no relation between mechanical properties and T_2 maps of the intervertebral disc (IVD) was considered albeit T_2 relaxation time values quantify the degree of degeneration. Therefore, MRI scans and mechanical tests were performed on 14 human lumbar intervertebral segments freed from posterior elements and all soft tissues but the IVD. Degeneration was evaluated in each specimen using morphological criteria, qualitative T_2 weighted images and quantitative axial T_2 map data and their stiffnesses were calculated from the load-deflection curves of *in vitro* compression, torsion, lateral bending and flexion/extension tests. In addition to mean T_2 , the OTSU threshold of T_2 (T_{OTSU}), a robust and automatic histogram-based method that computes the optimal threshold maximizing the distinction of two classes of values was calculated for anterior, posterior, left and right regions of each annulus fibrosus (AF). While mean T_2 and degeneration schemes were not related to the IVDs' mechanical properties, T_{OTSU} computed in the posterior AF correlated significantly with those classifications but also with all the stiffnesses.

Keywords: Human intervertebral disc, Experimental stiffness, Degeneration grade, MRI, Axial T_2 maps

1. Introduction

Low back pain concerns at least half of the western population and is responsible for high health care expenses every year (Panjabi 2003). Its origin is multifactorial. In case of mechanical failure, degeneration of the intervertebral disc (IVD) is the initiating event and is associated with high risk of prolapse and herniation (Trattnig et al. 2010). The intervertebral disc, composed of the fibrous annulus fibrosus and the gelatinous nucleus pulposus, ensures mobility of the segments and contributes to spinal stability (Kirkaldy-Willis et al. 1982, Stokes et al. 1987). As degeneration occurs, the pressure in the dehydrated nucleus decreases, the disc height reduces and the collagen structure is modified, eventually leading to initiation of lesions and protrusions in the annulus due to abnormal load distribution on the endplates (Dolan and Adams 2001). The stability of the segment is then affected by consequent alterations of the neutral zone (Panjabi 2003), range of motion (Tanaka et al., 2001) and stiffness (Haughton et al. 1999, Michalek et al. 2009).

Hence, effort has been put in developing non-invasive methods for detection and evaluation of degeneration. Considering the influence of water content and collagen structure on T_1 and T_2 relaxation times, an assessment based on qualitative clinical MRI (magnetic resonance imaging) or quantitative MRI is possible (Watanabe et al. 2007, Mwale et al. 2008, Marinelli et al. 2009). Notwithstanding the use of a mid-sagittal plane for most morphological (Thompson et al. 1990), $T_{1\rho}/T_2$ -weighted (Benneker et al. 2005) or T_2/T_2^* maps (Trattnig et al. 2010, Stelzeneder et al. 2012) -based grading schemes, few authors assert that axial T_2 maps are useful for visualisation of posterolateral protrusion thanks to a larger field of view (Watanabe et al. 2007, Hoppe et al. 2012).

Nonetheless, the standard procedure consists in classifying the degeneration into discrete grades, which is unspecific and dependent on the operator's experience. The mechanical properties of a disc can hardly be related to its degenerative level because of the large standard deviations within each grade (Krismer et al. 2000, Tanaka et al. 2001, Kettler et al. 2011). In addition, the impact of disc morphology on the biomechanical measurements is rarely considered (Elliott and Sarver 2004, Campana et al. 2007, Beckstein et al. 2008, Showalter et al. 2012).

In the knee cartilage, a disorganised collagen structure with high water content is associated with high T_2 values (Nieminen et al. 2001) while negative correlations between T_2 value, compressive Young modulus and dynamic modulus were found (Kurkijarvi et al 2004, Nissi et al 2007, Julkunen et al. 2008). Yet, no relation between mechanical properties and T_2 maps of the intervertebral disc was considered albeit T_2 values computed in nucleus and annulus regions potentially quantify the degree of degeneration (Stelzener et al. 2012).

Clinicians visually evaluate the hydration of the nucleus based on intensity and homogeneity of the T_2 signal. To achieve equivalent evaluations quantitatively, the measure of T_2 at various locations (Hoppe et al. 2012, Stelzener et al. 2012), entropy and geometry-based criteria (Mayerhofer et al. 2012) were recently proposed. Otsu is a robust method that computes the optimal threshold that maximizes the separability of two classes of values (Otsu et al. 1979). Being histogram-based and automatic, it produces an objective result unbiased by spatial information or by human interaction. Extensively used for the segmentation of the IVD (Michopoulou et al. 2008, Michopoulou et al. 2009, Chevrefils et al. 2009), it also bears information about homogeneity. The Otsu threshold of a homogenous image is equal to its mean value but it will be biased by the intensity and frequency of high intensity pixels possibly linked to the presence of annular tears (Trattnig et al. 2010).

Relying on the potential relation between quantitative T_2 maps and biochemical properties, the aim of this work is to propose a criterion for disc degeneration related to its mechanics and meeting the objectivity and simplicity requirements. The degeneration grades of 14 human lumbar intervertebral discs evaluated using MRI data and quantitative T_2 measures were compared to the specimens' stiffness in compression, torsion, lateral bending and flexion/extension.

2. Materials and methods

2.1 Qualitative and quantitative MRI imaging

Fourteen (14) spinal segments (T12-L1, L2-L3, L4-L5) were extracted from 6 human lumbar spines (age 63-89) after approval of the Ethics Committee of the Medical University of Vienna. All specimens were taken from individuals who voluntarily donated their bodies to the Center of Anatomy and Cell Biology of the Medical University of Vienna for postmortem studies by their last will. The posterior bony elements of the vertebrae were sectioned at

the pedicles and all soft tissues but the central intervertebral discs were removed. The endplates of the cranial and caudal vertebral bodies were embedded in a 10mm-thick layer of PMMA (polymethylmethacrylate). The specimens, stored in sealed polyethylene bags at -20°C were thawed at temperature room (20°C)

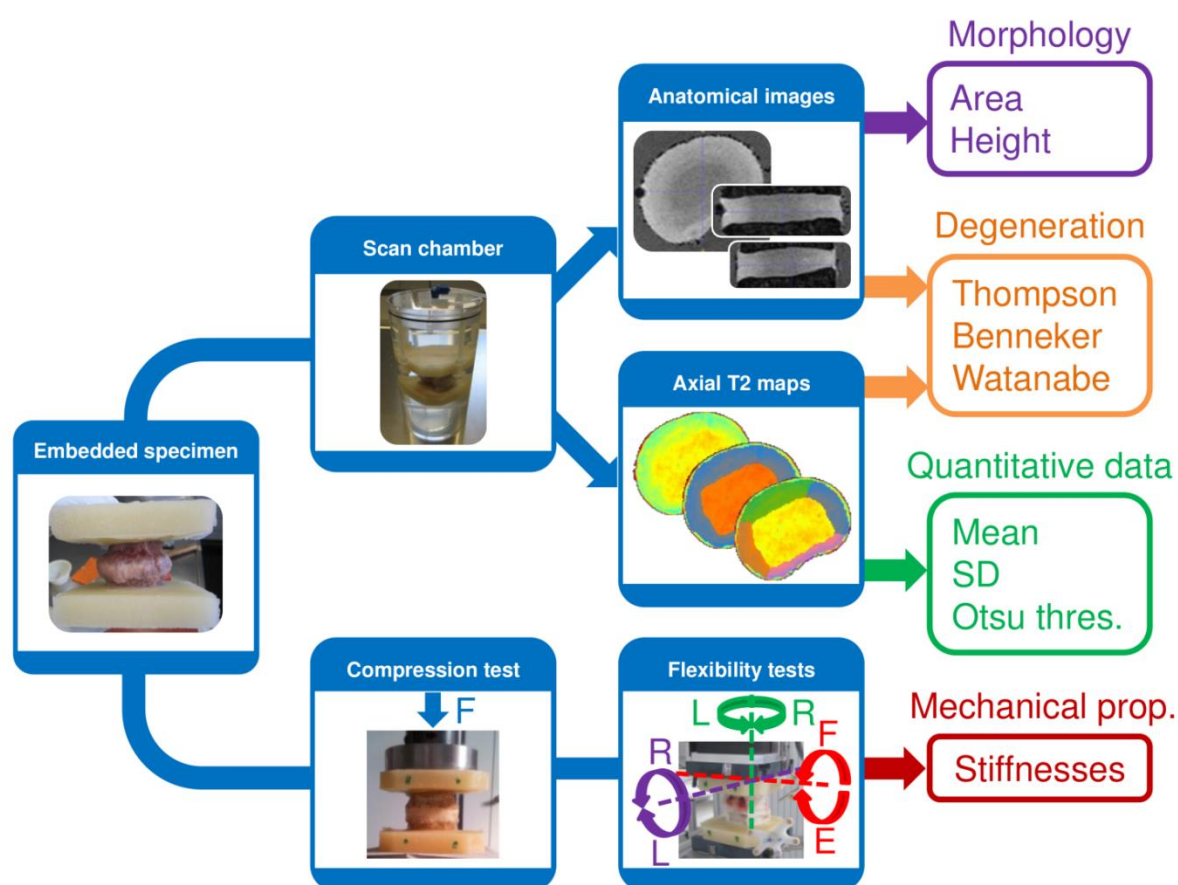


Fig. 1. Overview of the study. T_1 and T_2 weighted MRI and axial T_2 maps of 14 intervertebral segments were performed and morphological, degenerative and quantitative data were extracted or evaluated. The intervertebral stiffnesses were computed from the load-deflection curves of the tests in compression, torsion, lateral bending and flexion/extension. The relations between degenerative, quantitative and mechanical data were established.

the night before MRI imaging and placed in a custom-built container filled with 0.9% saline water to avoid drying of the specimen and to ensure sufficient loading of the RF coil. MRI scans were performed on a clinical 3T system (Verio, Siemens Healthcare, Germany) with a 15-channel knee coil. Anatomical T_1 ($T_R/T_E = 999/13$ ms) and T_2 -weighted images ($T_R/T_E = 4990/114$ ms) in axial, coronal and sagittal planes were acquired in order to document all pathological conditions. 0.3 mm in-plane resolution was achieved for each of the 0.8 mm

thick axial slices (128*256 mm² field of view (FOV), 384*768 matrix) and coronal/sagittal slices (3 mm thickness, 140*256 mm² FOV, 240*768 matrix).

For the axial T₂ mapping, a multi spin-echo sequence with 22 different echoes was chosen for its relatively short acquisition times. The sequence parameters were T_R = 3650 ms, first echo 12.5 ms and last echo 275 ms with steps of 12.5 ms, 106*199 mm² FOV and 204*384 matrix (0.5 mm resolution). Each T₂ map was calculated by exponential curve fitting using an in-house script from a 3mm thick slice acquired in the centre of the disc using the anatomical data to position the imaging plane (Matlab, Mathworks, Natick, U.S.A.).

Prior to the scanning of our specimens, 14 T₂ maps were taken from a test sample while the water temperature in the container increased from 9°C to 20°C to verify the influence of temperature on T₂. Then, to assess the stability and repeatability of the procedure, 2 sets of 6 T₂ maps were acquired on the test specimen every 30 minutes on two different days (D1, D2). Coefficient of variation (VC) and relative comparison of the mean T₂ value between D1 and D2 (Δ_{D1D2}) were evaluated for regions of interest in the nucleus and annulus:

$$CV = \frac{100 * SD}{Mean} \quad \Delta_{D1D2} = 100 * \frac{Mean_{D1} - Mean_{D2}}{Mean_{D1}}$$

Finally, the 16 samples were scanned. A whole imaging session lasted approximately 2.5 hours at controlled temperature (22°C) and the T₂ maps were acquired at the end of each session to limit the influence of temperature (Fig1.).

2.2 Apparent intervertebral moduli

To measure the stiffness of the samples, non-destructive quasi-static experiments were conducted after the scanning. The specimens were wrapped in 0.9% saline-soaked gauzes, aligned along the axis of a servohydraulic device (MTS, Bionix, U.S.A.) and compressed 5 times up to 1000 N at constant loading rate (2000 N/min). Each compression segment was followed by a release and the displacement of the superior vertebral body was monitored. Then, axial torsion, bilateral bending and flexion/extension tests were conducted without pre-load by applying 5 cycles of pure moments (-5 to 5 Nm) on the PMMA layer of the superior vertebral body at constant displacement rate (0.8°/s) via a spinal loading simulator (Gédet et al. 2007, Gédet et al. 2009). The positions of X-shaped reflective marker (4 LEDs,

resolution 0.1 mm) fixed to both PMMA layers were registered via motion capture (Optotrak3020, Northern Digital, Canada). The relative angular displacements of the vertebral bodies were then computed in Matlab (Mathworks, Natick, U.S.A.). Meanwhile, the moments applied on the superior vertebral body were measured with a 6-axis load cell (MC3A, AMTI, U.S.A.). Only the 5th loading-unloading cycle was kept for evaluation. Because of the irregular distribution of the data points, least square minimization of the residuals (Python, vanRossum and deBoer 1991) was utilised to fit exponential or double sigmoid functions on the load-deflection curves (Smit et al. 2011).

Stiffness (K, N/mm or Nmm/°) was determined from the fitted load-deflection data for all 4 biomechanical tests of each specimen as the ratio of the load over the displacement for the same deformation, a 3° angle or 15% strain, to include even the stiffest discs. Finally, normalisation of the stiffness was necessary to limit the influence of a disc's size on its mechanics and relate properly its stiffness to any degenerative alterations. Therefore, the apparent modulus (K^N , MPa) was calculated by normalising K by height (H, mm), area (CSA, mm²), polar moment of inertia (J, mm⁴) or area moment of inertia along the lateral (I_{xx}) or anteroposterior diameter (I_{yy}) computed from the voxels of the anatomical images:

$$K_C^N = \frac{K_C * H}{CSA} \qquad K_T^N = \frac{K_T * H}{J}$$

$$K_B^N = \frac{K_B * H}{I_{xx}} \qquad K_{F/E}^N = \frac{K_{F/E} * H}{I_{yy}}$$

2.3 Link between degeneration grade, quantitative MRI data and apparent modulus

Two clinicians evaluated independently the degeneration of the specimens via Thompson (Thompson et al. 1990), Benneker (Benneker et al. 2005) and Watanabe (Watanabe et al. 2007) grading systems without any knowledge of their stiffness using the anatomical images or the axial T₂ maps. A consensus table was established. The Otsu threshold (T_{OTSU}) was implemented in Python from Otsu et al (1979). Mean, Δ (Mean_{nucleus} - Mean_{annulus}) and T_{OTSU} were computed from each segmented T₂ map (ITKsnap, Yushkevich et al. 2006) for the

nucleus, the annulus and the anterior, posterior, left and right regions of the annulus to check if the regional T_2 values can discriminate the loading direction. Each AF region was determined by a 90° angle after an ellipse was automatically fitted to the IVD via a Python script and assuming a surface ratio of 43% between nucleus and annulus only if the distinction was not clear (Smit et al. 1997, Polikeit et al. 2003) (Fig1.). Finally, correlations between age, grading schemes, Mean, T_{OTSU} of each region and apparent moduli were established for every loading mode.

3. Results

The influence of temperature, the stability and the repeatability of the T_2 maps were checked. Even though the test specimen was scanned for a large span of temperature (from 9 to 20°C), the coefficient of variation (CV) for the T_2 maps of the intervertebral disc was less than 1.7%. At constant temperature, CV dropped to less than 1% and the difference between Day1 and Day2, Δ_{D1D2} , was less than 4%.

Grading, T_2 maps, Mean and T_{OTSU} for all disc regions and apparent moduli for the 14 specimens are presented in the appendix (TableA.1). As the data is sorted along increasing Thompson grade, the broad range of apparent moduli associated to each grade is obvious. Coefficients of determination (R^2) between age, grading, apparent moduli and T_2 were computed (Table1). The age of the donor could not be related to any of the grading schemes, apparent moduli or T_2 values. High correlations were found between the 3 grading schemes ($R^2 > 0.73$) but their relation with the mechanical properties was rather poor as only Thompson correlated significantly with K_C ($R^2 = 0.36$), K_T ($R^2 = 0.42$) and K_B ($R^2 = 0.32$). No link with mean T_2 in the nucleus and annulus and the grading parameter "classifications" were found but significant positive correlations were observed between the classifications and T_{OTSU} values computed in the annulus fibrosus and its posterior region (Fig2.).

Lateral bending moduli left or right were not linked to T_2 relaxation time computed in the left or right region of the annulus. The same observation was made between flexion/extension and mean T_2 of the anterior region. Interestingly, the highest correlations were established between T_{OTSU} computed in the posterior region and the apparent moduli of the torsional and bending tests K_T , K_B , K_E and K_F (Fig3.). Finally, the apparent modulus in compression K_C could not be related to any T_2 values.

Table 1. Coefficients of determination (R^2) computed between the degeneration grading systems, apparent moduli and values computed from the T_2 maps (mean T_2 and Otsu threshold) are represented. The significant values are bold ($p < 0.05$). Data of higher interest are highlighted in blue.

Age	Thompson			Benneker			Watanabe			Nucleus		Annulus		AF Anterior		AF Posterior		AF Left		AF Right			
	Mean	Th.	Mean	Mean	Th.	Mean	Mean	Th.	Mean	Th.	Mean	Th.	Mean	Th.	Mean	Th.	Mean	Th.	Mean	Th.	Mean	Th.	
-	0,08	0,12	0,16	0,17	0,16	0,12	0,13	0,10	0,07	0,10	0,12	0,06	0,06	0,21	0,19	0,02	0,02	0,06	0,21	0,19	0,02	0,02	
Thomp.	-	0,80	0,73	0,00	0,00	0,19	0,43	0,00	0,27	0,00	0,20	0,37	0,03	0,55	0,06	0,09	0,09	0,03	0,62	0,06	0,14	0,15	0,15
Benne.	0,80	-	0,90	0,00	0,02	0,23	0,52	0,03	0,27	0,03	0,21	0,42	0,03	0,62	0,14	0,15	0,15	0,03	0,62	0,14	0,14	0,15	0,15
Watan.	0,73	0,90	-	0,01	0,05	0,24	0,52	0,05	0,26	0,05	0,24	0,50	0,06	0,52	0,12	0,29	0,29	0,06	0,52	0,12	0,12	0,29	0,29
K_C	0,36	0,16	0,14	0,01	0,00	0,03	0,04	0,00	0,04	0,00	0,03	0,01	0,00	0,06	0,01	0,05	0,05	0,00	0,06	0,01	0,01	0,05	0,05
K_T^L	0,35	0,28	0,23	0,04	0,02	0,27	0,38	0,06	0,24	0,06	0,38	0,40	0,13	0,22	0,15	0,09	0,09	0,13	0,22	0,15	0,15	0,09	0,09
K_T^R	0,42	0,33	0,24	0,06	0,03	0,33	0,46	0,10	0,35	0,10	0,38	0,36	0,16	0,26	0,16	0,07	0,07	0,16	0,26	0,16	0,16	0,07	0,07
K_B^L	0,26	0,16	0,09	0,11	0,13	0,31	0,42	0,04	0,37	0,04	0,32	0,37	0,17	0,25	0,09	0,09	0,09	0,17	0,25	0,09	0,09	0,09	0,09
K_B^R	0,32	0,22	0,13	0,10	0,10	0,30	0,42	0,02	0,33	0,02	0,36	0,46	0,14	0,26	0,10	0,09	0,09	0,14	0,26	0,10	0,10	0,09	0,09
K_F	0,14	0,10	0,12	0,02	0,01	0,16	0,24	0,02	0,14	0,02	0,33	0,49	0,08	0,13	0,01	0,13	0,13	0,08	0,13	0,01	0,01	0,13	0,13
K_E	0,12	0,08	0,03	0,17	0,19	0,19	0,23	0,01	0,17	0,01	0,32	0,36	0,07	0,17	0,06	0,02	0,02	0,07	0,17	0,06	0,06	0,02	0,02

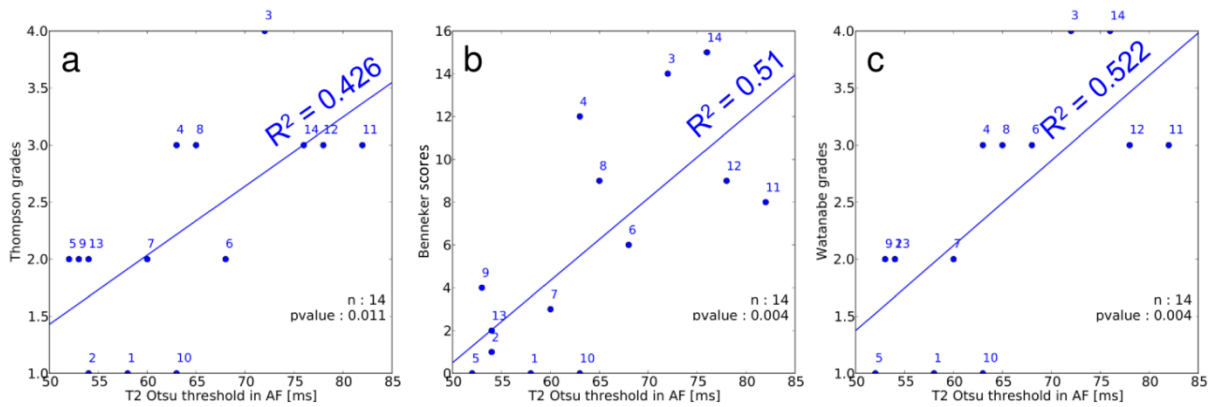


Fig. 2. Coefficient of determination (R^2) between the T_{OTSU} measured in the annulus fibrosus and Thompson (a), Benneker (b) and Watanabe (c) grading schemes.

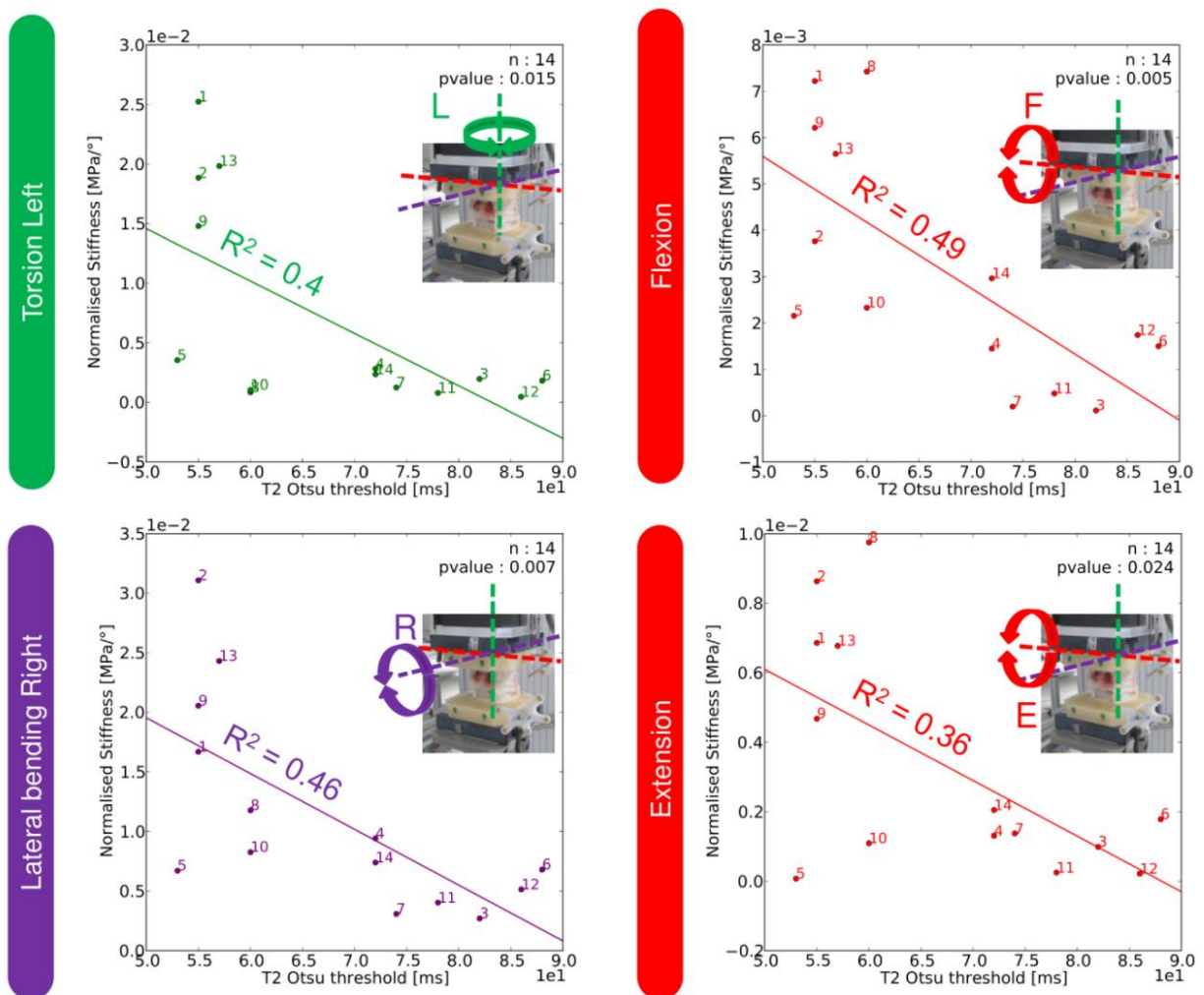


Fig. 3. Coefficient of determination (R^2) between the T_{OTSU} measured in the posterior annulus fibrosus and apparent moduli of the rotational and bending tests.

4. Discussion

The quantification of T_2 relaxation time is related to the biochemical properties of the intervertebral disc. This gives the advanced MRI methods the potential to evaluate objectively the disc degeneration (Mayerhofer et al. 2012). Although compressive Young modulus of the articular cartilage is connected to its mean T_2 value (Julkunen et al. 2008), such connection was not yet established for human intervertebral discs.

T_2 increases with temperature (Baron et al. 2011). However, the T_2 relaxation time was relatively constant for the range of temperature tested. The very low coefficient of variation obtained from our test images, confirms that T_2 is highly stable and repeatable at constant temperature (Gold et al. 2004). Slightly larger discrepancies were observed when performing day-to-day comparisons because of the different positions of the specimen and ROIs from one day to the other.

Two experts evaluated the degeneration of our samples by using the Thompson, Benneker and Watanabe disc degeneration classifications. Their ratings were performed independently but the evaluations are in good agreement. Albeit Thompson is solely based on morphology, Watanabe focuses on T_2 map signal while Benneker examines both T_{2w} signal and morphology, the grading schemes correlated well. Actually, regardless the method, it seems that the evaluation is mainly a matter of experience. However, if the mechanical properties of the disc are influenced by morphological and biochemical alterations induced by the degeneration process (Tanaka et al. 2001), they can hardly be linked to the standard evaluations of degeneration.

Mean T_2 relaxation time in the nucleus and annulus did not correlate with the degeneration grades. Published data (Welsh et al. 2011, Takashima et al. 2012) corroborates our results regarding the annulus but contradicts those pertaining to the nucleus. Unlike those studies, our T_2 maps were performed on cadaver specimens. The *in vitro* conditions may have lowered the water and proteoglycan content in the nucleus (Marinelli et al. 2009). Perhaps for the same reason is the nuclear Totsu not related to the degeneration grades. Besides, the nuclear mean T_2 and T_{OTSU} , with only poor connection to the mechanical measurements, are not a satisfactory degeneration criterion.

T_2 is inversely sensitive to the collagen content and orientation of these fibres: regions with denser collagen network as in the annulus are associated with lower T_2 relaxation time

(Perry et al. 2006, Marinelli et al. 2009) while annular tears, induced by the degeneration, come out as a higher local T_2 (Trattnig et al. 2010). These High Intensity Zone (HIZ), inevitably increase the value of the annular T_{OTSU} explaining why it correlated positively and significantly with all 3 grading systems.

Interestingly, annular T_{OTSU} correlates also significantly with torsional and lateral bending stiffnesses but not with the compressive one. Michalek et al. (2010) showed that a loss of pressurization of the nucleus is responsible of alterations of the compressive behaviour of the disc while the behaviour in torsion is influenced by the presence of annular fibre disruptions. As the collagen fibres also drive the mechanical response of the intervertebral disc in flexion, lateral bending and flexion/extension, any annular disruptions decrease the intervertebral stiffness for those loading modes as well (Haughton et al. 2000). Those annular conditions, resulting in a higher T_{OTSU} explain the significant negative correlations obtained between annular T_{OTSU} and the bending or torsional stiffnesses. These findings corroborate previous observations suggesting that the presence of HIZ in the intervertebral disc is associated with reduction of the intervertebral stiffness (Schmidt et al. 1998).

There is no relation between T_{OTSU} in lateral regions of the annulus and lateral loading or between T_{OTSU} in the anterior annulus and flexion/extension. Conversely, T_{OTSU} of the posterior annulus provides interesting results. Not only did it correlate significantly with all the grading schemes but also with all bending stiffnesses, including flexion and extension. This result is coherent with our previous assumption that T_{OTSU} is sensitive to annular disruptions insofar as most HIZ, sometimes associated with low back pain, occurs in the posterior annulus (Peng et al. 2006).

There are limitations to be aware of. Only quasi-static tests were conducted, since the intervertebral compliance is dependent on the loading rate and the hydration of the disc. Nevertheless, various loading rates would only offset the stiffness measurements (vanEngelen et al. 2012). The posterior elements and surrounding soft tissues such as muscles and ligaments that are also responsible for the spinal stability were removed. Human material is difficult to obtain, thus the donors were few and the samples old which might explain why the age of the donors was unrelated to T_2 measurements, stiffness or degeneration grade (Tanaka et al. 2001, Mayerhofer et al. 2012). The specimens were kept frozen. Few freeze-thaw cycles seem not to affect the flexibility of human spinal segments (Gleizes et al. 1998, Tan and Uppuganti 2012) but despite being the standard storage

method, they potentially damage the tissues. Finally, only one axial T_2 maps was acquired in the middle of each disc and some out of plane annular features may have been missed. Most of those limitations are inherent to *in vitro* conditions and cadaver testing but the stiffness measurements should be performed *in vitro* in a controlled environment to be reliable. Moreover, not only countless *in vivo* MRI studies already exist but also the link with mechanical properties, fundamental in the understanding of spinal instability, is rarely considered. For one of the first time, this study highlights the relation between quantitative MRI and stiffness of the intervertebral disc. The low but significant correlations between Otsu threshold, classification schemes and mechanical measures could be improved by performing similar study on fresh animal material but this raises the problem of interspecies comparison as no large animal model for disc degeneration exists (Alini et al. 2008). One last limitation lies in the use of a knee coil for the imaging. Although clinical protocols were performed in this study, a knee coil was used to maximise the signal-to-noise ratio. In conclusion, our study shows that the usual classification schemes cannot be related to the stiffness of cadaveric human intervertebral disc, unlike quantitative T_2 measurements (Otsu threshold) computed in the posterior part of the annulus fibrosus. Although this fully automatic method requires further validation for *in vivo* imaging conditions, its simplicity, minimal human interaction and link with biomechanical properties makes it an attractive candidate for clinical assessment of disc degeneration.

Acknowledgments

The authors thank Alexander Bürki and Marc Laurent for their help regarding the mechanical tests, Urs Röhler for producing the MRI-compatible container, Prof. Mauricio Reyes sharing his expertise in image processing (Institute of Surgical Technology and Biomechanics, University of Bern, Switzerland) and Dr. Michael L. Pretterklieber for providing the specimens (Institute of Anatomy, University of Vienna, Austria). Finally, we also would like to acknowledge Prof. Chris Boesch (Department of Clinical Research, Inselspital, University of Berne, Switzerland) for the interesting discussions regarding MRI and its application to the intervertebral disc imaging. The project was made possible through funding obtained from the European Community, Grant Agreement n° PITN-GA-2009-238690-SPINEFX.

Table A1. Degeneration grades, T2 maps, Mean, Standard deviation, Otsu threshold and Δ ($Mean_{nucleus} - Mean_{annulus}$) computed for the specimens as well as their apparent modulus for each load case. The compressive apparent modulus is in MPa, the apparent modulus in torsion, lateral bending, flexion and extension are expressed in kPa. The data is organised by increasing Thompson grade.

#	Thom.	Benn.	Wata.	Level	Level	Map	Quantitative T ₂ data (ms)												Apparent modulus (Comp.[Mpa], else [kPa])													
							Nucleus			Annulus			Δ		AF Anterior		AF Posterior		AF Left		AF Right		Comp.		Torsion		Bending		Flex.		Ext.	
							Mean	SD	Th.	Mean	SD	Th.	Mean	SD	Th.	Mean	SD	Th.	Mean	SD	Th.	Mean	SD	Th.	Mean	SD	Th.	Mean	SD	Th.		Mean
1	1	0	1	L2-L3	63		83.90	6.79	83	59.36	11.59	58	24.54	59.02	11.16	58	57.58	15.15	55	59.21	8.37	59	61.38	15.15	61	4.71	25.3	20.66	13.57	16.68	7.22	6.86
2	1	1	2	T12-L1	70		60.08	4.67	59	53.42	9.81	54	6.66	48.62	11.06	67	56.81	5.58	55	52.65	5.91	52	56.10	5.58	65	3.33	18.9	17.17	33.3	31.08	3.76	8.63
10	1	0	1	L2-L3	71		85.10	9.43	83	64.73	13.62	63	20.37	59.91	12.94	59	69.12	15.64	60	62.57	10.84	61	68.00	15.64	66	2	1.04	3.93	4.79	8.26	2.33	1.1
5	2	0	1	L4-L5	63		79.85	11.70	78	51.54	9.59	52	28.31	51.00	9.93	53	54.34	11.41	53	53.52	8.26	52	47.95	11.41	37	0.43	3.54	4.47	5	6.71	2.15	0.08
6	2	6	3	L4-L5	68		74.52	7.80	74	64.72	15.84	68	9.80	58.09	10.22	57	74.66	23.93	88	64.75	11.47	68	63.76	23.93	82	2.49	1.82	8.21	7.53	6.8	1.5	1.79
7	2	3	2	L2-L3	68		76.35	7.37	76	62.12	9.32	60	14.22	56.36	8.54	56	71.24	8.14	74	62.54	7.00	61	62.56	8.14	60	1.96	1.25	3.18	1.63	3.08	0.2	1.38
9	2	4	2	T12-L1	71		75.34	6.38	74	54.39	10.60	53	20.95	48.53	9.26	45	60.31	10.61	55	56.28	8.42	57	54.00	10.61	50	0.83	14.79	14.71	22.29	20.55	6.21	4.68
13	2	2	2	T12-L1	89		74.08	9.58	78	56.57	8.90	54	17.51	51.11	9.12	50	60.59	6.42	57	60.17	9.05	57	57.47	6.42	57	0.12	19.83	18.5	24.07	24.31	5.65	6.77
4	3	12	3	L4-L5	70		74.42	11.27	73	62.12	11.61	63	12.30	56.74	8.47	53	70.48	7.95	72	66.34	12.87	71	57.21	7.95	55	1.21	2.81	5.34	12.3	9.42	1.45	1.31
8	3	9	3	T12-L1	68		66.76	5.57	66	63.12	9.24	65	3.64	61.86	8.41	63	63.39	10.47	60	64.68	10.88	68	63.22	10.47	64	1.45	0.84	2.92	9.21	11.77	7.43	9.75
11	3	8	3	L4-L5	71		82.69	9.51	82	87.44	19.73	82	-4.75	89.75	29.77	86	89.05	15.67	78	84.09	9.07	82	86.21	15.67	78	0.47	0.79	1.16	1.88	4.03	0.48	0.25
12	3	9	3	L4-L5	89		130.65	45.55	103	75.53	20.60	78	55.12	72.46	26.66	76	84.56	14.53	86	83.53	19.74	82	74.44	14.53	74	1.94	0.46	1.53	3.54	5.13	1.74	0.22
14	3	15	4	L2-L3	87		72.43	9.95	74	72.30	15.33	76	0.13	71.81	13.69	75	71.02	11.76	72	82.63	17.63	81	61.78	11.76	60	0.52	2.35	2.73	5.39	7.4	2.96	2.05
3	4	14	4	L2-L3	70		61.48	5.88	61	60.32	26.38	72	1.16	63.10	26.65	40	64.92	26.62	82	57.11	22.34	39	55.47	26.62	80	0.91	1.97	2.49	1.03	2.7	0.11	0.99

References

- Alini M., Stephen M. Eisenstein S.M, Ito K., Little C., Kettler A.A., Masuda K., Melrose J., Ralphs J., Stokes I., Wilke H.J. 2008. Are animal models useful for studying human disc disorders / degeneration? *Eur Spine J.* 17:2–19
- Baron P., Deckers R., Sprinkhuizen S. M., Merckel L. G., Bleys R. L., Bakker C. J., and Bartels L. W. L. 2011. Measurement of the T1 and T2 temperature dependence of human breast adipose tissue. *Proc. Intl. Soc. Mag. Reson. Med.* 19
- Beckstein J.C., Sen S., Schaer T.P., Vresilovic E.J. and Elliott D.M. 2008. Comparison of animal discs used in disc research to human lumbar disc axial compression mechanics and glycosaminoglycan content. *Spine.* 33:E166–E173
- Benneker L.M., Heini P.F., Anderson S.E., Alini M., Ito K. 2005. Correlation of radiographic and MRI parameters to morphological and biochemical assessment of intervertebral disc degeneration. *Eur Spine J.* 14: 27–35
- Campana S., de Guise J.A., Rillardon L., Mitton D., Skalli W. 2007. Lumbar intervertebral disc mobility: effect of disc degradation and of geometry. *Eur J Orthop Surg Traumatol (2007)* 17:533–541
- Chevrefils C., Cheriet F., Aubin C., and Grimard G. 2009. Texture Analysis for Automatic Segmentation of Intervertebral Disks of Scoliotic Spines From MR Images. *IEEE Transactions On Information Technology In Biomedicine*, 13(4)
- Dolan P. and Adams M.A. 2001. Recent advances in lumbar spinal mechanics and their significance for modelling. *Clin Biomech.* 16-Suppl 1:S8-S16
- Elliott D.M. and Sarver J.J. 2004. Young investigator award winner: validation of the mouse and rat disc as mechanical models of the human lumbar disc. *Spine.* 29:713–722
- Gédet P., Thistlethwaite P.A. and Ferguson S.J. 2007. Minimizing errors during in vitro testing of multisegmental spine specimens: considerations for component selection and kinematic measurement. *J Biomech.* 40:1881-1885
- Gédet P., Thistlethwaite P.A. and Ferguson S.J. 2009. Comparative biomechanical investigation of a modular dynamic lumbar stabilization system and the Dynesys system. *Eur Spine J.* 18:1504-1511
- Gleizes V., Viguier E., Feron J.M., Canivet S. and Lavaste F. 1998. Effects of freezing on the biomechanics of the intervertebral disc. *Surg Radiol Anat.* 20:403-407
- Gold G.E., Han E., Stainsby J., Wright G., Brittain J., Beaulieu C. 2004. Musculoskeletal MRI at 3.0 T: Relaxation Times and Image Contrast. *AJR.* 183:343–351
- Haughton V.M., Lim T.H. and An H.S. 1999. Intervertebral disk appearance correlated with stiffness of lumbar spinal motion segments. *AJNR Am J Neuroradiol.* 20:1161-1165
- Haughton V.M., Schmidt T.A., Keele K., An H.S. and Lim T.H., Ph.D. 2000. Flexibility of lumbar spinal motion segments correlated to type of tears in the annulus fibrosus. *J Neurosurg.* 92:81–86
- Hoppe S., Quirbach S., Mamisch T.C., Krause F.G., Werlen S. and Benneker L.M. 2012. Axial T2* mapping in intervertebral discs: a new technique for assessment of intervertebral disc degeneration. *Eur Radiol.* 22:2013–2019
- Julkunen P., Korhonen R.K., Nissi M.J. and Jurvelin J.S. 2008. Mechanical characterization of articular cartilage by combining magnetic resonance imaging and finite-element analysis-a potential functional imaging technique. *Phys. Med. Biol.* 53:2425–2438

- Kettler A., Rohlmann F., Ring C., Mack C. and Wilke H.J. 2011. Do early stages of lumbar intervertebral disc degeneration really cause instability? Evaluation of an in vitro database. *Eur Spine J.* 20:578–584
- Kirkaldy-Willis W.H. and Farfan H.F. 1982. Instability of the lumbar spine. *Clin Orthop Relat Res.* 165:110–123
- Krismer M., Haid C., Behensky H., Kapfinger P., Landauer F. and Rachbauer F. 2000. Motion in lumbar functional spine units during side bending and axial rotation moments depending on the degree of Degeneration. *Spine.* 25:2020-2027
- Kurkijarvi J.E., Nissi M.J., Kiviranta I., Jurvelin J.S. and Nieminen M.T. 2004. Delayed Gadolinium-Enhanced MRI of Cartilage (dGEMRIC) and T2 Characteristics of Human Knee Articular Cartilage: Topographical Variation and Relationships to Mechanical Properties. *Magnetic Resonance in Medicine.* 52:41-46
- Mayerhofer M.E., Stelzeneder D., Bachbauer W., Welsch G.H, Mamisch T.C., Szczypinski P., Weber M., Peters N., Fruehwald-Pallamar J., Puchner S. and Siegfried Trattng. 2012. Quantitative analysis of lumbar intervertebral disc abnormalities at 3.0 Tesla: value of T2 texture features and geometric parameters. *NMR Biomed.* 25: 866–872
- Marinelli N.L, Houghton V.M., Munoz A. and Anderson P.A. 2009. T2 Relaxation Times of Intervertebral Disc Tissue Correlated With Water Content and Proteoglycan Content. *Spine.* 34(5):520 –524
- Michalek A.J., Funabashi K.L. and Iatridis J.C. 2010. Needle puncture injury of the rat intervertebral disc affects torsional and compressive biomechanics differently. *EurSpineJ.* 19:2110–2116
- Michopoulou S., Costaridou L., Panagiotopoulos E., Speller R., Todd-Pokropek A. 2008. Segmenting degenerated lumbar intervertebral discs from MR images. *IEEE Nuclear Science Symposium Conference Record.*
- Michopoulou S.K., Costaridou L., Panagiotopoulos E., Speller R., Panayiotakis G., and Todd-Pokropek A. Atlas-Based Segmentation of Degenerated Lumbar Intervertebral Discs From MR Images of the Spine. *IEEE transactions on biomedical engineering,* 56(9).
- Mwale F., Iatridis J.C., Antoniou J. 2008. Quantitative MRI as a diagnostic tool of intervertebral disc matrix composition and integrity. *EurSpineJ.* 17(4):S432–S440
- Nieminen M.T., Rieppo J., Toyras J., Hakumaki J.M., Silvennoinen J., Hyttinen M.M., Helminen H.J and Jurvelin J.S. 2001. T2 Relaxation Reveals Spatial Collagen Architecture in Articular Cartilage: A Comparative Quantitative MRI and Polarized Light Microscopic Study. *Magnetic Resonance in Medicine.* 46:487-493
- Nissi M.J., Rieppo J., Toyras J., Laasanen M.S., Kiviranta I., Nieminen M.T. and Jurvelin J.S. 2007. Estimation of mechanical properties of articular cartilage with MRI e dGEMRIC, T2 and T1 imaging in different species with variable stages of maturation. *OsteoArthritis and Cartilage.* 15:1141-1148
- Otsu N. 1979. A Threshold Selection Method From Gray-Level Histograms. *EEE Transactions On Systems, Man, And Cybernetics,* 9(1)
- Panjabi M. 2003. Clinical spinal instability and low back pain. *Journal of Electromyography and Kinesiology.* 13:371–379
- Peng B., Hou S., Wu W., Zhang C., Yang Y. 2006. The pathogenesis and clinical significance of a high-intensity zone (HIZ) of lumbar intervertebral disc on MR imaging in the patient with discogenic low back pain. *Eur Spine J.* 15: 583–587

- Perry J., Haughton V.M., Anderson P.A., Wu Y., Fine J., Mistretta C. 2006. The Value of T2 Relaxation Times to Characterize Lumbar Intervertebral Disks: Preliminary Results. *AJNR Am J Neuroradiol.* 27:337–342
- Polikeit A., Ferguson S.J., Nolte L.P., Orr T.E. 2003. Factors influencing stresses in the lumbar spine after the insertion of intervertebral cages: finite element analysis. *Eur Spine J.* 12:413–420
- Schmidt T.A., An H.S., Lim, T.H., Nowicki. B.H. and Haughton V.M. 1998. The stiffness of lumbar spinal motion segments with a high-intensity zone in the annulus fibrosus. *Spine.* 23:2167–2173
- Showalter B.L., Beckstein J.C., Martin J.T., Beattie E.E., Espinoza Orías A.A., Schaer T.P., Vresilovic E.J. and Elliott D.M. 2012. Comparison of animal discs used in disc research to human lumbar disc. *Spine.* 7:E900–E907
- Smit T. H., van Tunen M.S.L.M., van der Veen A.J., Kingma I., van Dieën J.H. 2011. Quantifying intervertebral disc mechanics: a new definition of the neutral zone. *BMC Musculoskeletal Disorders.* 12:38
- Smit T., Odgaard A., Schneider E. 1997. Structure and function of vertebral trabecular bone. *Spine* 22:2823–2833
- Stelzeneder D., Welsch G.H., Kovács B.K., Goed S., Paternostro-Sluga T., Vlychou M., Friedrich K., Mamisch T.C. and Trattnig S. 2012. Quantitative T2 evaluation at 3.0 T compared to morphological grading of the lumbar intervertebral disc: A standardized evaluation approach in patients with low back pain. *European Journal of Radiology.* 81:324–330
- Stokes I.A., Frymoyer J.W. 1987. Segmental motion and instability. *Spine.* 12:688–691
- Takashima H., Takebayashi T., Yoshimoto M., Terashima Y., Tsuda H., Ida K. and Yamashita T. 2012. Correlation between T2 relaxation time and intervertebraldisk degeneration. *Skeletal Radiol.* 41:163–167
- Tan J.S. and Uppuganti S. 2012. Cumulative Multiple Freeze-Thaw Cycles and Testing Does Not Affect Subsequent Within-Day Variation in Intervertebral Flexibility of Human Cadaveric Lumbosacral Spine. *Spine.* 37:E1238–E1242
- Tanaka N., An H.S., Lim T., Fujiwara A., Jeon C., Haughton V.M. 2001. The relationship between disc degeneration and flexibility of the lumbar spine. *The Spine Journal.* 1:47–56
- Thompson JP, Pearce RH, Schechter MT, Adams ME, Tsang IK, Bishop PB. 1990. Preliminary evaluation of a scheme for grading the gross morphology of the human intervertebral disc. *Spine* 15:411–415
- Trattnig S., Stelzeneder D., Goed S., Reissegger M., Mamisch T.C., Paternostro-Sluga T., Weber M., Szomolanyi P., Welsch G.H. 2010. Lumbar intervertebral disc abnormalities: comparison of quantitative T2 mapping with conventional MR at 3.0T. *Eur Radiol.* 20:2715–2722
- Van Engelen S.J.P.M., Ellenbroek M.H.M., van Royen B.J., de Boer A., van Dieën J.H. 2012. Validation of vibration testing for the assessment of the mechanical properties of human lumbar motion segments. *JBiomech.* 45:1753–1758
- Van Rossum G. and de Boer J. 1991. Interactively testing remote servers using the python programming language. *CWI Q.* 4:283–303
- Watanabe A., Benneker L.M., Boesch C., Watanabe T., Obata T., Anderson S.E. 2007. Classification of Intervertebral Disk Degeneration with Axial T2 Mapping. *AJR.* 189:936–942

- Welsch G.H, Trattnig S., Paternostro-Sluga T., Bohndorf K., Goed S., Stelzeneder D., Mamisch T.C. 2011. Parametric T2 and T2* mapping techniques to visualize intervertebral disc degeneration in patients with low back pain: initial results on the clinical use of 3.0 Tesla MRI. *Skeletal Radiol.* 40:543–551
- Yushkevich P.A., Piven J., Hazlett H.C., Smith R.G., Ho S., Gee J.C. and Gerig G. 2006. User-guided 3D active contour segmentation of anatomical structures: Significantly improved efficiency and reliability. *NeuroImage.* 31:1116 – 1128

Chapter 6: Conclusions

1. Discussions and limitations

This study not only highlighted the lack of realism of the standard rigid boundary conditions usually applied but also proposes new strategies for the non-invasive evaluation of the biomechanical status of the intervertebral disc via MRI, the first steps towards subject-specific boundary conditions for the finite elements analyses. The combined use of the CT-based models of vertebral bodies and MRI-based models of intervertebral discs could improve the predictions of vertebral strength.

Chapter 2: The influence of the endplate on vertebral strength

In mechanical testing and QCT voxel models of the human vertebrae, the usual procedure consists in embedding the vertebral body in stiff polymer (PMMA). Therefore, concerns were raised about the few tests conducted on vertebral sections and the hypothetical lack of realism of such boundary condition. Actually, not only the ultimate forces (ie. vertebral strength) computed with vertebral sections or embedded endplates are equivalent but also the evolution and distributions of damage, especially when the vertebral sections were fully constrained. Thus, the damage mechanism with PMMA and sections are equivalent. The removal of endplates may not be physiologic but it is as realistic as a rigid embedding.

Limitations:

- 1) The *in vitro* CT used do not present noise and artefacts due to soft tissues.
- 2) We do not account for the preexisting damage present in osteoporotic bone.
- 3) The cortex and trabecular structure could not be distinguished at low resolution.

Chapter 3: The influence of intervertebral disc degeneration on vertebral strength

Computationally expensive linear elastic μ FE models were used to study the behaviour of the osteoporotic vertebral body during compressive loading but neither ultimate force nor damage distributions were computed with healthy intervertebral or PMMA boundary condition, which resembles a highly degenerated disc. The smooth models with HRpQCT-based cortex thickness and trabecular fabric provided clear results: an embedded vertebra is more brittle and shows higher ultimate force compared to a vertebral body loaded via

intervertebral discs. Indeed, the damage initiates progressively long before the failure of the vertebral body in the endplate regions under the healthy nucleus while most of the damage is quickly induced at failure load in the cortical regions of an embedded vertebral body. In conclusion, as *in vivo* studies report, an osteoporotic vertebral body is subjected to a lesser risk of fracture when surrounded by degenerated discs.

Limitations:

- 1) The preexisting osteoporotic microdamage was again not taken in account.
- 2) Only uniaxial compression was tested although other load cases (flexion+compression) could be more adequate.
- 3) The intervertebral disc model was idealistic in terms of geometry and material properties.

Chapter 4: Normalisation of intervertebral disc compliances

No standard normalisation protocol is available for the stiffness measured on compression, torsion, lateral bending and flexion-extension tests. This is surprising considering the large discrepancies due to the specimen variability, making inter-specimen comparisons challenging. Thus, cross-sectional (CSA) area, polar moment of inertia (J) or area moments of inertia (I_{xx} , I_{yy}) and height (H) were computed from MRI data for all specimens and *in silico* and *in vitro* tests were performed. First, the simulations on discs with identical material properties but various dimensions, confirms the influence of the geometry on the disc's mechanics, a stiffer response was obtained for every biomechanical tests on disc with a larger CSA, J, I_{xx} or I_{yy} or a smaller H. The normalisation with respect to H, CSA, J, I_{xx} and I_{yy} attenuated but did not suppress the effect of geometry as non-linearity also occurs. Then, even after normalisation, the experimental stiffnesses calculated presented large standard deviations, probably amplified by diverse degrees of degeneration within our set of samples. All but compressive stiffnesses correlated highlighting different mechanisms in compression mainly affected by the nucleus condition and torsion and bending, influenced by the state of the annulus' collagen fibres. Such a normalisation protocol is useful for inter-species, inter-individual and inter-level stiffness comparison of intervertebral discs and necessary when relating its mechanical properties to the degree of degeneration.

Limitations & perspectives:

- 1) Although the intervertebral compliance is dependent on the loading rate and the hydration of the disc, only quasi-static tests were conducted.
- 2) A full normalisation of the stiffness, suppressing the material non-linearity, would be possible via reliable specimen-specific IVD models.

Chapter 5: An MRI-based methodology for biomechanical evaluation of degenerated intervertebral discs

The quantification of T_2 relaxation time is related to the biochemical properties of the intervertebral disc giving the advanced MRI methods the potential to evaluate objectively the disc degeneration. Although compressive Young modulus of the human articular cartilage is connected to its mean T_2 relaxation time, such connection was not yet established for intervertebral disc. Thus, MRI data (axial, coronal, sagittal T_1 and T_2 weighted and axial T_2 map) was used to: determine the cross-sectional area (CSA), polar moment of inertia (J) or area moments of inertia (I_{xx} , I_{yy}) and height (H) for the normalisation of stiffness from compression, torsion, lateral bending and flexion-extension tests, evaluate the degeneration of our samples by using the Thompson, Benneker and Watanabe classifications and compute the mean T_2 and the Otsu threshold (T_{OTSU}) in different regions of the discs. Mean T_2 relaxation time in the nucleus and annulus and the stiffnesses did not correlate with the degeneration grades unlike T_{OTSU} computed in the posterior annulus that was also linked to torsional and lateral bending. T_{OTSU} is a histogram-based segmentation method that computes the optimal threshold that maximizes the separability of two classes of values. Tears, mostly found in the posterior annulus, are responsible for stiffness loss and high intensity zones detected by the method, explaining the positive correlation between T_{OTSU} and the rotational and bending stiffnesses. In conclusion, the usual classification schemes cannot be related to the stiffness of cadaveric human intervertebral disc, unlike quantitative T_2 measurements (Otsu threshold) computed automatically in the posterior part of the annulus fibrosus.

Limitations:

- 1) We must also report some limitations related to the quasi-static tests conducted on the specimens.

- 2) Only one axial T_2 maps was acquired in the middle of each disc and some annular features may have been missed.

2. Outlooks

If finite element analysis in biomedical engineering is going towards patient-specific modelling but as suggested throughout this thesis, a number of crucial steps are still to be taken.

2.1 MRI-based intervertebral disc model

Our work only provided but an insight on how the mechanical properties of the intervertebral disc could be related to quantitative MRI data. Hence, the non-invasive evaluation of the biomechanical status of the IVD still needs improvements. Low but significant correlations between Otsu threshold, classification schemes and mechanical measures were found in **Chapter 5**. We believe that those correlations could be improved by performing similar study on fresh material considering the possible defects induced by cycles of freezing-thawing. One issue lies in the difficulties to obtain human material. Of course, numerous studies use animal material but as long as no large animal model for disc degeneration, this raises the problem of interspecies comparison.

In a future work, one might want to calibrate the material parameters of the disc constitutive law used in **Chapter 3 and 4** using the quantitative MRI data, following an approach similar to what is currently done between the bone material properties and the CT images. A first step would be a disc model able to simulate the experimental tests in compression, bending, flexion-extension and torsion to replicate completely the mechanical behaviour of the specimen *in silico*. Unfortunately, our current disc material model is still too complex but the creation of a simpler constitutive model still able to fit accurately the experimental load-deflection curves would be more suitable for an efficient optimisation.

In **Chapter 5**, we suggest that the heterogeneity of the quantitative MRI and High Intensity Zones, measured by Otsu threshold, might reflect the presence of tears. Those tears are primarily defects of the annular collagen fibres. Therefore, a second step would be to relate the Otsu threshold to the fibres material parameters introduced in **Chapter 2**, namely the angle of the fibre with regards to the transverse plane (ϕ), the stiffness of the fibres (K_1) and the density of fibres (K_2).

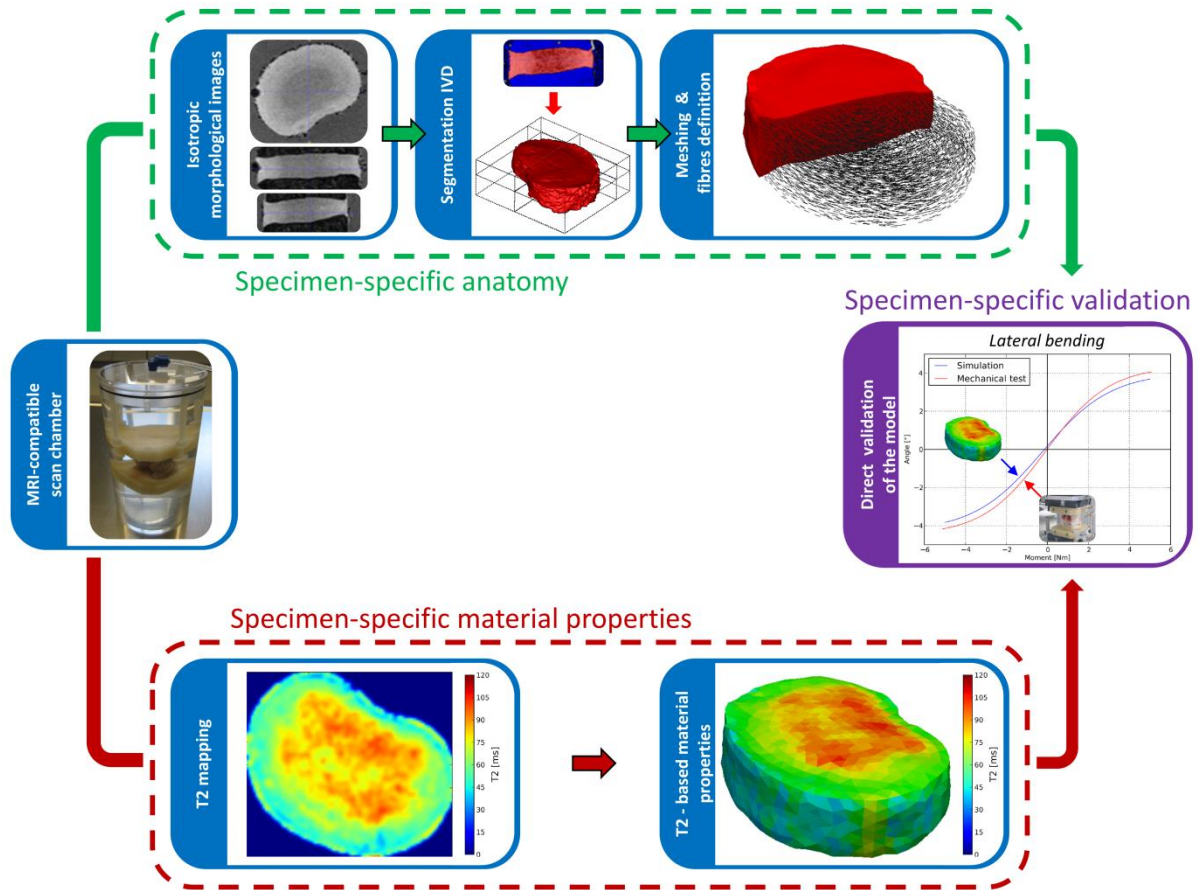


Fig. 1. The framework for a fully subject-specific model of the intervertebral disc.

2.2 Patient-specific loading on the vertebral body model

In a perfect world where the patient would be scanned by high resolution CT and MRI, fully specimen-specific models of the vertebral body and intervertebral discs could be used for the diagnosis of disc degeneration or the prediction of vertebral strength for realistic boundary conditions and daily activities.

While the current state-of-the-art of FE models did not reach such degree of personalisation, the time spent for the diagnosis and radiation doses received by the patient would still be too important. However, the load cases applied on the models of **Chapter 2 and 3** are a key point of the vertebral strength prediction that can be improved today. Usually, the tests conducted in experiments such as axial compression, flexion, torsion, lateral bending or even coupled motions are simulated with the FE models but they do not represent adequately the type of loading that the spine is undergoing during the day.

One solution lies in the direct use of the patient's kinematics determined from fast and low-radiation imaging techniques such as Dual Fluoroscopy Imaging suggested by Wang et al. 2012 or the EOS system.

Another possibility which is increasingly considered is the application to the FEA of realistic boundary conditions and loadings computed from Invert dynamic analysis software. The musculoskeletal simulation software Anybody Modelling System (AMS) is able to compute muscle forces from motion capture driven rigid-body simulations. Moreover, the possibility to provide AMS with patient's data such as height or weight and the use of the patient's bone geometry enhance the personalisation of the calculated muscles, tendons and ligaments forces. Coupling the AMS and FE models is another step towards more realism (Wagner et al. 2010, Grujicic et al. 2010, Böhme et al. 2012).

References

- Böhme J., Shim V., Höch A., Mütze M., Müller C., Josten C. 2012. Clinical implementation of finite element models in pelvic ring surgery for prediction of implant behavior: A case report. *Clinical Biomechanics*. 27. 872–878
- Grujicic M, Arakere G, Xie X, LaBerge M, Grujicic A, Wagner D, Vallejo A (2010) Design-optimization and material selection for a femoral-fracture fixation-plate implant. *Materials and Design* 31: 3463–3473
- Wagner D, Divringi K, Ozcan C, Grujicic M, Pandurangan B and Grujicic A (2010) Combined musculoskeletal dynamics/structural finite element analysis of femur physiological loads during walking. *Multidiscipline Modeling in Materials and Structures*. 6 (4): 417-437
- Wang S., Park W.M., Gadikota H.R., Miao J., Kim Y.H., Kirkham B. Wood & Li G. 2012. A combined numerical and experimental technique for estimation of the forces and moments in the lumbar intervertebral disc. *Computer Methods in Biomechanics and Biomedical Engineering*. iFirst

Appendix: From Anybody to Abaqus

From the internal report

Application of realistic boundary conditions computed from Invert dynamic analysis to a finite element model: stress distribution in a human lumbar vertebra during gait.

G. Maquer^a and P. Galibarov^b

^a Institute for Surgical Technology & Biomechanics, University of Bern, Switzerland

^b AnyBody Technology, Aalborg University, Denmark

Since the coupling AMS-FE is fully available in the latest version of AMS, a preliminary feasibility study was conducted with Dr. Pavel Galibarov (consultant Anybody: patient-specific modelling of the lumbar spine, degenerated spine kinematics and development of interfaces to FE packages ANSYS and Abaqus).

Written in: January 2012

1. Introduction

Characterized by low bone mineral density (BMD) and degradation in bone structure, osteoporosis is a major clinical issue (Kanis 2006). Dual energy X-ray Absorptiometry (DXA) is mainly used for non-invasive fracture prediction by measuring areal BMD (Griffith and Genant 2008), but the geometry and local variation in bone density are not taken in account in the measurements. Over the last years, a number of finite element (FE) models based on CT images were developed and homogenized HRpQCT-based FE models with smooth geometry (82 μm) have been validated with experimental tests of human vertebral bodies (Pahr et al. 2010). The models compute vertebral structural properties such as compressive ultimate load and provide a better fracture risk prediction than densitometric methods (Crawford et al. 2003, Buckley et al. 2007, Chevalier et al. 2008, Dall'Ara et al. 2011). However, unrealistic situation could be simulated and the strain localization mechanism could be altered by the boundary conditions (Dall'Ara et al. 2010).

Indeed, even if material modelling and meshes are getting increasingly accurate and patient-specific, the loading conditions are simplistic while realistic boundary conditions are essential to get reliable outcomes from finite element models. A first step is to load the vertebra through intervertebral discs. Moreover, the musculoskeletal simulation software Anybody Modeling System (AMS) is able to compute muscle forces from motion capture driven rigid-body simulations. Hence, coupling the AMS and FE models is another step towards more realism (Wagner et al. 2010, Grujicic et al. 2010).

Therefore, the aim of this study is to introduce a procedure to define loading conditions on a FE model from forces and moments computed in the AMS. The method is used to analyse stress distribution in a QCT-based finite element of a vertebra during walking.

2. Materials and methods

2.1 Vertebral body model

A L2 vertebral body model was generated following the methods introduced in a previous study (Maquer et al. 2012 – **Chapter 3**) with CT-based cortical thickness and trabecular fabric was chosen. This vertebral body is surrounded by hyperelastic intervertebral discs.

Two types of material were tested for the discs either with collagen fibres distributed circumferentially in the annulus fibrosus ($IVD_{\text{anisotropic}}$) or without fibres ($IVD_{\text{isotropic}}$).

2.2 Personalisation of the AMS model

Muscular, ligamentous, and joint reaction forces can be computed by performing an inverse dynamics analysis task on an individualized model in AnyBody Modelling System (AMS - AnyBody Technology A/S, Aalborg, Denmark). An AMS model was constructed based on a standard example, GaitFullBody, of the AnyBody Managed Model Repository (version 1.3) featuring 3 element hill-type muscles. This detailed model of the human including a large number of muscles, ligaments, and other anatomic structures was anthropometrically scaled to fit dimensions of a subject. Yet, an additional level of personalisation could be reached by including the subject's bone morphology. The CT-based geometry of the lumbar vertebral body L2 was reconstructed in Mimics (Materialize, Leuven, Belgium), imported in AMS and a set of landmarks was chosen on its endplates (centre of the endplate, anteroposterior and mediolateral diameters). Similar set of landmarks was selected on the generic AnyBody vertebra geometry and both sets were utilized to define an affine transform in a least-squares manner, in order to morph the source geometry into the subject's geometry. Such morphing was required for the automated scaling of the muscles and ligaments attachment nodes on the vertebral mesh.

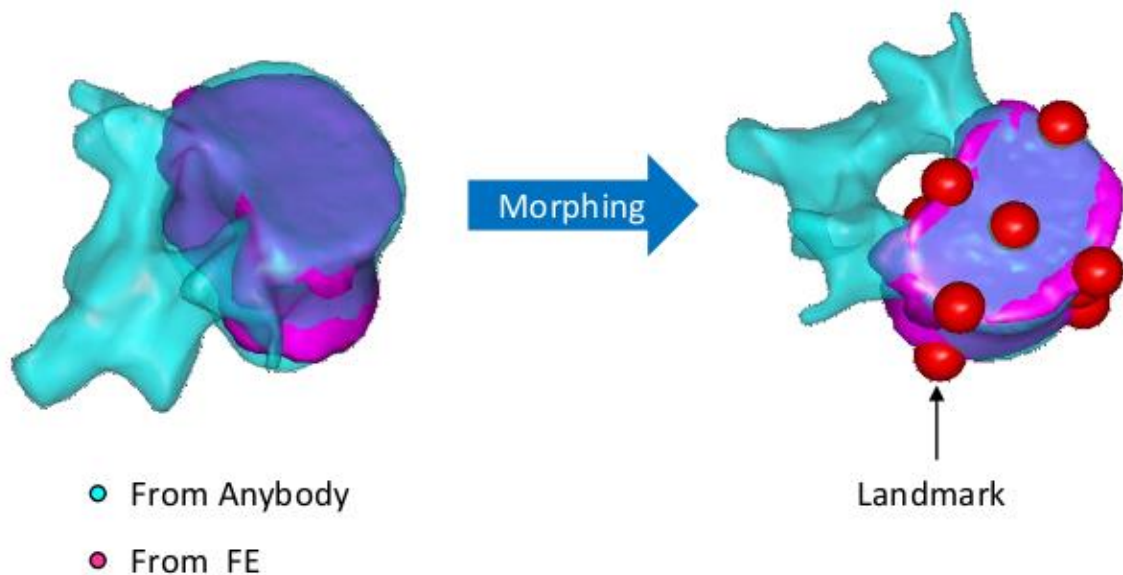


Fig. 1. Morphing of AMS vertebral geometry

The kinematics of the subject's gait were recorded and his motion capture data (a C3D file) was used to drive the AMS model via a set of landmarks on each segment coupled to the corresponding motion capture marker.

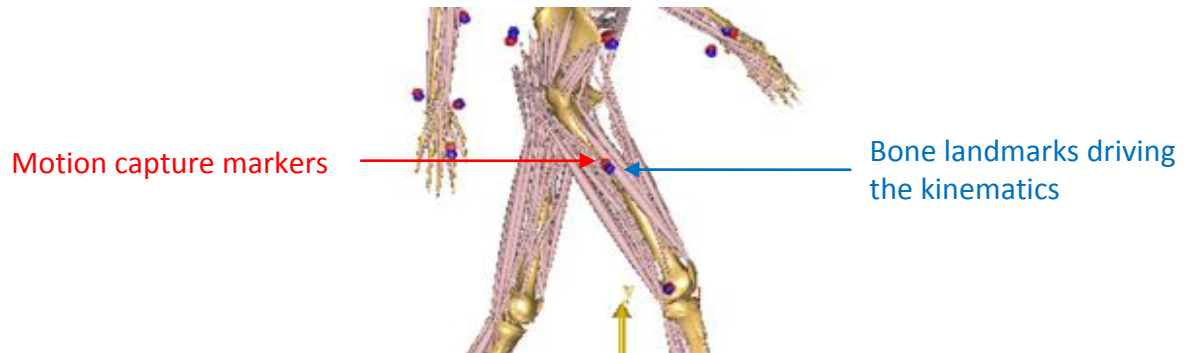


Fig. 2. Motion capture driven kinematics

2.3 Combining musculoskeletal and finite element models

A gait analysis was performed in AMS, muscular and joint reaction forces were computed and extracted to be assigned as loading conditions to the FE model by means of the AnyFE2Abq tool (AnyBody Technology A/S, Aalborg, Denmark). This automated tool extract forces from AMS output file, creates muscle and joints attachments nodes on the mesh and generates evenly distributed rigid constraints (see *COUPLING keyword) between those newly defined nodes and patches of the bone surface with minimal user's interaction. The exported forces are applied to the newly created nodes as concentrated forces (*CLOAD keyword).

The outcome of AnyFE2Abq is an Abaqus input file that can be directly included in the input file describing the FE model. Time dependant amplitudes were automatically created to change the forces/moments according to the gait cycle period. However, results of this procedure had to be revised as the posterior part of the vertebra was missing. Therefore, for all muscle with posteriorly located muscle, attachment nodes were constrained to the pedicle cut surfaces. Similarly, the L1L2 and L2L3 joint loads (analogue of intervertebral disc pressure) were applied to the endplates of adjacent vertebrae accordingly. Forces applied to the model were in equilibrium but density (*DENSITY) properties were set for the model and *INERTIA RELIEF option was used to avoid rigid body motion without constraining the

mesh. Fig.3 demonstrates the created loading conditions and rigid constraints used for the finite element analysis.

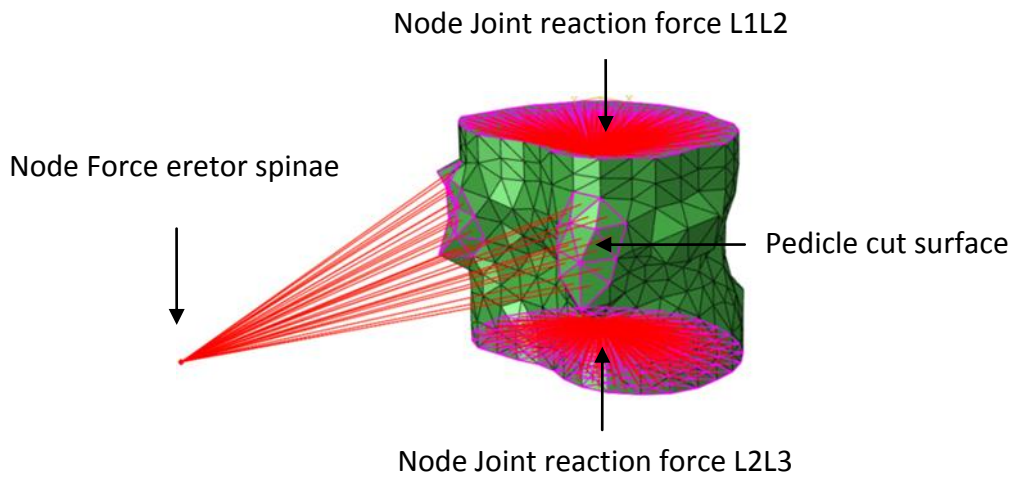


Fig.3. Kinematic coupling between the node of application of the force and the loaded surfaces

2.4 Finite element simulations

The forces computed by AMS were applied to the vertebral body model and 2 simulations were conducted with $IVD_{isotropic}$ and $IVD_{anisotropic}$. Von Mises Stresses were computed for both simulations at 6 characteristic positions of the gait analysis in trabecular core, cortical endplates and cortical wall.

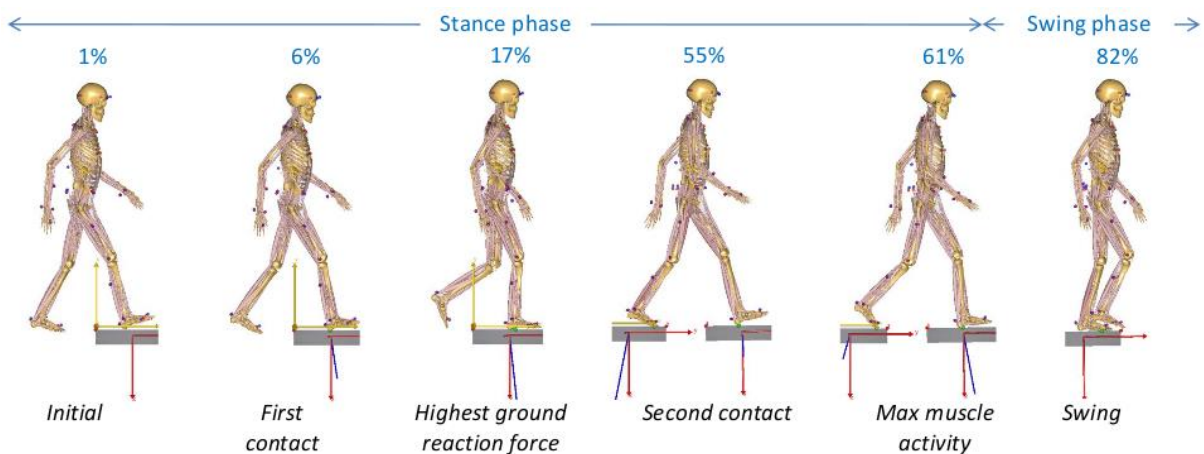


Fig. 4. Simulated gait in AMS. First contact is the moment when the first foot is reaching the ground, second contact when the second foot is touching the floor.

3. Results

Stresses were extracted for the chosen positions and compared. Fig. 5. shows the typical stress distribution in the vertebral bodies. Both simulations resulted in similar stress distribution in the vertebral body. The highest stress level was found in the posterior and lateral cortical walls. A high stress area was observed on the endplates under the nucleus in both cases ($IVD_{\text{isotropic}}$ and $IVD_{\text{anisotropic}}$). The trabecular bone showed similar pattern on the cranial and caudal transverse cross-sections with area of higher stress under the nucleus. The cranial and caudal cross-sections displayed also a higher stress level than the mid transverse cross-section.

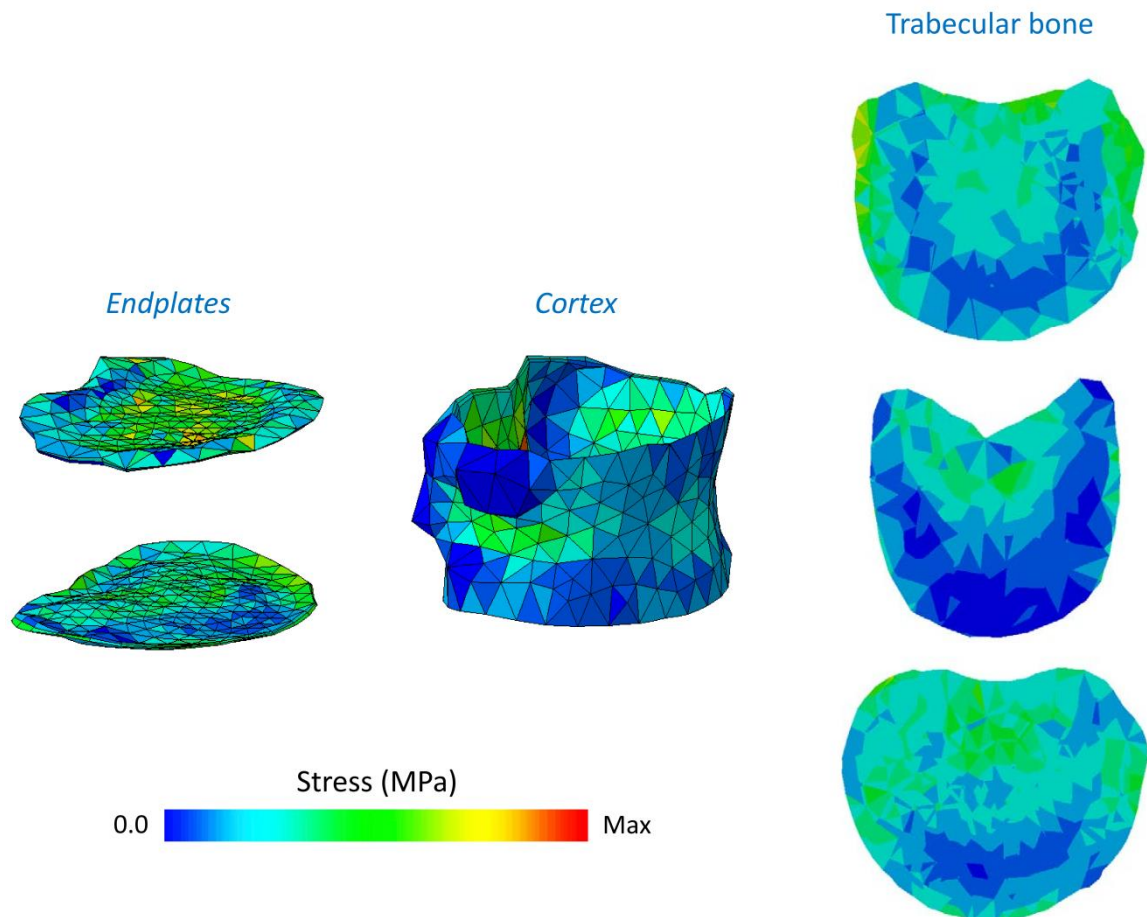


Fig. 5. Example of Von Mises Stress distribution in endplates, cortex and trabecular bone (top, middle, bottom cuts) for isotropic IVD at "Second contact". The stress is plotted in MPa with a Max value depending on the element set of interest: MAX STRESS ENDPLATES = 5.221 MPa, MAX STRESS CORTEX = 12.819 MPa and MAX STRESS TRAB = 1.465 MPa

No significant differences were observed between stress distributions when the vertebral body was loaded via isotropic IVD or anisotropic IVD. Moreover, the stress barplots for each bone area were similar, differing only slightly by the intensity of the von Mises stress.

Fig. 6. compares the maximum value of von Mises stress reached in the vertebra loaded via isotropic and anisotropic IVD for each position in the gait. Stress in cortex was highest and stress in the trabecular bone the lowest for each stage of gait no matter which IVD was used for the computation. For all three element sets, peak of stresses were computed whenever a contact foot-ground occurred. Even if the differences due to various intervertebral disc models were not significant, a trend could be observed: $IVD_{anisotropic}$ seems to induce slightly higher stress in the endplates but lower stress in the cortical and trabecular bone than $IVD_{isotropic}$.

4. Discussion

The main goal of this study was to provide a user case to the newly developed interface between AMS and Abaqus, AnyFE2Abq.exe. A tutorial can be found on Anybody website:

http://www.anybodytech.com/fileadmin/AnyBody/Docs/Tutorials/chap8_Finite_element_analysis/intro.html

The example given was to analyse the von Mises stress distribution in a finite element model of vertebra under muscle forces computed from musculoskeletal analysis. Two simulations were performed using Abaqus with isotropic and anisotropic intervertebral discs and stresses were evaluated for 6 stages of a motion capture driven gait. The geometry of the vertebra implemented in AMS and the muscle insertion points were morphed to match the QCT-based geometry of the vertebra.

The stress distribution in the vertebral body tested can be compared to a FE study carried out by Homminga et al. 2001 who found a higher portion of the total load in the trabecular bone near the endplates. Higher stresses under the nucleus and in the cortex were also seen in this study. However, those data were computed for axial compression and not a gait. The collagen fibres did not seem to have a major impact on the stress distributions probably because the spine undergoes minimal flexion and bending during the gait.

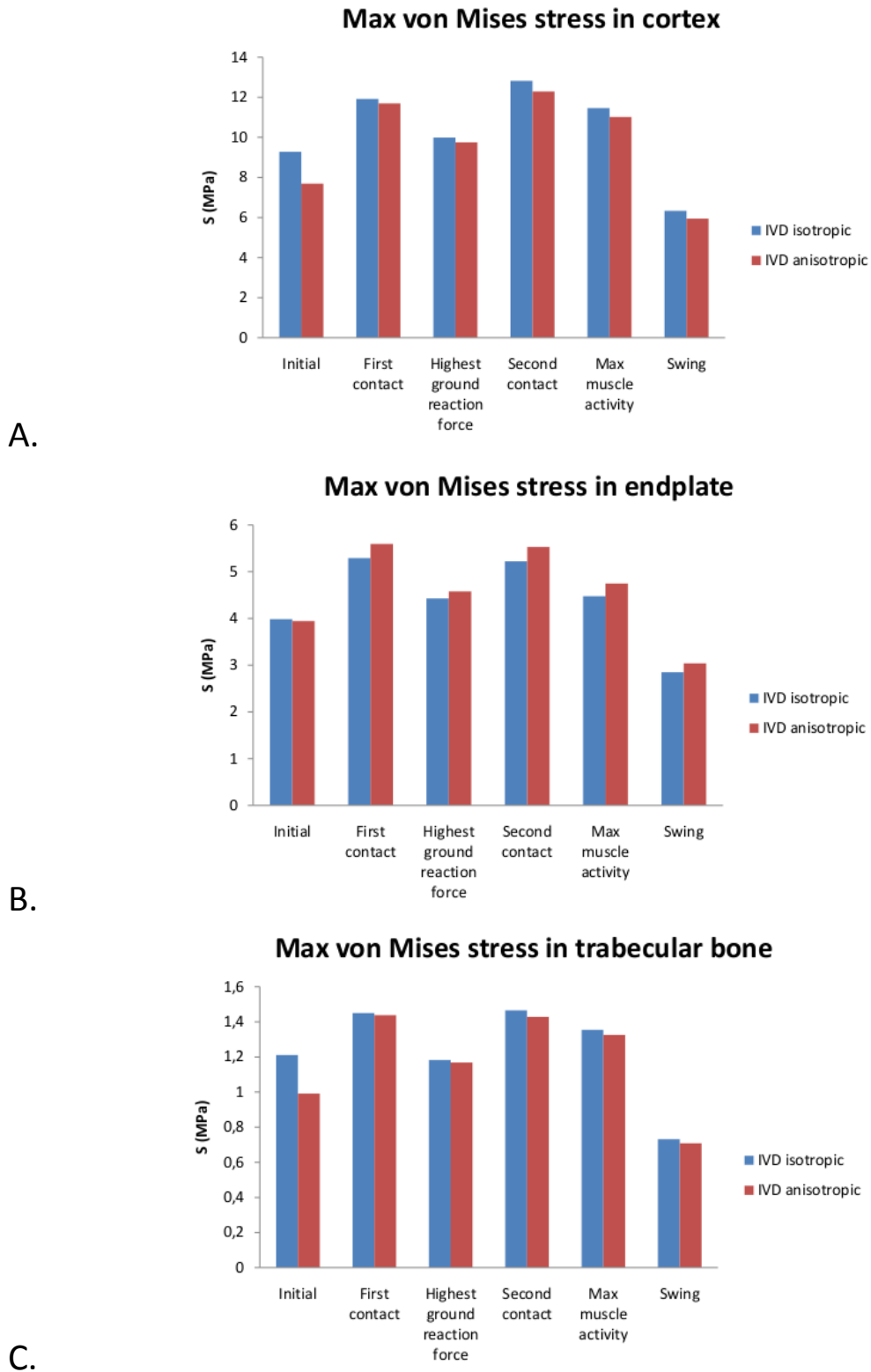


Fig. 6. Max von Mises stresses in each element set: a) endplate, b) cortex, and c) trabecular bone for the chosen positions. Results with isotropic and anisotropic IVD are plotted.

However, due to the scarce number of papers found on similar topic, it is hard to evaluate the validity of the results. In particular, the intervertebral disc model was idealized and was not validated in depth and the posterior elements of the vertebral body were missing. In spite of those limitations that are inherent to the FE model used, combining Anybody Modelling System and Abaqus can provide additional computational solutions to several medical issues such as implant loosening (Böhme et al. 2012).

Acknowledgments

The project was made possible through funding obtained from the European Community, Grant Agreement n° PITN-GA-2009-238690-SPINEFX.

References

- Böhme J., Shim V., Höch A., Mütze M., Müller C., Josten C. 2012. Clinical implementation of finite element models in pelvic ring surgery for prediction of implant behavior: A case report. *Clinical Biomechanics*. 27. 872–878
- Chevalier Y., Charlebois M., Pahr D., Varga P., Heini P., Schneider E., Zysset P.K. 2008. A patient-specific finite element methodology to predict damage accumulation in vertebral bodies under axial compression, sagittal flexion and combined loads. *Comput Meth Biomech Biomed Engin*. 11:477–487
- Crawford R.P., Cann C.E., Keaveny T.M. 2003. Finite element models predict in vitro vertebral body compressive strength better than quantitative computed tomography. *Bone*. 33(4):744–750
- Dall’Ara E., Schmidt R., Pahr D., Varga P., Chevalier Y., Patsch J., Kainberger F., Zysset P.K. 2010. A nonlinear finite element model validation study based on a novel experimental technique for inducing anterior wedge-shape fractures in human vertebral bodies in vitro. *J Biomech*. 43:2374–2380
- Dall’Ara E., Pahr D., Varga P., Kainberger F., Zysset P.K. 2011. QCT-based finite element models predict human vertebral strength in vitro significantly better than simulated DEXA. *Osteoporos Int*. DOI 10.1007/s00198-011-1568-3: Epub ahead of print
- Griffith J.F. and Genant H.K. 2008. Bone mass and architecture determination: state of the art. *Best Pract Res Clin Endocrinol Metab*. 22:737–764
- Grujicic M., Arakere G., Xie X., LaBerge M., Grujicic A., Wagner D., Vallejo A. 2010. Design-optimization and material selection for a femoral-fracture fixation-plate implant. *Materials and Design* 31: 3463–3473
- Homminga J., Weinans H., Gowin W., Felsenberg D. and Huiskes R. 2001. Osteoporosis changes the amount of vertebral trabecular bone at risk of fracture, but not the vertebral load distribution. *Spine* 26: 1555-1561
- Kanis JA et al. 2006. The use of multiple sites for the diagnosis of osteoporosis. *Osteoporos Int*. 17:527–534

- Maquer G., Schwiedrzik J.J. and Zysset P.K. 2012. Embedding of human vertebral bodies leads to higher ultimate load and altered damage localisation under axial compression. *Computer Methods in Biomechanics and Biomedical Engineering*. iFirst. 1-12
- Pahr D., Dall'ara E., Varga P., Zysset P.K. 2011. HR-pQCT based homogenized finite element models provide quantitative predictions of experimental vertebral body stiffness and strength with the same accuracy as μ FE models. *Comput Meth Biomech Biomed Engin.*iFirst article: 1–10
- Wagner D., Divringi K., Ozcan C., Grujicic M., Pandurangan B. and Grujicic A. 2010 Combined musculoskeletal dynamics/structural finite element analysis of femur physiological loads during walking. *Multidiscipline Modeling in Materials and Structures*. 6 (4): 417-437

Curriculum vitae

GHISLAIN MAQUER

Birth: 21st May, 1986 in Lens (FRANCE)

Nationality: French

Address: Mühledorfstrasse 28/127, 3018 Bern, SWITZERLAND

Personal Email address: ghislain.maquer@wanadoo.fr

Phone number: 0041 79 10 22 568

Languages: French, English (fluent), German (basics)

Education

2010-2013: Phd in Biomedical Engineering

Institute of Lightweight Design and Structural Biomechanics, TU Vienna, AUSTRIA

Institute for Surgical Technology and Biomechanics, University of Bern, SWITZERLAND

2006-2009 : Ecole nationale supérieure de physique de Strasbourg (Biomedical Engineering)

Strasbourg University, 67 Bas-Rhin, FRANCE

2007-2009: Master IRMC (Image processing, medical and surgical robotics)

Strasbourg University, 67 Bas-Rhin, FRANCE

2004-2006: Math sup / Math spé (Entrance exam preparation for engineering school)

Lycée Châtelet, Douai, FRANCE

2004: Baccalaureat scientifique (Scientific A-levels)

Lycée d'Artois, Noeux-les-Mines, France

Work experience

2010-2013: Research assistant

Institute of Lightweight Design and Structural Biomechanics, TU Vienna, AUSTRIA

Institute for Surgical Technology and Biomechanics, University of Bern, SWITZERLAND

2009-2009: Internship

Philips Consumer Lifestyle, Drachten, THE NETHERLANDS

2008-2008: Internship

Institute of Lightweight Design and Structural Biomechanics, TU Vienna, AUSTRIA

2007-2007: Internship

STA, Renault, Ruitz, FRANCE

Technical reports

Maquer G. 2012. "Meshing protocol: Meshing of intervertebral discs and cement in smooth models of vertebrae"

Maquer G. and Galibarov P. 2012. "Application of realistic boundary conditions computed from Invert dynamic analysis to a finite element model: stress distribution in a human lumbar vertebra during gait."

Publications in peer reviewed journals

Maquer G., Schwiedrzik J. and Zysset P.K. 2012. Embedding of human vertebral bodies leads to higher ultimate load and altered damage localisation under axial compression. *Comput Methods Biomech Biomed Eng.* iFirst article, 1–12

Maquer G., Dall'Ara E. and Zysset P.K. 2012. Removal of the cortical endplates has little effect on ultimate load and damage distribution in QCT-based voxel models of human lumbar vertebrae under axial compression. *J Biomech.* 45:1733–1738

Contributions to international conferences

Maquer G. and Zysset P.K. 2011. "Effect of boundary conditions on ultimate load and damage distribution in QCT-based voxel models of lumbar vertebrae under axial compression". Talk at Eurospine2011, Milan, Italy

Maquer G. and Zysset P.K. 2012. "Intervertebral disc degeneration influences ultimate load and damage distribution in human lumbar vertebral bodies under axial compression". Talk at Computer Methods in Biomechanics and Biomedical Engineering (CMBBE), Berlin, Germany

Declaration of originality

Declaration of Originality

Last name, first name: MAQUER Ghislain

Matriculation number: 11 - 133 - 014

I hereby declare that this thesis represents my original work and that I have used no other sources except as noted by citations.

All data, tables, figures and text citations which have been reproduced from any other source, including the internet, have been explicitly acknowledged as such.

I am aware that in case of non-compliance, the Senate is entitled to withdraw the doctorate degree awarded to me on the basis of the present thesis, in accordance with the "Statut der Universität Bern (Universitätsstatut; UniSt)", Art. 69, of 7 June 2011.

Place, date

Bern, 26/03/2013

Signature

